

POSSIBLE GRAVITATIONAL ANOMALIES IN QUANTUM MATERIALS

Phase I: Experiment Definition and Design

Award No. FA8655-03-1-3075

Date: 12. Feb. 2004

Prepared by: M. Tajmar and K. Hense, ARC Seibersdorf research

- be used for any purposes other than those for which it was supplied
- be copied or reproduced in whole or in detail without the prior written consent of ARCS
- be disclosed to any third party without the prior written consent of ARCS.

Report Documentation Page				Form Approved OMB No. 0704-0188	
Public reporting burden for the collection of information is estimated to average 1 hour per response, including the time for reviewing instructions, searching existing data sources, gathering and maintaining the data needed, and completing and reviewing the collection of information. Send comments regarding this burden estimate or any other aspect of this collection of information, including suggestions for reducing this burden, to Washington Headquarters Services, Directorate for Information Operations and Reports, 1215 Jefferson Davis Highway, Suite 1204, Arlington VA 22202-4302. Respondents should be aware that notwithstanding any other provision of law, no person shall be subject to a penalty for failing to comply with a collection of information if it does not display a currently valid OMB control number.					
1. REPORT DATE 15 SEP 2005		2. REPORT TYPE N/A		3. DATES COVERED -	
4. TITLE AND SUBTITLE Gravitational Anomalies in Quantum Materials				5a. CONTRACT NUMBER	
				5b. GRANT NUMBER	
				5c. PROGRAM ELEMENT NUMBER	
6. AUTHOR(S)				5d. PROJECT NUMBER	
				5e. TASK NUMBER	
				5f. WORK UNIT NUMBER	
7. PERFORMING ORGANIZATION NAME(S) AND ADDRESS(ES) Austrian Research Center - Seibersdorf Seibersdorf A-2444 Austria				8. PERFORMING ORGANIZATION REPORT NUMBER	
9. SPONSORING/MONITORING AGENCY NAME(S) AND ADDRESS(ES)				10. SPONSOR/MONITOR'S ACRONYM(S)	
				11. SPONSOR/MONITOR'S REPORT NUMBER(S)	
12. DISTRIBUTION/AVAILABILITY STATEMENT Approved for public release, distribution unlimited					
13. SUPPLEMENTARY NOTES The original document contains color images.					
14. ABSTRACT					
15. SUBJECT TERMS					
16. SECURITY CLASSIFICATION OF:			17. LIMITATION OF ABSTRACT UU	18. NUMBER OF PAGES 103	19a. NAME OF RESPONSIBLE PERSON
a. REPORT unclassified	b. ABSTRACT unclassified	c. THIS PAGE unclassified			

ABSTRACT

One of the authors (MT) recently published a paper, suggesting for the first time that a reported disagreement between experimental measurements and theoretical predictions for the magnetic field in rotating superconductors might arise from an anomalous high-order gravitomagnetic contribution (also known as frame dragging or Lense-Thirring effect). In normal matter, the ratio between electromagnetic and gravitational fields is given by the difference in the respective permeabilities. However, magnetic fields generated as a consequence of the quantization of the canonical momentum in a superconductor do not depend on the permeability. Hence, there is the possibility that the ratio between those two fields might be different in a quantum material.

This report summarizes the work carried out in Phase I – the experiment definition, detailed analysis and design. According to the performed analysis, the experimental apparatus described in this report is be able to resolve the gravitational anomaly having an ultimate resolution of $0.3 \mu\text{g}$ and exceeding the required rotational speeds and angular accelerations.

- be used for any purposes other than those for which it was supplied
- be copied or reproduced in whole or in detail without the prior written consent of ARCS
- be disclosed to any third party without the prior written consent of ARCS.

TABLE OF CONTENT

1	Introduction.....	4
2	Experiment Definition	5
2.1	Requirements for Experimental Assembly.....	5
2.2	Trade-Off Study for Major Components.....	9
2.2.1	Accelerometer and Electronics.....	9
2.2.2	Superconductor	15
2.2.3	Motor Assembly.....	18
3	Experiment Design	21
3.1	Overview of Complete Assembly	21
3.2	Mechanical Design	26
3.2.1	Rotational part	26
3.2.2	Vibrational Isolation of the Accelerometers	30
3.3	Thermal Design	42
3.4	Magnetic Fields	44
3.5	Electric connectors	47
3.6	Expected Performance in Laboratory Environment	48
4	Test Plans	49
4.1	Test Plan for Validation of Design.....	49
4.2	Test Plan for Experiment	50
5	References.....	51

1 INTRODUCTION

One of the authors (MT) recently published a paper [Tajmar et al. 2003], suggesting for the first time that a reported disagreement between experimental measurements and theoretical predictions for the magnetic field in rotating superconductors [Tate et al. 1989] might arise from an anomalous high-order gravitomagnetic contribution (also known as frame dragging or Lense-Thirring effect). In normal matter, the ratio between electromagnetic and gravitational fields is given by the difference in the respective permeabilities. However, magnetic fields generated as a consequence of the quantization of the canonical momentum in a superconductor do not depend on the permeability. Hence, there is the possibility that the ratio between those two fields might be different in a quantum material.

For Tate's experiment, a delta-gravitomagnetic field of at least $\Delta B_g = 1.62 \times 10^{-6} \text{ rad.s}^{-1}$ would be required to match the theoretical prediction of quantum and relativity theory. This is certainly above any classical coupling phenomena and will be investigated within this research program. Therefore, a facility is designed to rotate a high-temperature superconductive ring and measure, based on the Einstein-Maxwell equations of weak gravitational interactions [Tajmar et al. 2001], induced gravitoelectric fields using highly sensitive accelerometers by varying the speed of rotation. This report summarizes the design of the cryostat and the rotational superconductor assembly, as well as the selection of the major components and test plans to proceed with the actual measurement.

- be used for any purposes other than those for which it was supplied
- be copied or reproduced in whole or in detail without the prior written consent of ARCS
- be disclosed to any third party without the prior written consent of ARCS.

2 EXPERIMENT DEFINITION

2.1 Requirements for Experimental Assembly

Tate et al [Tate et al. 1990] followed Ginzburg-Landau theory, integrating the current density of Cooper pairs around a closed path including the effect of a rotating reference frame, but neglecting any gravitomagnetic fields:

$$\frac{m^*}{e^2 n_s} \oint_{\Gamma} \vec{j} \cdot d\vec{l} = \frac{nh}{2e} - \int_{S_{\Gamma}} \vec{B} \cdot d\vec{S} - \frac{2m^*}{e} \cdot \vec{\omega} \cdot \vec{S}_{\Gamma}, \quad (2.1)$$

where n_s is the Cooper-electron number density, S_{Γ} is the area bounded by Γ , ω the angular velocity, B the London moment and m^* the Cooper-pair mass measured by Tate. The argument put forward in [Tajmar et al. 2003] says that Tate's measured Cooper-pair mass m^* is different from the theoretically expected one m because Equ. (2.1) does not account for a possibly involved gravitomagnetic field B_g . The complete Ginzburg-Landau equation should read as

$$\frac{m}{e^2 n_s} \oint_{\Gamma} \vec{j} \cdot d\vec{l} = \frac{nh}{2e} - \int_{S_{\Gamma}} \vec{B} \cdot d\vec{S} - \frac{m}{e} \int_{S_{\Gamma}} \vec{B}_g \cdot d\vec{S} - \frac{2m}{e} \cdot \vec{\omega} \cdot \vec{S}_{\Gamma}. \quad (2.2)$$

Combining both equations we can express the gravitomagnetic field B_g as

$$\vec{B}_g = 2\vec{\omega} \cdot \left(\frac{m^* - m}{m} \right) + \left(\frac{m^* - m}{m} \right) \cdot \frac{1}{\vec{S} e n_s} \oint_{\Gamma} \vec{j} \cdot d\vec{l}. \quad (2.3)$$

In a superconductor that is thick compared to the London penetration depth, the current integral in the above equations can be set to zero as there is always a path inside the superconductor in which no current is flowing (outside the London penetration depth). The gravitomagnetic field is then just a function of the angular velocity and the mass difference of the Cooper-pairs

- be used for any purposes other than those for which it was supplied
- be copied or reproduced in whole or in detail without the prior written consent of ARCS
- be disclosed to any third party without the prior written consent of ARCS.

$$\vec{B}_g = 2\vec{\omega} \cdot \left(\frac{m^* - m}{m} \right). \quad (2.4)$$

For the case of Niobium, based on Tate's measurement, we can expect a gravitomagnetic field according to Figure 2.1-1.

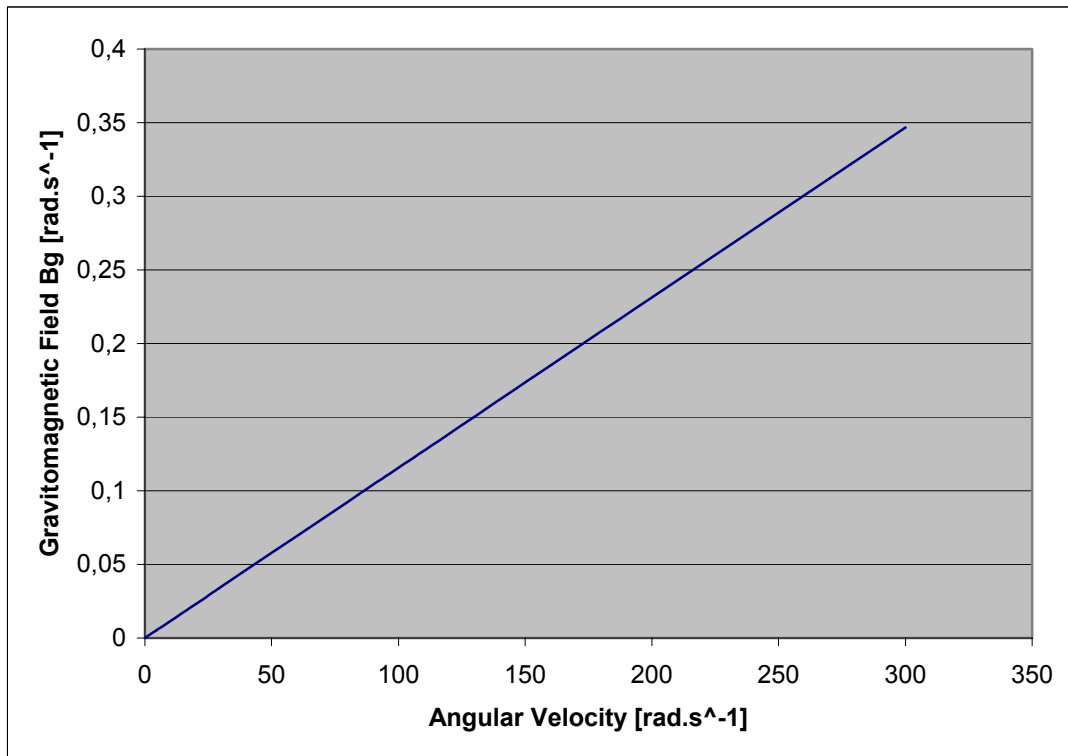


Figure 2.1-1 Expected gravitomagnetic field in thick Niobium superconductor as a function of angular velocity.

As the gravitomagnetic field is related to a gravitational field using the equations given by Tajmar and De Matos ([De Matos et al. 2001][Tajmar et al. 2001][Tajmar et al. 2003]).

- be used for any purposes other than those for which it was supplied
- be copied or reproduced in whole or in detail without the prior written consent of ARCS
- be disclosed to any third party without the prior written consent of ARCS.

$$\vec{\nabla} \times \vec{g} = -\frac{\partial B_g}{\partial t} \quad (2.5)$$

$$\oint \vec{\nabla} \times \vec{g} \, d\vec{A} = \oint \vec{g} \, d\vec{s} = \oint -\frac{\partial B_g}{\partial t} \, d\vec{A} \sim 2\pi r \vec{g}$$

an accelerated superconductor should show a change of the gravitational field. Combining Equ. (2.5) with (2.1), we can express the expected gravitational field at radial position r by

$$\vec{g} = -\dot{\vec{\omega}} \cdot \left(\frac{m^* - m}{m} \right) \cdot \frac{R^2}{r}. \quad (2.6)$$

where R is the outer radius of the superconducting ring. The result is shown in **Figure 2.1-2**.

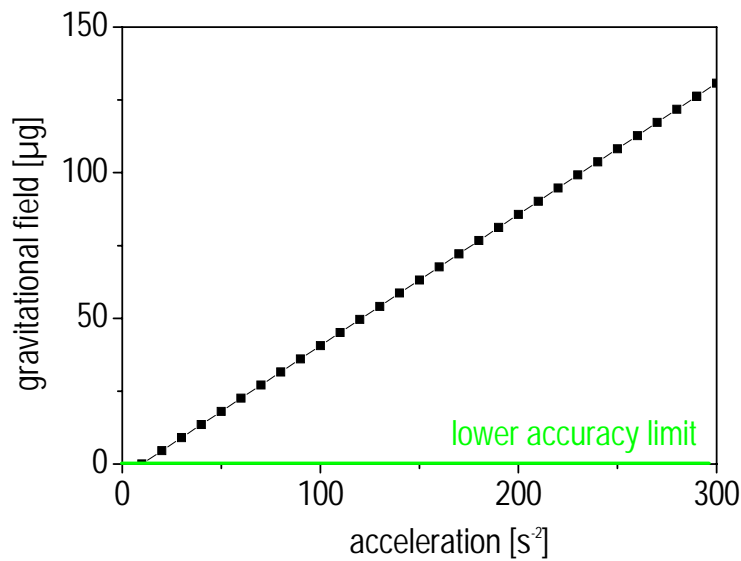


Figure 2.1-2 Expected gravitational field as a function of superconductor acceleration.

- be used for any purposes other than those for which it was supplied
- be copied or reproduced in whole or in detail without the prior written consent of ARCS
- be disclosed to any third party without the prior written consent of ARCS.

In order to get a measurable signal (assuming a resolution of $1\mu\text{g}$ of the acceleration sensor - see chapter 2.2.1), the necessary acceleration of the ring can be calculated to be higher than 200 s^{-2} . The distance between the acceleration sensor and the superconducting ring was chosen to be 30 mm in accordance with the design of the experiment. The area of the superconducting ring is $7 \times 15\text{ mm}^2$ as offered by Nexans superconductors (see chapter 2.2.2).

In order to get reasonable experimental results, the desired acceleration was taken to be 1.5 times the estimated acceleration (note, that one can expect a linear relation between the acceleration and the gravitational field). In order to allow filtering of the signal at the highest achievable acceleration of 300 s^{-2} , this acceleration has to be maintained for at least 1 second, resulting in a maximum rotational speed of 300 s^{-1} corresponding to approximately 3000 rpm.

In order to perform the experiment, the superconductor has to be cooled below its transition temperature. Therefore, a temperature limit of 77 K (LN_2) was chosen. However, due to the design of the experiment, an upgrade to 4.2 K (liquid He temperature) is possible without significant changes.

All requirements for the experimental facility are summarized in **Table 1**.

Resolution of Acceleration Sensor	$1\mu\text{g}$
Angular Acceleration of Superconductive Ring	$> 200\text{ s}^{-2}$
Minimum Measurement Time	1 s
Maximum Rotational Speed of Superconductive Ring	3000 rpm
Temperature of Superconductive Ring	77 K (LN_2)

Table 1 Summary of Requirements for Experimental Facility

- be used for any purposes other than those for which it was supplied
- be copied or reproduced in whole or in detail without the prior written consent of ARCS
- be disclosed to any third party without the prior written consent of ARCS.

2.2 Trade-Off Study for Major Components

2.2.1 Accelerometer and Electronics

There are several demands, which have to be reached by the accelerometer:

- 1) The accelerometer has to be small enough to fit into the superconducting ring. The measurement area has to be small compared to the inner diameter in order to measure the local acceleration instead of an average.
- 2) The signal has to be measured inert (without movement of the accelerometer) i.e. accelerometer has to show 1 g when being subjected to earth gravitational field.
- 3) The resolution of the accelerometer has to be high enough to reach at least 1 μg . For a lower resolution, the acceleration of the SCR has to be increased (see **Figure 2.1-2**), causing several design problems.
- 4) As there are nine accelerometers necessary (two positions near the surface, and one a referent position, each position consisting of three acceleration axes), also the price is an important factor.

After an extensive survey, four accelerometers have been investigated for their adaptability (all types are hermetically sealed and therefore compatible with vacuum operation) which are summarized in **Table 2** (Note: only the MWS sensor is a three-axis sensor, all other ones are single-axis sensors).

Manufacturer / Product	Resolution	Size	Price
Honeywell QA3000 Q-Flex [Honeywell]	50 $\text{ngHz}^{-0.5}$	25 x 25 x 25 mm	5500 \$/pc
Applied MEMS Si-Flex SF1500ULND [Applied Mems]	300 $\text{ngHz}^{-0.5}$ low frequency noise $\sim 3 \mu\text{gHz}^{-0.5}$	63 x 45 x 13 mm	600 \$/pc
Silicon designs 1221L-02 [Silicon Designs]	2 $\mu\text{gHz}^{-0.5}$ (down to 0,2 Hz)	8 x 8 x 3 mm (including electronics)	200 \$/pc
MWS Sensorik BS 5401 (3-axis) [MWS]	25 $\mu\text{gHz}^{-0.5}$	23 x 18 x 16 mm	2300 \$/pc

Table 2 Accelerometers Investigated for their Adaptability

As the resolution demand is 1 μg with a signal to noise ratio of at least 3 and a signal length of at least 1 s with at least 10 data points (= 10 Hz), the MWS sensor does not reach the demands of resolution. The best performing sensor is obviously the Honeywell Q-flex. But mostly due to its size and its high price, it has to be ruled out at the present stage.

The two remaining sensors (the Silicon Design and the applied MEMS accelerometers), are quite similar in price, however, the applied MEMS one is due to its large electronics (which has to be attached directly on the chip) too big for placing it inside the superconducting ring. Therefore, the Silicon Design 1221L-02 accelerometer (see **Figure 2.2-1**) was selected as the baseline, which has of course some shortcomings in resolution that can be balanced by proper measurement electronics.

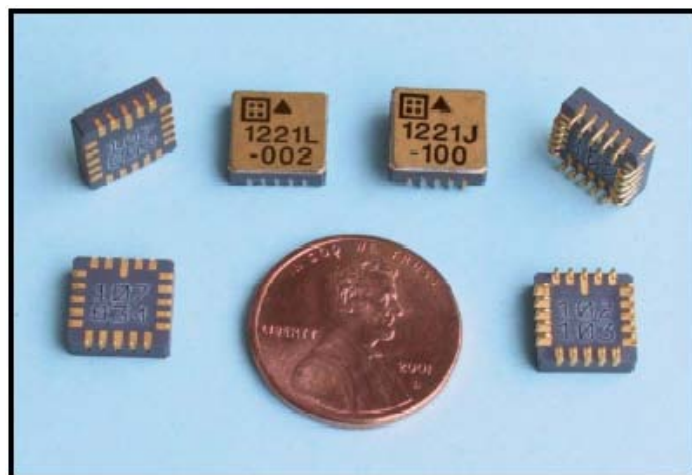


Figure 2.2-1 Photograph taken from the Silicon Designs 1221L-02 chip.

Silicon Design's accelerometers use capacitance change due to acceleration force as the sensed parameter. A capacitive approach allows several benefits when compared to the piezoresistive sensors used in many other accelerometers. In general, gaseous dielectric capacitors are relatively insensitive to temperature. Although spacings change with temperature due to thermal expansion, the low thermal coefficient of expansion of many materials can produce a thermal coefficient of capacitance about two orders of magnitude less than the thermal coefficient of resistivity of doped silicon. Therefore, the demands on the temperature regulation system can be kept minimal.

- be used for any purposes other than those for which it was supplied
- be copied or reproduced in whole or in detail without the prior written consent of ARCS
- be disclosed to any third party without the prior written consent of ARCS.

As compared with piezoelectric type accelerometers which require a dynamic input of some minimum frequency to generate a response, a capacitive sensing allows for response to DC accelerations guaranteeing a fully inert measurement.

Silicon Design's basic accelerometer unit is a 20 pin LCC package containing two parts: the Sense Element or sensor chip and the integrated electronics or ASIC chip **Figure 2.2-2**.

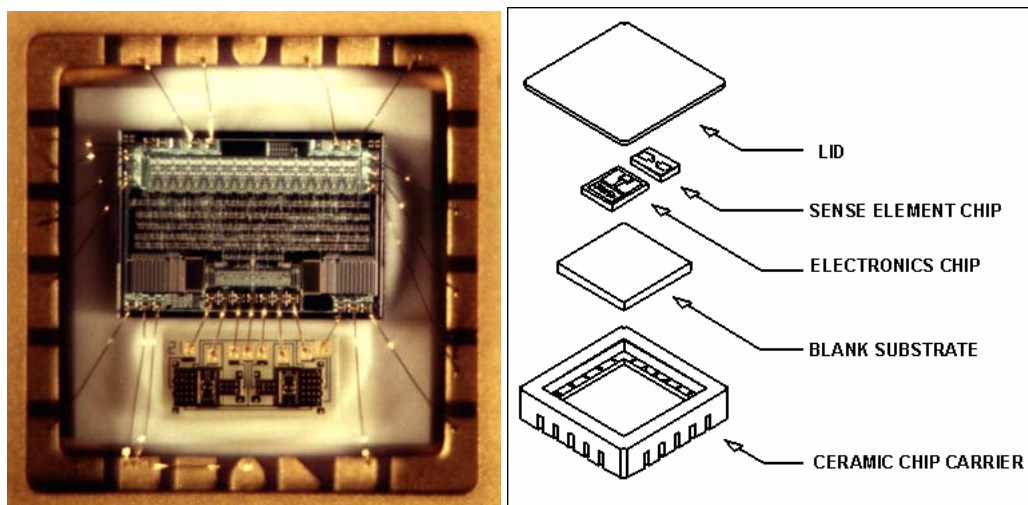


Figure 2.2-2 Photograph of the interior of the chip (left) and exploded schematic drawing (right).

The basic structure of the SDI sense element is shown below. The sense element wing is a flat plate of nickel supported above the substrate surface by two torsion bars attached to a central pedestal. The structure is asymmetrically shaped so that one side is heavier than the other, resulting in a center of mass that is offset from the axis of the torsion bars. When an acceleration force produces a moment around the torsion bar axis, the plate or wing is free to rotate, constrained only by the spring constant of the torsion bars.

On the substrate surface, beneath the sense element wing, two conductive capacitor plates are symmetrically located on each side of the torsion bar axis. The upper wing and the two lower capacitor plates on the substrate form two air-gap variable capacitors with a common connection. This creates a fully active capacitance bridge. When the wing rotates about the torsion bar axis, the average distance

- be used for any purposes other than those for which it was supplied
- be copied or reproduced in whole or in detail without the prior written consent of ARCS
- be disclosed to any third party without the prior written consent of ARCS.

between the wing and one surface plate decreases, increasing the capacitance for that plate, while the distance to the other plate increases, decreasing its capacitance (see Figure 2.2-3) .

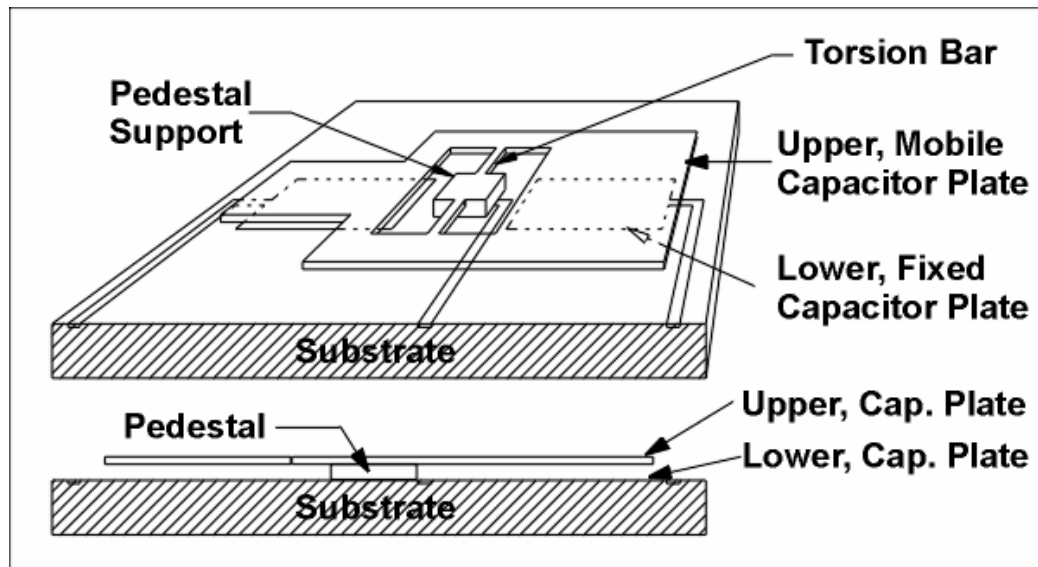


Figure 2.2-3 Operational principle of the accelerometer.

The sense element wings are approximately 1000 microns long by 600 microns wide and 5 to 10 microns thick. The wing to substrate spacing of about 5 microns results in a capacitance from the wing to each lower plate of about 0.15 pF. The sensitivity of the sense elements (the ratio of deflection to acceleration) is determined by the mass of the sense element, the distance from the center of mass to the torsion bar axis, and the torsion bar stiffness. Each complete sense element chip contains two wings for a total of four sensing capacitors.

The output of the Silicon Design's chip is a differential voltage of ± 2 V (at full scale of $\pm 2g$), making it necessary to measure voltages as low as $2 \mu\text{V}$ with a resolution of at least 100 nV. Therefore, a Keithley Nanovoltmeter 2182 (a two channel Voltmeter with a resolution of 10nV/100 nV for Channels one/two) has been chosen. The nanovoltmeter comes with an integrating A/D converter (the integration time can be adjusted in terms of 0.2 ms) and a digital moving filter (for the details of this filtering, we refer to the manual [Keithley]). The output can be read from an analog 0-10 V channel or directly using the GBIP interface. Full control of the nanovoltmeters can be taken from the computer using SCIP

- be used for any purposes other than those for which it was supplied
- be copied or reproduced in whole or in detail without the prior written consent of ARCS
- be disclosed to any third party without the prior written consent of ARCS.

protocol. Therefore, this part of the experiment can be remotely controlled avoiding human movements and subsequently vibrations in the vicinity of the experiment.

A simulated signal of 1 μg calculated for the Silicon designs 1221L-02 accelerometer attached to a 10 Hz lowpass filter and acquired by the Keithley 2182 nanovoltmeter with integration time of 20 ms (=1 Power-Load-Cycle PLC) and a digital moving filter of 10 is shown in the upper **Figure 2.2-4**. The Keithley settings are changed to 2 PLC and digital moving filter of 50 for the 0.3 μg signal shown in **Figure 2.2-4**.

- be used for any purposes other than those for which it was supplied
- be copied or reproduced in whole or in detail without the prior written consent of ARCS
- be disclosed to any third party without the prior written consent of ARCS.

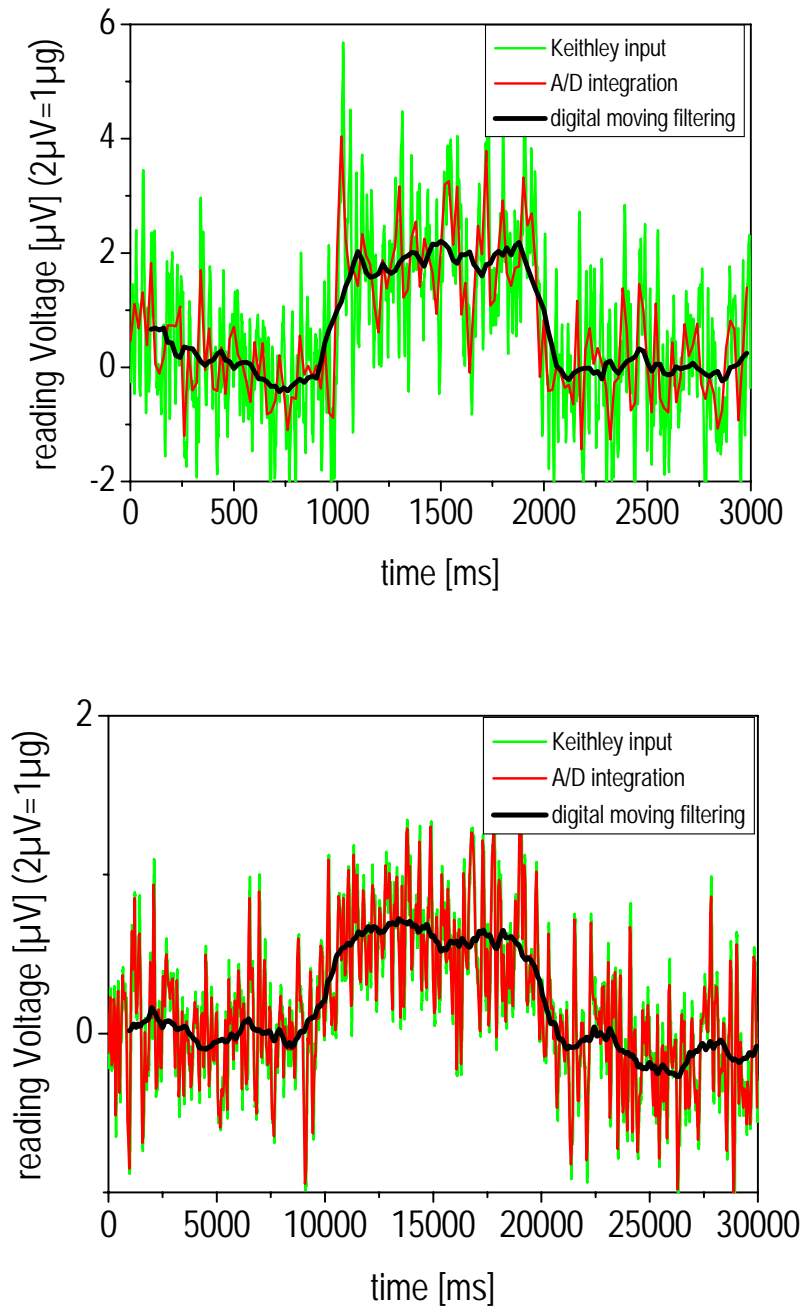


Figure 2.2-4 Simulated Signal of the Acceleration Sensor (upper: 1μg signal; lower: 0.3 μg signal). The green line gives the sensor output filtered using a 10 Hz low pass filter. The black line is the reading of the Keithley nanovoltmeter after integration time of 0.5 or 2 PLC (digital moving filter disabled). Enabling the digital moving filter with a filter count of 10 or 50, results in the red signals. The signal noise ratio is better than 3 for both signals.

2.2.2 Superconductor

Two types of high-temperature superconductors (HTC) are commercially available:

- 1) **YBCO**: The material is grown as multi domain structure. Three suppliers have been contacted:

Nexans superconductors: The production of the ring can be done either with glued segments or directly using a 12 domain ring (12 seeds crystals are necessary). The orientation of the grains will be axial. Therefore the superconducting plane will be the radial plane. However, the grain boundaries at the segment interfaces can serve as Josephson junctions. The success of producing such a ring can not be guaranteed. The price for a trial was quoted at 6730 €.

ISTEC: The International Superconductivity Technology Centre is world leader in producing large superconducting bulk-devices. A production of a single domain ring could be possible. However the properties will decay towards the edges of the disk. Therefore, a single domain ring with good properties can not be guaranteed. A price can not be quoted so far, but will be higher than the Nexans Superconductors product.

CAN Superconductors: The largest standard disk has a diameter of 50 mm (far from the experimental design). A try for a bigger multi seeded ring was roughly estimated to be in the order of 10 k€.

- 2) **BSCCO**: The Material can be produced as long conduit and will be aligned by melt-texturing. **Nexan superconductor** offered a standard BSCCO ring with an outer diameter of 150 mm and 6 mm wall thickness with a height of 15 mm for 1380 € (a higher ring is possible). For a ring with 15 mm wall thickness, the costs will be 3240 €, but the success can not be guaranteed due to the problems of the melt texturing process for such wall thicknesses.

American Superconductors, SCI Engineered Materials and the Slovakian Academy of Sciences (Group of P. Kovac and M. Polak) noted that they are only producing tape material, and are not producing bulk materials. The Austrian leader in superconductivity (Prof. Harald Weber from the Atomic Institute of the Vienna University of Technology) referred to contact ISTEC.

Therefore, the BSCCO ring offered by NEXANS superconductors was selected.

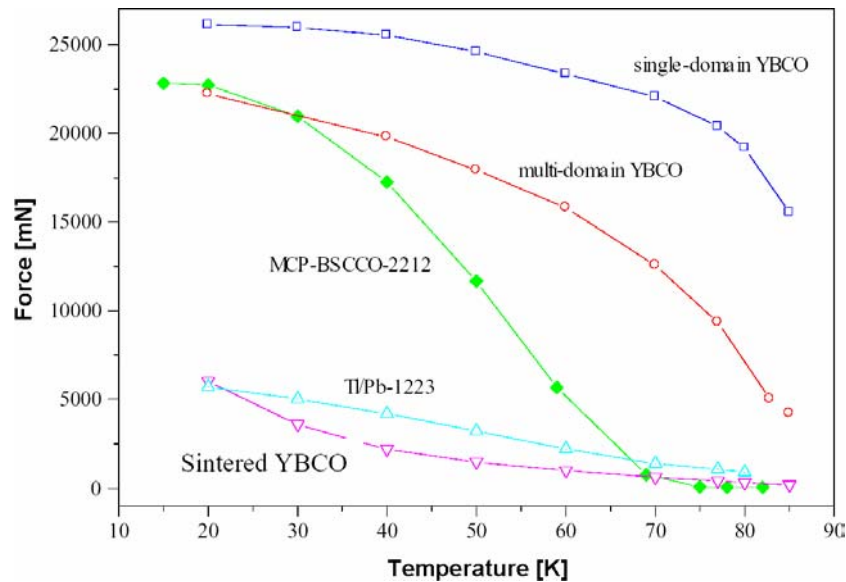
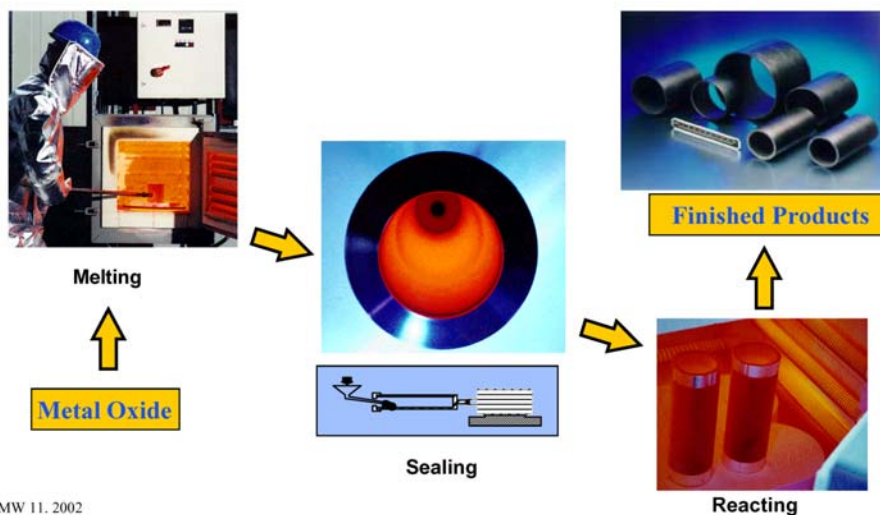


Figure 2.2-5 Levitation Force of Different Superconducting Materials as a Function of Temperature



Production of BSCCO-Tubes at NEXANS



BMW 11. 2002

Figure 2.2-6 Production Process of BSCCO Melt Textured Material

- be used for any purposes other than those for which it was supplied
- be copied or reproduced in whole or in detail without the prior written consent of ARCS
- be disclosed to any third party without the prior written consent of ARCS.



Production of Multi-Seeded YCBO Rings

Preparation Steps YBCO-Ring with 9 Domains $d_a = 100$ mm



BMW 11, 2002

Figure 2.2-7 Production Process of YBCO Multi Seeded Ring

- be used for any purposes other than those for which it was supplied
- be copied or reproduced in whole or in detail without the prior written consent of ARCS
- be disclosed to any third party without the prior written consent of ARCS.

2.2.3 Motor Assembly

As motor, a brushless servo motor with computer controllable amplifier (ability of remote control of the experiment) was chosen. The rotational speed, as well as the acceleration given in **Table 1** has to be reached by the motor. Obviously, there are several motors reaching the demands. As all motors are similar in performance and price, it was decided to take the motor from Torque Systems (an American supplier) [**Torquesystems**]. For the amplifier, the PWM Brushless Sinusoidal Servo amplifier was chosen. The amplifier allows for full control of the rotational speed or the applied torque and allows running step less profiles.

As the moment of inertia of the rotating part in the experiment (superconductor including the support structure) has a designed value of 0.010 kgm^2 , the torque necessary to reach 300 s^{-2} is 3 Nm . Therefore, the BNR3034 brushless servo motor was chosen. This motor is fully compatible with the servo amplifier, and allows for a maximum stall torque of 3.8 Nm (a peak torque of 16.95 Nm), as well as a maximum operation speed of 5800 rpm . Therefore, the design goals are completely reached, and can even be extended without changing the motor setup (the mechanical stability to do so have to be checked during the evaluation phase). The weight of 4.3 Kg has to be carried by the structure. The moment of inertia of the rotor is about 10% of the moment of inertia of the experimental structure, and does therefore not significant effect the performance of the motor.



Figure 2.2-8 Motor and Servo Amplifier Proposed to be Used in the Experiment

- be used for any purposes other than those for which it was supplied
- be copied or reproduced in whole or in detail without the prior written consent of ARCS
- be disclosed to any third party without the prior written consent of ARCS.

In order to estimate the influence of the magnetic field acting on the superconductor due to the motor at maximum acceleration, the motor windings can be approximated as a simple coil pointing toward the superconductor. No shielding of the magnetic field due to the cryostat structure etc. is assumed. It has to be emphasized, that this situation shown in **Figure 2.2-9** is a clear overestimation of the actual situation.

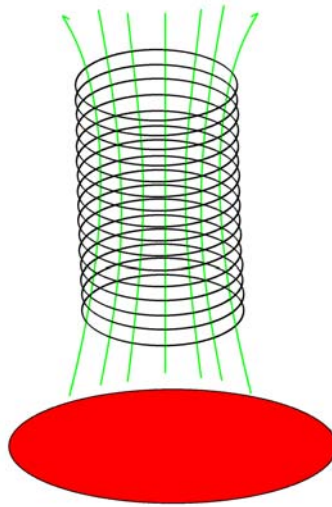


Figure 2.2-9 Schematic sketch describing the magnetic field due to the motor acting on the superconductor.

By using

$$L = \frac{N^2 \mu_0 A}{l} \quad (2.2)$$

$$B = \mu_0 I \frac{N}{l} \frac{A}{4\pi} \left(\frac{1}{\left(d - l/2\right)^2} - \frac{1}{\left(d + l/2\right)^2} \right)$$

one can calculate the magnetic field to be

$$B = I \sqrt{\frac{L A \mu_0}{l}} \frac{1}{4\pi} \left(\frac{1}{\left(d - l/2\right)^2} - \frac{1}{\left(d + l/2\right)^2} \right) \quad (2.3)$$

- be used for any purposes other than those for which it was supplied
- be copied or reproduced in whole or in detail without the prior written consent of ARCS
- be disclosed to any third party without the prior written consent of ARCS.

The current $I=6.6$ A (for a torque of 3.8 Nm at a rate of 0,57Nm/A). The inductance $L=4.9$ mH. The dimensions of the motor (area A and length l) have been estimated to be about 60 % of the outer dimensions of the motor. The distance z from the motor to the superconductor has been estimated from the design drawings to be 400 mm. Taking all this data as an input to equation (2.3), the magnetic field coming from the motor is about 30 μ T, and is therefore in the same order of magnitude as the earth magnetic field (30-60 μ T). As the described situation is definitely an overestimation of the actual situation, the magnetic influence of the motor can be neglected.

Air motors (having no magnetic moment acting on the superconductor) are ruled out, as their control is much more complicated compared to standard servo motors, and high torques and high rotational speed are not easily achievable. Products supplied from Duesterloh, Dynatork, Kinequip and PSIautomation have been investigated [**Airmotors**].

- be used for any purposes other than those for which it was supplied
- be copied or reproduced in whole or in detail without the prior written consent of ARCS
- be disclosed to any third party without the prior written consent of ARCS.

3 EXPERIMENT DESIGN

3.1 Overview of Complete Assembly

The interplay and principal assembly of the key-components described above is shown in the block diagram in Figure 3.1-1. In addition to the key components, a temperature regulation for some parts is necessary to maintain the operational condition of these components.

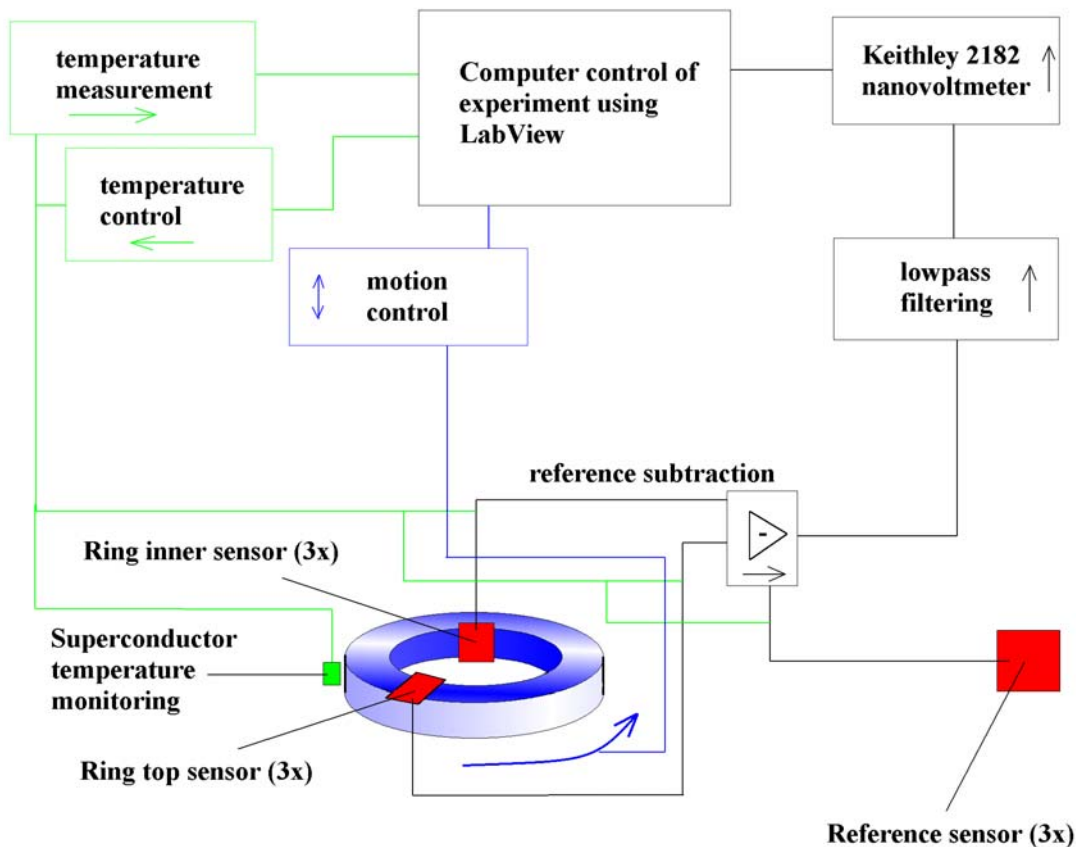


Figure 3.1-1 Block Diagram of the Experimental Setup

The design of the experiment identifying the key components and the information flow path shown in Figure 3.1-1 is given in Figure 3.1-2.

- be used for any purposes other than those for which it was supplied
- be copied or reproduced in whole or in detail without the prior written consent of ARCS
- be disclosed to any third party without the prior written consent of ARCS.

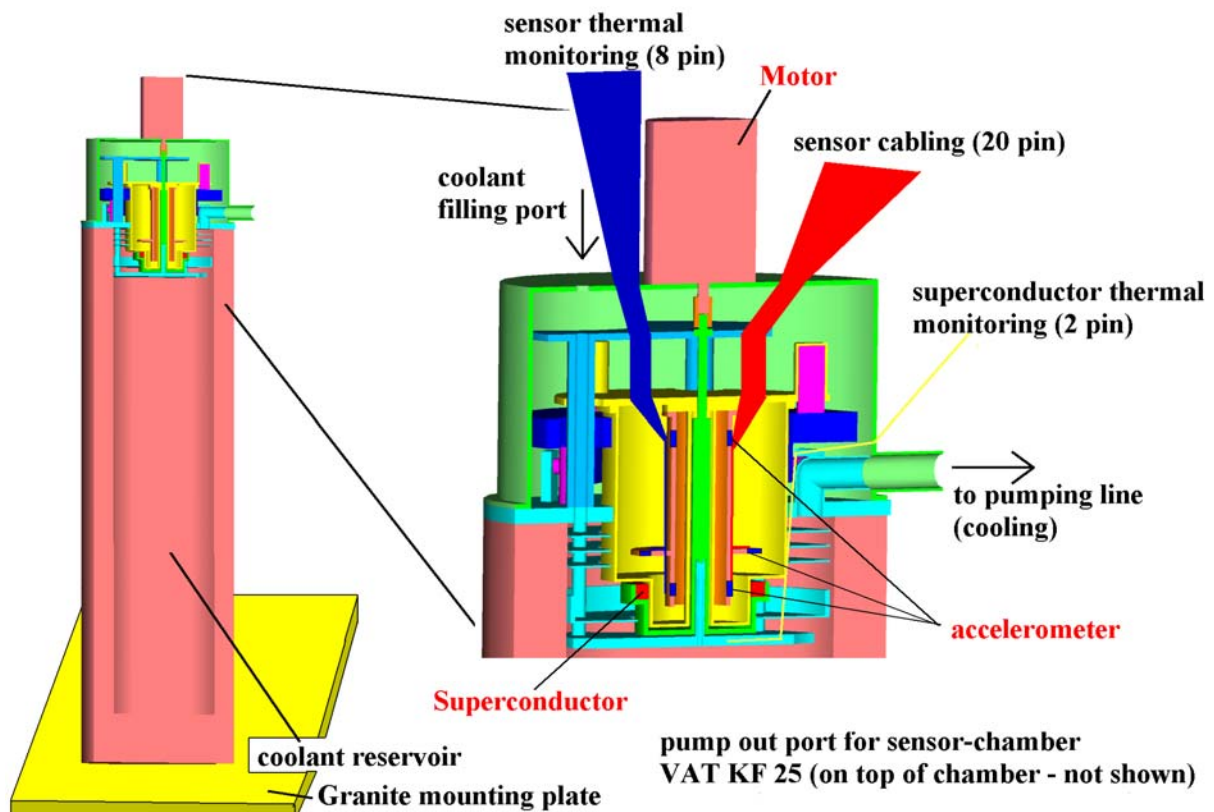


Figure 3.1-2 Design of the Experiment identifying the Key Components and the Information Flow Path

The detailed design identifying the structural elements of the experiment is shown in **Figure 3.1-3**. The cryogenic system is omitted in this figure.

- be used for any purposes other than those for which it was supplied
- be copied or reproduced in whole or in detail without the prior written consent of ARCS
- be disclosed to any third party without the prior written consent of ARCS.

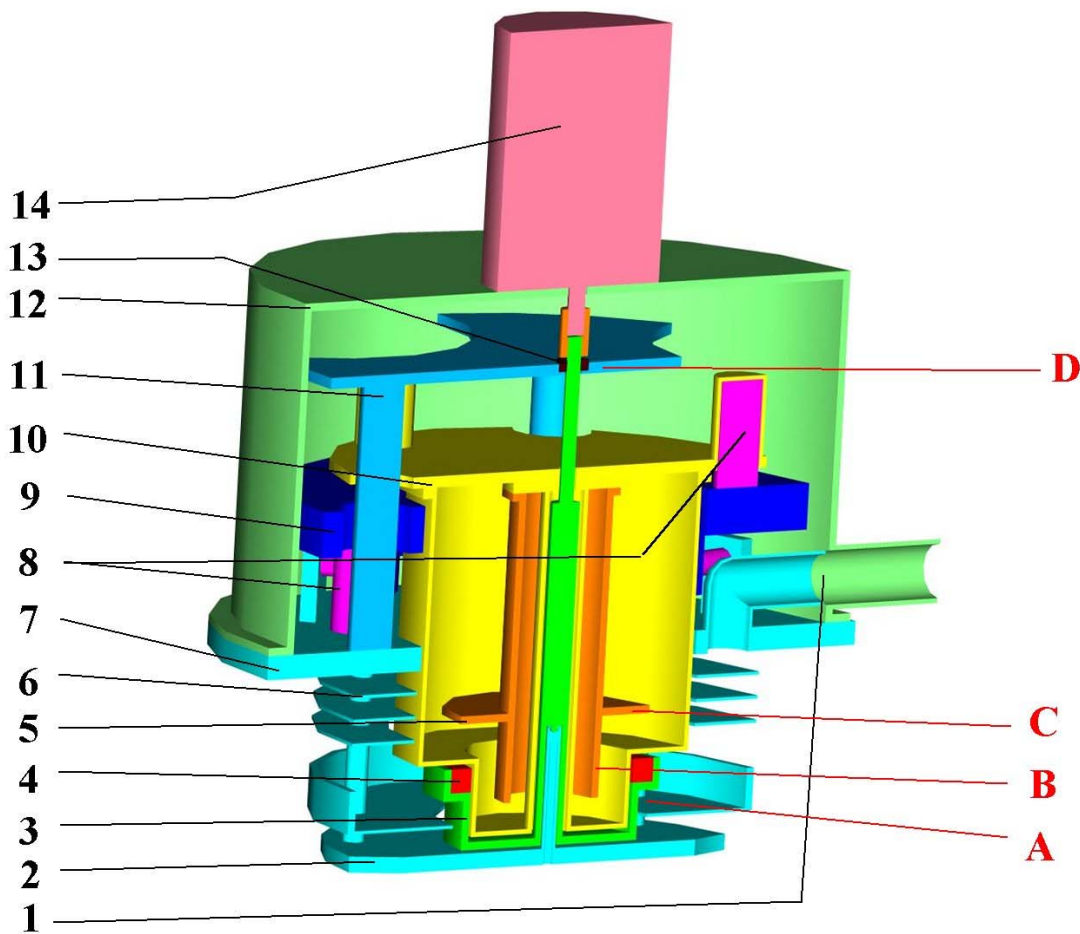


Figure 3.1-3 Complete Design of the Experiment. The black numbers mark structural design parts. The red letters state temperature measurement and –regulation points. As this is only the design, for the detailed solutions (including cryostat, cabling and valves) see later.

- 1) Coolant exhaust port. The conduit coming out of part 7 is used to prevent the upper parts from being extensively cooled by cryogenic gas.
- 2) Lower support structure for the rotating part. The cold bearing is designed to be radial ball bearing with solid lubricant.
- 3) Support structure for the superconducting ring. The support structure carries the SCR, and is attached directly to the Motor (Part 14)
- 4) Superconducting ring
- 5) Mounting structure for the accelerometers and Gauss-meter

- 6) Radiation shields (thermal design). The radiation shield at the height of the SCR acts as structural support for the magnetic field coil #5, as well as as coolant guide force the gas flow toward the SCR support structure.
 - 7) Mounting flange. The whole structure is connected via the mounting flange to the cryostat (the cryostat is not shown in the design).
 - 8) Vibrational damping springs. The operation will be explained in much detail in the following sections.
 - 9) First stage ring of the vibrational damping system.
 - 10) Vacuum container carrying the thermal as well as the structural support to allow the operation of the sensors.
 - 11) Upper support structure of the rotating parts. The liquid gas will be supplied through the stilts. This should again prevent extensive cooling of the upper parts especially shortly after the cooling down phases.
 - 12) Experiment closure. In order to prevent cryo pumping of air and humidity to the experimental structure causing the risk of freezing the bearings.
 - 13) Upper bearing (ball bearing)
 - 14) Motor
-
- A) Measurement of the SC temperature. The temperature will be measured about one mm below the lower support structure. Due to the experience given in [Hense 2002]; [Hense 2004], the temperature accuracy necessary to control the SCR temperature can be achieved in gas flow regime even when not attaching the thermometer directly to the structure of which the temperature is of interest. In addition, the temperature should have only a minor influence on the effect (even if the temperature is wrong by some tenth of a Kelvin, the influence can be neglected), as long as the superconductor is cooled below its transition temperature.
 - B) Measurement and Control of the accelerometer temperature in order to achieve the specified temperature range of the SD1221L-02.
 - C) Measurement and Control of the accelerometer temperature in order to achieve the specified temperature range of the SD1221L-02.
 - D) Measurement and control of the temperature of the upper bearing in order to prevent freezing of the bearing due to thermal conductivity of the rotating support structure.

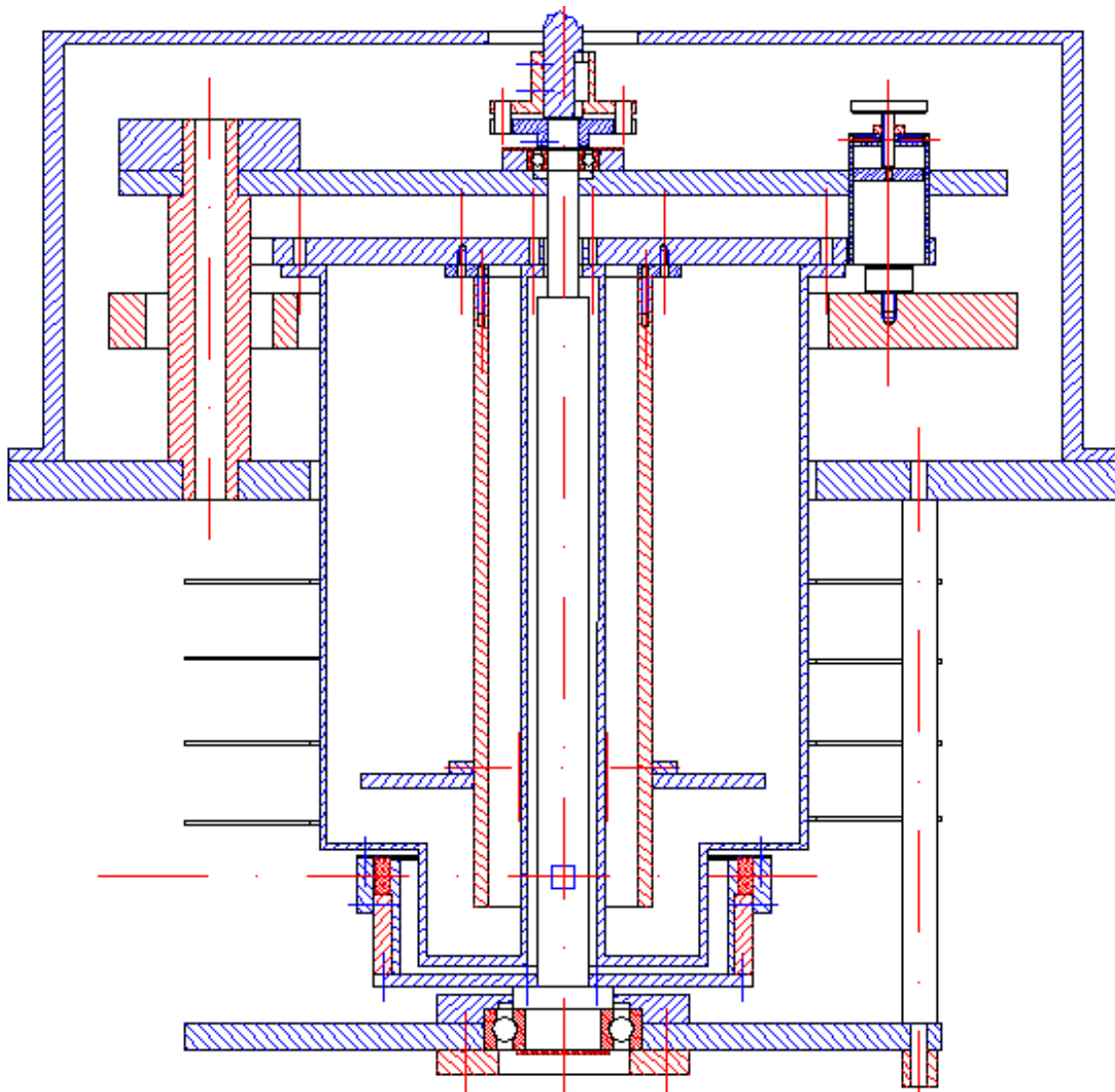


Figure 3.1-4 Mechanical drawing (The drawing is simplified in order to avoid confusions).

- be used for any purposes other than those for which it was supplied
- be copied or reproduced in whole or in detail without the prior written consent of ARCS
- be disclosed to any third party without the prior written consent of ARCS.

3.2 Mechanical Design

3.2.1 Rotational part

The design of the rotating parts (3 and 4 in **Figure 3.1-3**) is shown in **Figure 3.2-1**. The final weight of the rotor is 4 kg, and its moment of inertia is 0.01 kgm².

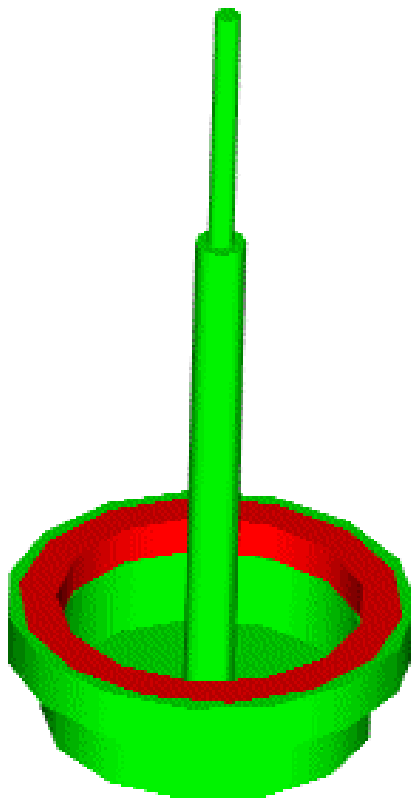


Figure 3.2-1 Design of the Rotational Part of the Experiment (Including the Superconducting Ring – Red Color)

In the final construction, the part has to be separated in two functional groups:

1) The lower part of the support structure (which is well separated from the SCR) and the axis going to the motor. This part has to have high mechanical strength (the whole torque will be conducted through this axis), as well as low thermal conductivity in order to prevent heating of the superconductor via the

- be used for any purposes other than those for which it was supplied
- be copied or reproduced in whole or in detail without the prior written consent of ARCS
- be disclosed to any third party without the prior written consent of ARCS.

structure and cooling of the ball bearing at the upper side. The acceleration of the SCR causes a shear stress of about 30 N/mm² (well below the usual upper limit for the torque of 80 N/mm²) in the axes, as well as a torque of 0.5° [Böge 1989].

The upper bearing is a radial roller bearing of type 6001 (axis diameter 12 mm), the inner ring is allowed to move along the axis. The outer ring is fixed in the mounting structure. The connection to the motor is done using a positive fit clutch (see **Figure 3.2-2**).

The lower bearing is a KOYO radial ball bearing, compatible with cryogenic temperatures, with solid lubricant (silver), of 6206 type. The maximal allowed rotational speed of the bearing is specified to be ~3000 rpm. The dynamic load rating of this type of bearing is 1.5 kN (and 75 0N static). The maximal axial force is about 50 N (the weight of the rotor), and the radial force is about 170 N (from the asymmetric rotating superconductor due to imperfect centering caused by thermal expansion). This results in an dynamic equivalent bearing load of 170 N. Using this as an input, the bearing lifetime (assuming the bearing to be operated at 3000 rpm for the whole lifetime) can be estimated to be higher than 4000 h. Therefore, the allowed parameters of the bearing are well within the expected forces acting on it. It has to be emphasized, that this calculation is only necessary for the cold bearing, as the mechanical strength of the standard bearing used on the warm side is 13 times higher than for the same EXCEF bearing (see **Figure 3.2-3**).

For both, the warm and the cold bearing an emergency friction type bearing with a thickness of ~5 mm steel is included, in order to reduce the risk of damaging the experiment in the case of a failure of the roller bearings.

- be used for any purposes other than those for which it was supplied
- be copied or reproduced in whole or in detail without the prior written consent of ARCS
- be disclosed to any third party without the prior written consent of ARCS.

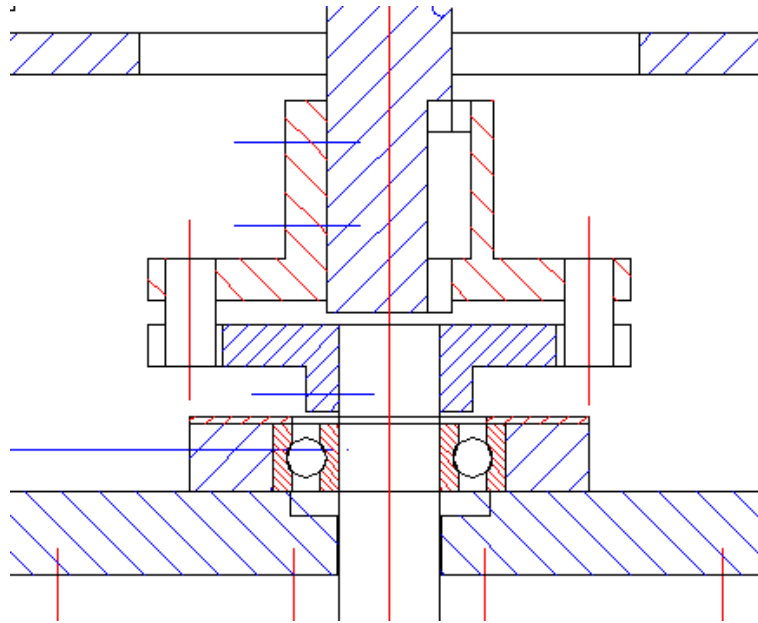


Figure 3.2-2 Clutch between the rotor and the motor. The radial roller bearing is of 6001 type.

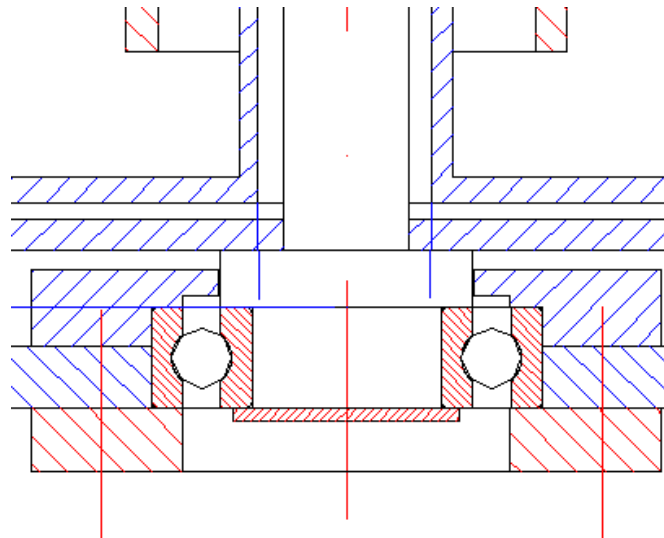


Figure 3.2-3 Design of the cold bearing. The torque is supplied to the support structure using three 3mm bolts separated by 120° from each other).

2) The part supporting the superconducting ring directly. This part should have good thermal conductivity in order to allow a good cooling from the gas flow which passes below the support structure. In order to reduce the moment of inertia due to heavy weight at high radii, this support material has to be pure aluminum. The thermal conductivity of aluminum is 229 W/m K. In comparison,

the thermal conductivity of copper is 372 W/m K, however, the density is 8960 kg/m³ (compared to 2700 kg/m³ for aluminum). The thermal conductivity of steel is typically 16.3 W/m K with an typical density (Steel 1.4301) of 7900 kg/m³ [VDI1997].

The centering of the BSCCO superconductor is done from the inner side (at room temperature), and at cryogenic temperature, the ring is kept in position from the outer side by an aluminum cage, which has three small contacts to the superconductor. This is necessary, as the linear thermal expansion coefficient of BSCCO is about $5.9 \times 10^{-6} \text{ K}^{-1}$ in the range down to 10 K [Escher et al. 1996].

The thermal expansion of aluminum in the same range is about $20 \times 10^{-6} \text{ K}^{-1}$ [VDI1997]. Therefore, the excess contraction of the support structure is about 0.6 mm with respect to the (brittle) HTC superconducting ring. The support structure is designed to center the ring properly at cryogenic temperatures.

In order to prevent the ring from slipping with respect to the support structure, a axial force is applied, to produce frictional connection of the ring to the support structure (see Figure 3.2-4).

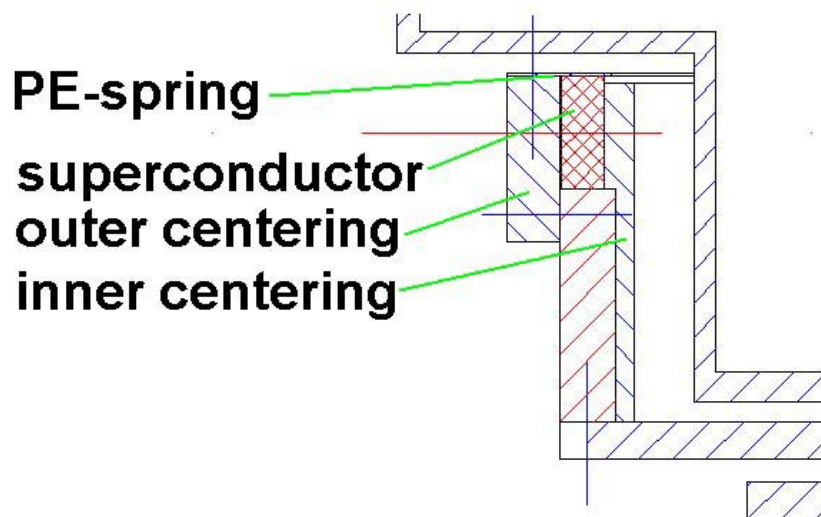


Figure 3.2-4 Centering and frictional connection of the ring to the support structure.

- be used for any purposes other than those for which it was supplied
- be copied or reproduced in whole or in detail without the prior written consent of ARCS
- be disclosed to any third party without the prior written consent of ARCS.

3.2.2 Vibrational Isolation of the Accelerometers

The sensors will be put in a separate vacuum chamber, and are packed by a multilayer insulation to maintain the permitted operational temperature of the sensors. This chamber is mounted on a two step vibration isolation system consisting of commercial springs, as well as a copper ring and the vacuum chamber itself as oscillator masses. The setup is shown in **Figure 3.2-5**.

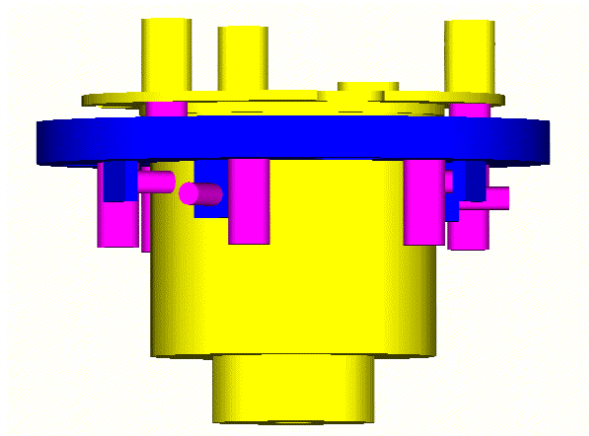


Figure 3.2-5 Sketch of the Vibration Isolation. The springs are plotted violet, mass 1 is given by the blue ring, the yellow ring contains the vacuum chamber with the accelerometers, and serves as second mass. The support structure is not shown in this figure.

The isolation system can be interpreted as a double pendulum as shown in **Figure 3.2-6**. For an elaborated discussion in the analysis of vibrational spectra we referee to the literature [Hense 1999/2002].

Mass M_0 is driven to oscillate by an external force F_0 . This force comes from the eccentricity of the rotated superconductor, which is transmitted to the housing (M_0), and from oscillations of the whole system due vibrations of the surroundings (moving persons, traffic, ...). The oscillations are transported to mass M_1 (#10) via spring c_1 (#9) and from there to the sensor housing (#11) via spring c_2 (#9). Spring c_0 gives the mounting of the whole structure to the laboratory floor, and is used to isolate vibrations from the surrounding.

- be used for any purposes other than those for which it was supplied
- be copied or reproduced in whole or in detail without the prior written consent of ARCS
- be disclosed to any third party without the prior written consent of ARCS.

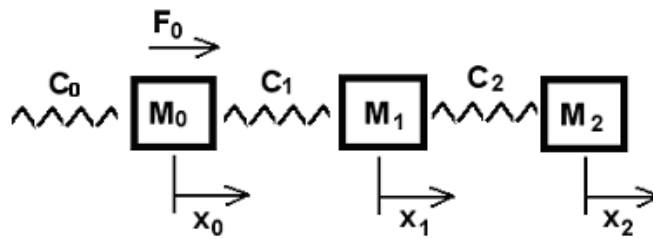


Figure 3.2-6 Schematic Interpretation of the Vibration Isolation System.

Therefore, the equation of motion for this system reads as:

$$\begin{aligned} M_0 x_0'' &= F_0 + c_1(x_1 - x_0) \\ M_1 x_1'' &= c_1(x_0 - x_1) + c_2(x_2 - x_1) \\ M_2 x_2'' &= c_2(x_1 - x_2) \end{aligned} \quad (3.2)$$

or alternatively

$$\bar{X}'' = \tilde{C}\bar{X} + \frac{1}{M_1}\vec{F}_0 \quad (3.3)$$

with the abbreviations

- be used for any purposes other than those for which it was supplied
- be copied or reproduced in whole or in detail without the prior written consent of ARCS
- be disclosed to any third party without the prior written consent of ARCS.

$$M_i x_i = X_i$$

$$\vec{C} = \begin{pmatrix} -\frac{c_1 + c_0}{M_0} & \frac{c_1}{M_0} & 0 \\ \frac{c_1}{M_1} & -\frac{(c_1 + c_2)}{M_1} & \frac{c_2}{M_1} \\ 0 & \frac{c_2}{M_2} & -\frac{c_2}{M_2} \end{pmatrix}$$

$$\vec{F}_0 = F_0 \begin{pmatrix} 1 \\ 0 \\ 0 \end{pmatrix} = f_0 \exp(i\omega t) \begin{pmatrix} 1 \\ 0 \\ 0 \end{pmatrix}$$

Assuming harmonic excitations, the oscillations X_i have to be of harmonic type, therefore, the three dimensional linear differential equation can be transformed to a linear equation:

$$\begin{aligned} X_i &= \Psi_i \exp[i(\omega t + \varphi)] = \Psi_i \exp[i\omega t] \exp(i\varphi) = \Theta_i \exp[i\omega t] \\ X_i'' &= -\Psi_i \omega^2 \exp[i(\omega t + \varphi)] = -\Theta_i \omega^2 \exp[i\omega t] \end{aligned} \quad (3.4)$$

Note, that the quantity Θ_i is now complex defined. Therefore, a homogenous solution of the problem is defined to be:

$$-\omega^2 \Theta_i = C_{ij} \Theta_j \quad (3.5)$$

Obviously, the above equation has three independent eigenvectors, and three orthonormal eigenvectors. Therefore, the matrix C_{ij} can be transformed to diagonal form using

$$(\vec{\Theta}^T)_{im} C_{ml} \vec{\Theta}_{lj} = \omega_i^2 \delta_{ij} \quad (3.6)$$

- be used for any purposes other than those for which it was supplied
- be copied or reproduced in whole or in detail without the prior written consent of ARCS
- be disclosed to any third party without the prior written consent of ARCS.

Note, that on the right hand side of above equation, the Einstein convention must not be applied. The notation simply represents a diagonal matrix, where the diagonal elements are the eigenfrequencies ω_i . Applying above transformation to the inhomogeneous equation, one ends up with

$$\Phi_i'' = \left(\tilde{\Theta}^T \tilde{C} \tilde{\Theta} \right)_{ij} \Phi_j + \left(\tilde{\Theta}^T \right)_{ij} (F_0)_j = \omega_i^2 \delta_{ij} \Phi_j + \gamma_i \quad (3.7)$$

where the Φ_i 's are the normal modes of the system. As the matrix $\left(\tilde{\Theta}^T \tilde{C} \tilde{\Theta} \right)$ is now diagonal, the three equations are decoupled, and therefore, the system can be treated as three (independent) driven oscillators, with the well known solutions

$$\Phi_i = \frac{\gamma_i}{M_0} \frac{1}{\omega_i^2 - \omega^2} \quad (3.8)$$

which can be transformed back to the coordinates X_i using the matrix $\tilde{\Theta}$. Therefore, one ends up with (including a damping δ)

$$X_i = \Theta_{ij} \frac{\gamma_j}{M_0} \frac{1}{\sqrt{(\omega_j^2 - \omega^2)^2 + 4\delta^2 \omega^2}} \exp(i\omega_j t) \quad (3.9)$$

In the present case, not the amplitude of the oscillations transferred through the isolation system are of interest, but only the accelerations acting on the accelerometers, which are the second derivative of X_3 . Assuming the driving force to come from the rotating superconductor, the driving force can be assumed to be:

$$F_0 = m r_{ex} \omega^2 \quad (3.10)$$

where m is the mass that is rotational asymmetric, and r_{ex} is the radius of this asymmetry (the displacement of the centre of gravity from the ideal axis).

For the further analysis, it is obvious that the eigenfrequencies of the system have to be as low as possible. Therefore, the dependence of the eigenfrequency as a function of the input parameter was done putting above equations to Mathematica by Wolfram research. The results are shown in **Figure 3.2-7** and **Figure 3.2-8**.

- be used for any purposes other than those for which it was supplied
- be copied or reproduced in whole or in detail without the prior written consent of ARCS
- be disclosed to any third party without the prior written consent of ARCS.

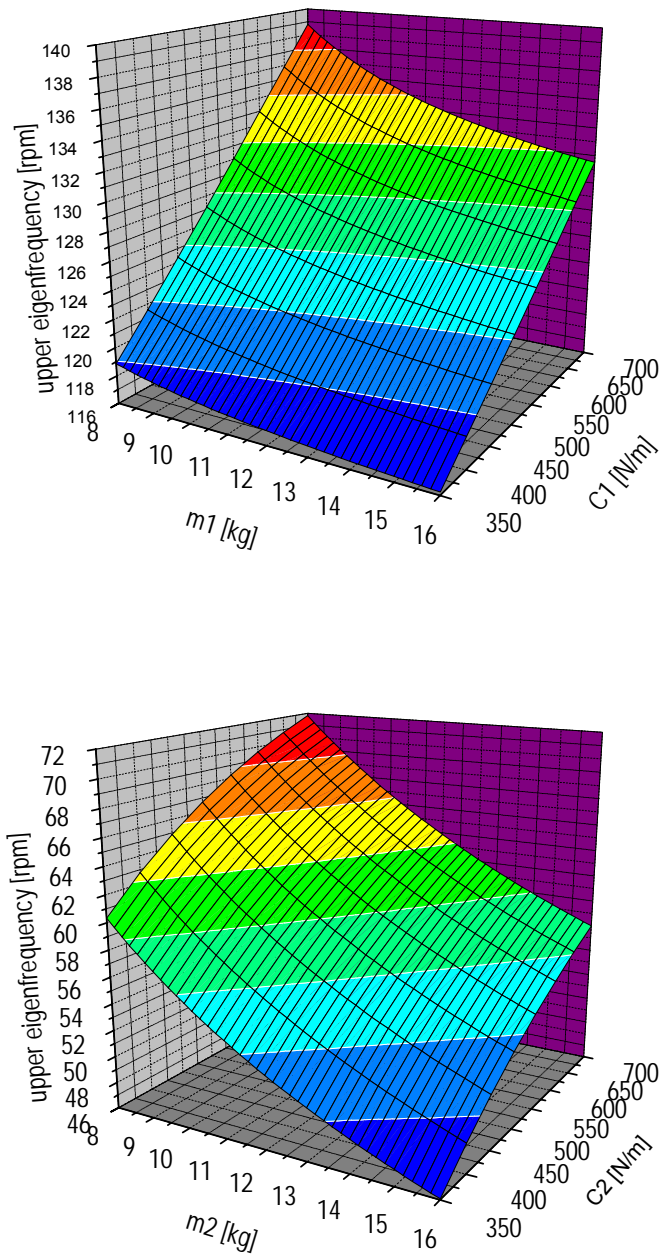


Figure 3.2-7 Influence of the Masses M_1 and M_2 as well as of the Spring Constants c_1 and c_2 on Eigenfrequency ω_1

- be used for any purposes other than those for which it was supplied
- be copied or reproduced in whole or in detail without the prior written consent of ARCS
- be disclosed to any third party without the prior written consent of ARCS.

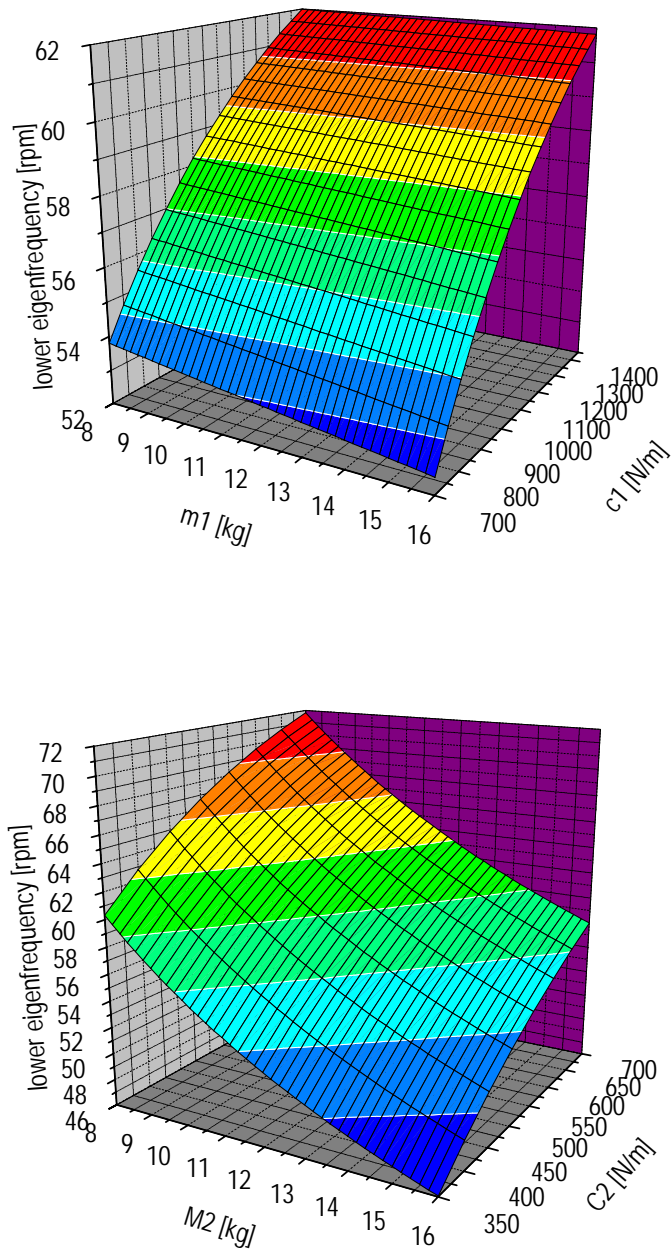


Figure 3.2-8 Influence of the Masses M_1 and M_2 as well as of the Spring Constants c_1 and c_2 on
Eigenfrequency ω_1

- be used for any purposes other than those for which it was supplied
- be copied or reproduced in whole or in detail without the prior written consent of ARCS
- be disclosed to any third party without the prior written consent of ARCS.

From these figures, it can be concluded, that big masses and small spring constants are desirable. Unfortunately, for the springs along the z direction (axial direction in **Figure 3.2-5**), the springs are not only used for vibration isolation, but have also to carry the weight of the structure.

From the analysis of the available springs, it was found, that designing the sensor mounting structure to a net weight of 12 kg it is possible to reach an upper eigenfrequency in the order of 150 rpm (15 Hz). Using three springs for the support of the sensor mounting, this mass is compatible with commercial available springs with a spring constant of 0.188 N/mm and a permitted total force of 40.956 N. In order to allow the usage of the same springs, the Mass M_2 was also designed to 12 kg, using 6 springs with the same properties as described above (Construction remark: length of the loaded spring: 44.3 mm; The radial isolation is done using springs with $k=0,105$ N/mm with an adjusted length of 45 mm excluding the adjustment space (including adjustment space (mounting whole distance is 60 mm) 55 mm).

For the further calculation, it was assumed, that the SCR and its support structure (having a total weight of 4 kg) has an asymmetry of 1 mm (this is obviously a drastic overestimation which can only happen due to problems in the cold bearing, more realistic would be an eccentricity of 0.2 mm which could happen due to movement of the axis and the SCR within the supporting structure). The mass of the whole experiment (including cryostat and cryostat mounting but excluding the oscillation parts) was assumed to be 50 kg.

The Matrix $\tilde{\Theta}$ can be calculated to be (note, as the formal solution is a quite complex expression, only the numeric solution is given here):

$$\tilde{\Theta} = \begin{pmatrix} 0.5773 & 0.2962 & -0.7608 \\ 0.5773 & -0.8070 & 0.1238 \\ 0.5773 & 0.5107 & 0.6369 \end{pmatrix} \quad (3.11)$$

- be used for any purposes other than those for which it was supplied
- be copied or reproduced in whole or in detail without the prior written consent of ARCS
- be disclosed to any third party without the prior written consent of ARCS.

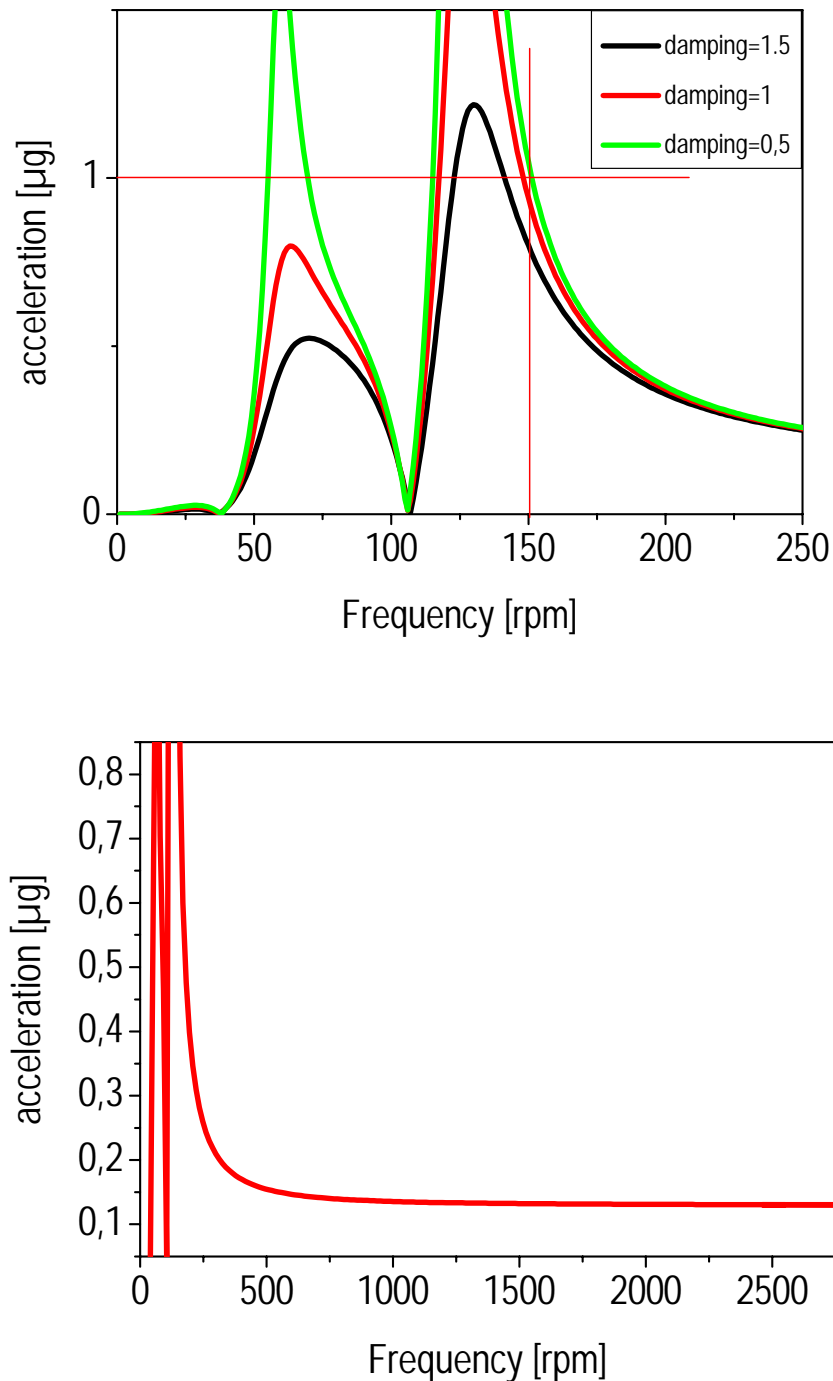


Figure 3.2-9 Low and High Frequency Part of the Acceleration Acting on the Accelerometers

It can be seen, that the noise level reaches $1 \mu g$ for motor speeds higher than 150 rpm. The graph shows the behavior for three different damping with $\delta_1=0.5$, $\delta_2=1.0$ and $\delta_3=1.5$. For the high frequency part, the damping is of no importance.

The same procedure can be done for the radial components. As the springs in this case are only used for adjusting the sensor mounting, the spring constant can be chosen to be much smaller. However, it has to be noted, that the sensor-mounting acts as physical pendulum. Therefore, the position of the springs has to be chosen carefully in order to prevent excitation of rotational modes of the system. Therefore, the working point of the springs was chosen, to be below the centre of gravity of the first and the second mass. In this case, the forces acting from the radial springs act in the opposite direction from the forces caused by the axial springs, minimizing the transmitted force.

Another source of acceleration comes from the torque of the motor itself, which is a step-like function. The problem with this acceleration is that it lies in the same plane as the signal proposed to be measured. As the signal from the SCR is assumed to increase linear with the acceleration of the disc, both contributions can not be separated from each other.

The transversal stiffness of spring 1 is $c_1 \sim 0.3 \text{ Nm/rad}$, and for c_2 the spring constant is 0.15 Nm/rad . The spring constant $c_0 \sim 1 \text{ Nm/rad}$. The moment of inertia corresponding to mass $M_0 = 5,4 \text{ kgm}^2$. The two isolation masses have moments of inertia of approximately 0.03 kgm^2 . The sensors are placed in a distance of 35 mm from the axis. The acceleration acting on the accelerometer due to this torque-step is shown in **Figure 3.2-10**.

- be used for any purposes other than those for which it was supplied
- be copied or reproduced in whole or in detail without the prior written consent of ARCS
- be disclosed to any third party without the prior written consent of ARCS.

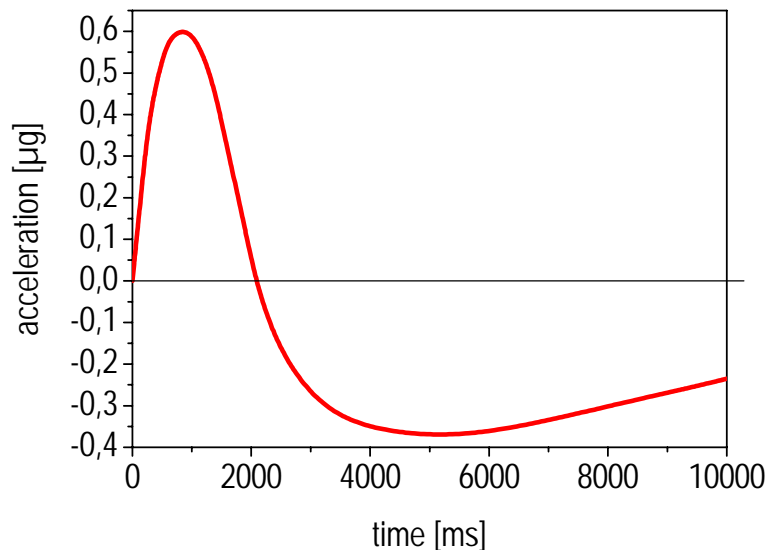


Figure 3.2-10 Acceleration acting on the accelerometer due to the step like acceleration or deceleration of the SCR. This picture was obtained by Fourier transformation of a quasi step like function, calculating the response of the system using the theory described above, and performing the inverse Fourier transformation back to time space.

It can be seen, that the acting acceleration due to the torque of the motor is less than 1 μg (even if the motor accelerates at its maximum torque). Nevertheless, this force acts irrespectively of whether the SCR is superconducting or not. Therefore calibration measurements with the SCR in the normal conducting state have to be done. Subtracting the thus obtained signals from the signals with the SCR cooled below TC eliminates the effect of this torque. Another reduction should be achieved, when subtracting the reference sensor from the signal sensor. As both sensors are placed at the same structure, the influence of the acceleration of the SCR should be strongly reduced. A careful analysis of this topic has to be done during the experiment.

Note, that this calculation is based on the assumption, that the whole structure is only 50 kg in weight, and is moving free in the air. When attaching a heavy ground plate, and fixing this plate with isolation elements to the laboratory ground, the influence can also be strongly decreased.

- be used for any purposes other than those for which it was supplied
- be copied or reproduced in whole or in detail without the prior written consent of ARCS
- be disclosed to any third party without the prior written consent of ARCS.

The spring adjustment is shown in **Figure 3.2-11**

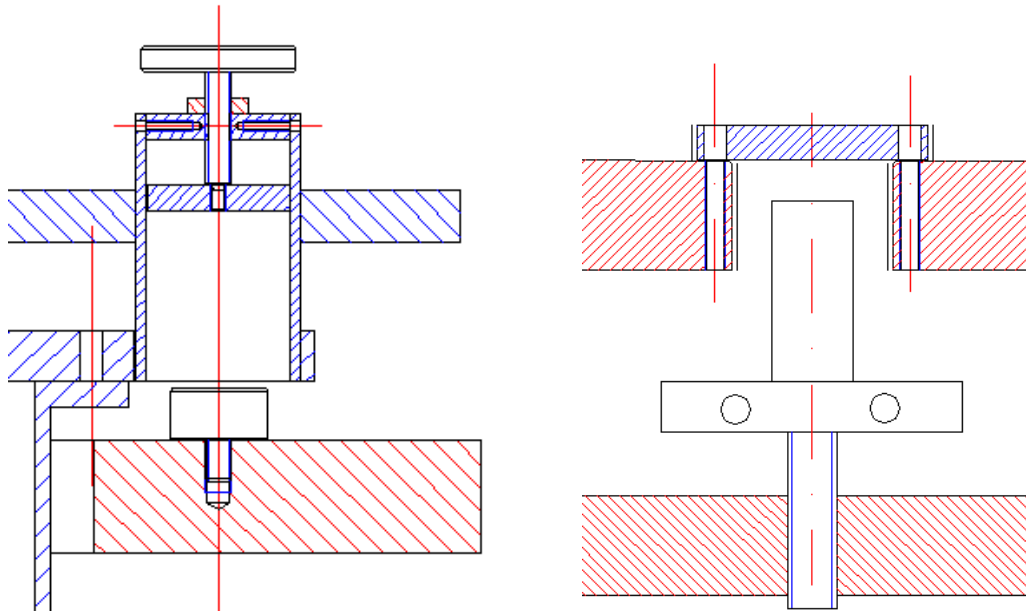


Figure 3.2-11 Spring adjustment. The two designs are the two axial adjustments, the radial adjustment is similar to the left figure.

- be used for any purposes other than those for which it was supplied
- be copied or reproduced in whole or in detail without the prior written consent of ARCS
- be disclosed to any third party without the prior written consent of ARCS.

3.3 Thermal Design

The calculation of the thermal properties is based on the formulas given in the VDI Wärmeatlas²⁸.

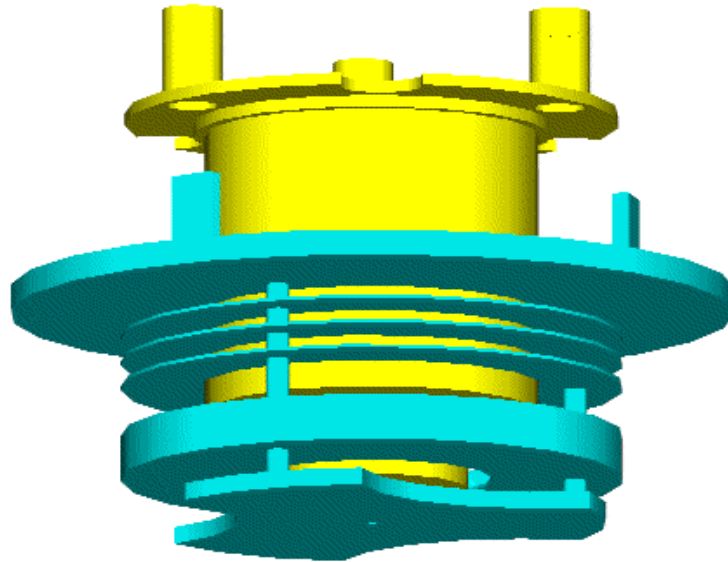


Figure 3.3-1 Sketch of the thermal relevant parts of the experimental setup.

The thermal isolation of the system has to fulfill two demands: first, the SCR has to be cooled well below T_C , and second, the accelerometers have to be placed in a (nearly) room temperature ambient (the temperature will be measured using PT 100 resistors for the three principal positions, each sensor will be placed in the vicinity of one to two PT 100 used for heating of the sensor surrounding keeping the sensor at room temperature). Therefore it was decided to place the accelerometers in a vacuum chamber equipped with a multilayer insulation. In the remaining space between cryostat and accelerometer cage, three to four radiation shields have to be placed. The cooling is done by pumping the cryogenic gas along the experimental setup. In order to constrict the costs of the coolant, a maximal cooling power of about 30 W@4.2 K should not be exceeded.

From the principal properties of a multilayer insulation (MLI), it can be assumed, that a maximum heating power of 12 W/m² for a temperature gradient of approximately 300 K (LHe cooling) can be reached. The whole surface of the sensor structure is about 0.1m², resulting in a thermal load of

about 1.2 W. This heat has to be cooled away on one side, but also to be supplied at the sensor mounting. This will be done using PT100 resistors.

In order to have some safety margin, for the further considerations, a thermal power of **3 W through the MLI** will be assumed.

The thermal radiation using four radiation shields is calculated by

$$\dot{q}_R = \sigma(T_h^4 - T_l^4) \frac{1}{\frac{2}{\varepsilon} - 1} \frac{1}{N+1} A \quad (3.12)$$

with T_h and T_l being the highest and lowest temperature. For this case, $T_h=300$ K and $T_l=4.2$ K is assumed. The Stefan Boltzmann constant $\sigma=5.67\text{W}/(\text{m}^2\text{K}^4)$. The reflectivity of the radiation shields is assumed to be $\varepsilon=0.2$. Using 4 shields with an area of $A=0.05$ m², the **thermal power due to radiation is approximately 1 W** (Note that the reflectivity of 0.2 is an underestimation, applying $\varepsilon=0.1$ reduces the radiation power to 0,5 W).

The heat conductance in the N₂ (He) gas is calculated using

$$\dot{q}_G = \lambda \frac{l}{A} \Delta T \quad (3.13)$$

with a thermal conductivity of the gas of approximately 0,084 Wm/K. The conducting area is the same as introduced in the calculation of the radiation. The length of the isolation shield is 100 mm (0.1 m). therefore, the thermal power from the **thermal conductivity of the gas is approximately 13 W**.

The heat conductance in the remaining structural parts is calculated using the same equation as given for the thermal conductance in the gas (However with changed cross-sections. The total cross section (including the axis, and the structural material needed for the support of the SCR and the radiation shields is $A=0.003\text{m}^2$. Therefore, the **heat transport through the structural material is approximately 4 W**.

The total heat transport through the experiment (neglecting the cryostat itself) is about 21 W, which is in the order of the design goal of the experiment. As the specific heat of N₂ is approximately 1 kJ/kg.K (for He its ~5.2 kJ/kg.K), the density of the gas is approximately 2 kg/m³ for N₂ (2 kg/m³ for He).

Both liquids have a density of approximately 1000 Kg/m³ at low temperature. Therefore, the gas/liquid fraction is approximately 260 for He, and 400 for LN₂. in order to reach a cooling of 30 W and a temperature of ~7 K (LHe, ; $\Delta T=5$ K, lowering of boiling temperature neglected) and ~80 K (LN₂; $\Delta T=10$ K, lowering of boiling temperature ~12 K), a consumption of 0,9 m³/h He-gas and a consumption of 3.8 m³/h N₂ gas is necessary, resulting in a consumption of 3,5 liter LHe/h and 4.5 liter LN₂/h. Therefore, the cryostat has to be capable to cover at least 30 l for a proper cooling and operation of the experiment.

3.4 Magnetic Fields

In order to subject the superconducting ring to an external magnetic field, a coil will be inserted in the experiment (see **Figure 3.4-1**). The coil can be removed completely without serious changes.

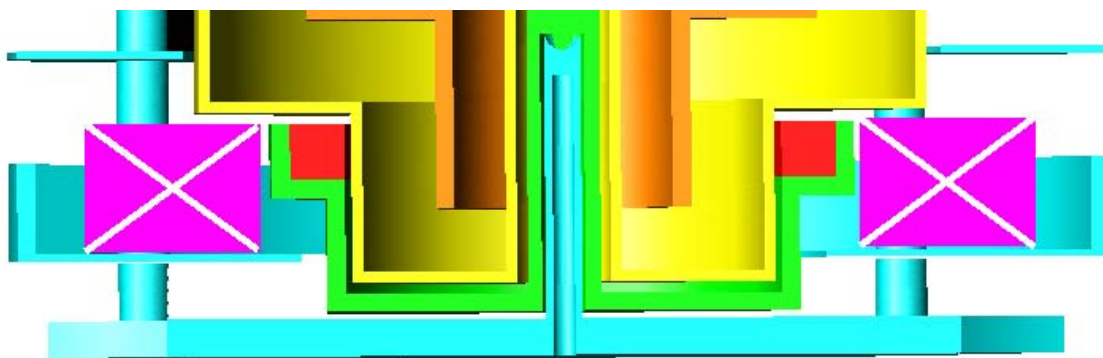


Figure 3.4-1 Magnetic field coil inside the experiment

- be used for any purposes other than those for which it was supplied
- be copied or reproduced in whole or in detail without the prior written consent of ARCS
- be disclosed to any third party without the prior written consent of ARCS.

Coil Parameters	Requirement
Strand diameter	1.5 mm
Number of winding	660
Cross section of coil	1665 mm ²
Resistance at 77 K	0.5 Ω
Resistance at RT	4.8 Ω
Maximum current	8A
Maximum field	65 mT

Table 3 Performance of the coil

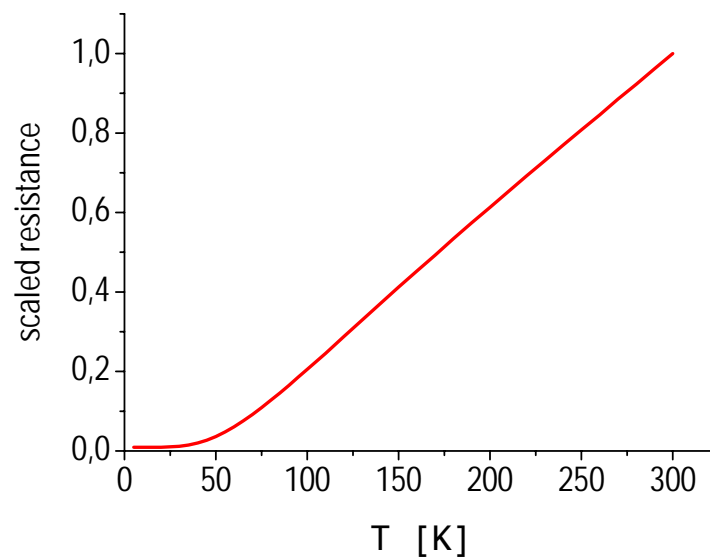


Figure 3.4-2 Resistance of copper as a function of temperature. The Debye temperature of copper is assumed to be 343 K. The room temperature conductivity is 100 %IACS corresponding to 58 MS/m.

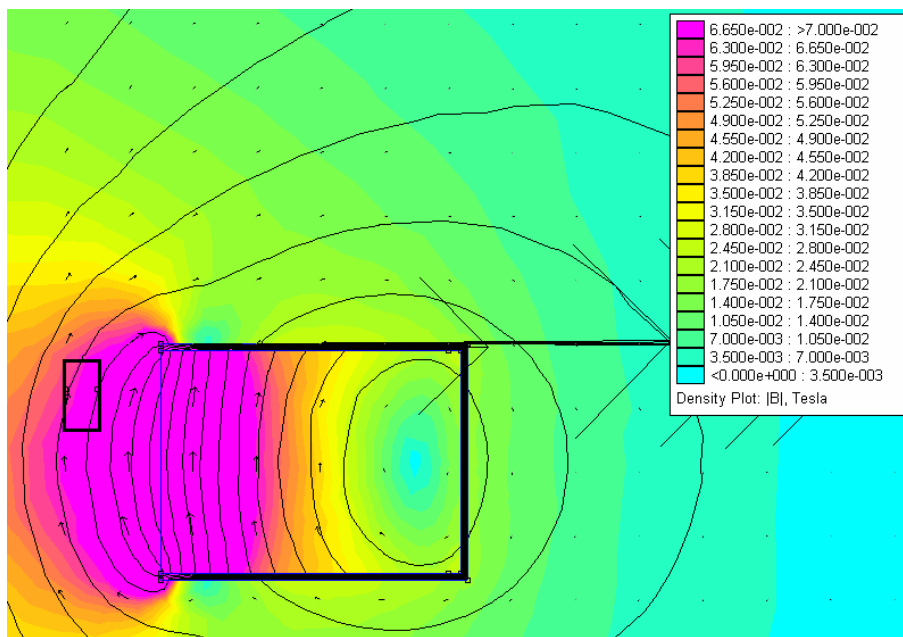


Figure 3.4-3 Calculation of the magnetic field distribution

The parameters of the coil are given **Table 3**. The change in the resistance due to the lowered temperature can be estimated from **Figure 3.4-2**. The maximum magnetic field (for operation at 8 A) was calculated to be 65 mT (see **Figure 3.4-3**). In order to reach this field, the coil has to be shielded by silicon core iron (without shielding the field is reduced to 45 mT).

Operating the coil at the given parameters results in an heat production of ~33 W yielding an additional coolant consumption of ~6l/h. The situation becomes better when cooling to lower temperature (e.g. Helium temperature), where the resistance is lowered to about 0.05 Ω resulting in an additional coolant consumption of 1 l/h.

The magnetic signal of the superconductor resulting from the London moment will be measured using a DC Milligauss Magnetometer produced by AlphaLab Inc. The Gauss-meter has a resolution of 1 nT, and a full range of 200 μ T. For the measurement of the magnetic field produced by the field coil, commercially available hall-probes will be used.

- be used for any purposes other than those for which it was supplied
- be copied or reproduced in whole or in detail without the prior written consent of ARCS
- be disclosed to any third party without the prior written consent of ARCS.

3.5 Electric connectors

In order to read the signal of the accelerometers, a 20 pin electric connection is needed. For the temperature control of the accelerometers, additional 8 pins are needed. For the Gauss-meter and the Hall probe additional 12 pins are needed. Therefore, two LEMO-vacuum connectors with 22 pins each will be used (HGP.4S.322.CLLPV). Using these connectors, a spare of 4 pins to the vacuum chamber is available for later upgrades, or improvements of the electric design.

- be used for any purposes other than those for which it was supplied
- be copied or reproduced in whole or in detail without the prior written consent of ARCS
- be disclosed to any third party without the prior written consent of ARCS.

3.6 Expected Performance in Laboratory Environment

The expected performance based on the design outlined in the chapters before is summarized in **Table 4**, which is fully compliant to the requirements.

	Requirement	Expected Performance
Resolution of Acceleration Sensor	1 μg	0.3 μg
Angular Acceleration of Superconductive Ring	$> 200 \text{ s}^{-2}$	380 s^{-2} Peak: 1700 s^{-2}
Minimum Measurement Time	1 s	3 s
Maximum Rotational Speed of Superconductive Ring	3000 rpm	$> 3000 \text{ rpm}$ 5800 rpm are possible (the mechanical stability has to be checked)
Temperature of Superconductive Ring	$< 77 \text{ K}$	70 K

Table 4 Summary of Requirements and Expected Performance for Experimental Facility

- be used for any purposes other than those for which it was supplied
- be copied or reproduced in whole or in detail without the prior written consent of ARCS
- be disclosed to any third party without the prior written consent of ARCS.

4 TEST PLANS

4.1 Test Plan for Validation of Design

As the goal which should be reached by this experiment are quite challenging, an extensive test phase for the validation of the experiment has to be performed before running the actual experiments.

- 1) During the manufacturing of the experimental parts, the accelerometers should be placed where the experiment should be carried out. A long term monitoring of the vibrations of the surrounding, as well as a test of the stability of the accelerometers should be gained from this. As three accelerometers are measuring the same direction, the differences between the accelerometers can be checked (the axes of the accelerometers should be changed in that way, that there is a period for which each accelerometer has measured the same direction as an any other). Special care should be taken to the periods which are of particular interest for the experimental phases (late night and weekend).
- 2) The mechanical stability of the rotational system has to be checked. Therefore a dummy ring with the same mass has to be placed in the position of the SCR. The accelerometers must not be mounted at this time. Several acceleration and acceleration tests should be done. The first test shall be done at room temperature, to permit full access to the structure. Later tests shall be done at cryogenic temperature to identify possible thermal problems before the experiment. The heat control system A and D has to be installed.
- 3) In the meantime, the evacuated sensor mounting can be tested if the isolation is sufficient to prevent the accelerometers from thermal destruction (therefore the heat control system B and C have to be installed).
- 4) Finally, a test with the dummy superconductor should be done, to check the influence of the vibrations and the acceleration of the superconductor on the accelerometers (see **Figure 3.2-9** and **Figure 3.2-10**). This test could also be done using the already mounted superconductor. The decision if the dummy or the real conductor will be used will be taken after tests 1 - 3. One of the results of this test should also be the time between two accelerations which is necessary to allow the decay of oscillations.

4.2 Test Plan for Experiment

For the experimental case, it is proposed to start at the lowest temperature achievable with the experiment at liquid nitrogen. The signal of the superconducting ring when decelerating from a mean rotational speed (which has to be taken from the validation tests) should be measured, starting with a low deceleration speed (due to safety considerations). The same test should be performed with the same acceleration (the same value of angular acceleration but opposite sign). Subsequently, the experiment should be repeated with increasing acceleration (deceleration) speed up to the upper safe limit of the experiment obtained from the validation phase.

The same procedure should be repeated at several temperatures till the normal conducting state of the superconductor is reached. As the design of the experiment should also allow to perform experiments at lower temperatures, it is proposed to perform also some experiments using the HTC ring at temperatures below 50 K (see **Figure 2.2-5**). This experiments would require liquid He, as nitrogen solidifies at 63 K, therefore a temperature lowering using the enthalpy of evaporation stops at temperatures higher than around 70 K (or at least the cooling power converges toward zero).

- be used for any purposes other than those for which it was supplied
- be copied or reproduced in whole or in detail without the prior written consent of ARCS
- be disclosed to any third party without the prior written consent of ARCS.

5 REFERENCES

[Airmotors] <http://www.duesterloh.de/deutsch/hydraulikmotoren/hydraulikmotoren.html>

http://www.dynatork.co.uk/index_flash.htm

http://www.kinequip.com/airmotors.asp?Cat_Id=9#

<http://www.psiautomation.com/>

Private communication

[Applied Mems] http://www.appliedmems.cc/htmlmems/p_si_flex.html; private communication

[Böge 1989] Böge A, Das Techniker Handbuch – Band 1; Vieweg&Sohn (1989)

[De Matos et al. 2001] De Matos, C. J., and Tajmar, M., "Gravitomagnetic Barnett Effect", *Indian Journal of Physics* **75B**(5), 2001, pp. 459-461 (also gr-qc/0012091)

[Escher et al. 1996] Escher U., Samuel R., Gladun A., Hegenbarth E., The influence of SrSO₄ additives to Bi₂Sr₂CaCu₂O₈ high temperature Superconductors. *Physica B* **219-220** (1996), 189-191

[Hense 1999/2002] Hense K, Gitterdynamik in der orthorhombischen Struktur YCu₂, TU Wien
Diplomathesis 1999

Hense K, CEF phonon interaction in the orthorhombic compound NdCu₂, TU Wien, PhD thesis 2002

[Hense 2002] Hense K et al. Influence of the annealing time of internal tin Nb₃Sn strands on the critical current and the magnetization losses; *Physica C* **372-276** (2002) pp 1758-1761

[Hense 2004] Hense K. et al., Scaling behavior for the exponents of U-I-, U-B- and U-T – measurements, *Physica C* **401** (2004) 214-217

[Honeywell] <http://www.inertialsensor.com/qa3000.shtml> ; private communication

[Keithley] <http://www.keithley.com/main.jsp?action=keithleysearch>

- be used for any purposes other than those for which it was supplied
- be copied or reproduced in whole or in detail without the prior written consent of ARCS
- be disclosed to any third party without the prior written consent of ARCS.

[MWS] <http://www.mws-sensorik.de/pdf/5401.pdf> ; private communication

[Silicon Designs] <http://www.silicondesigns.com/1221.html>; private communication

[Tajmar et al. 2001] Tajmar, M., de Matos, C.J., "Coupling of Electromagnetism and Gravitation in the Weak Field Approximation", *Journal of Theoretics*, **3**(1), February 2001 (also gr-qc/0003011)

[Tajmar et al. 2003] Tajmar, M, de Matos, C. J., "Gravitomagnetic field of a rotating superconductor and of a rotating superfluid", *Physica C*, **385**, 2003, pp. 551-554

[Tate et al. 1989] Tate, J., Cabrera, B., Felch, S.B., Anderson, J.T., "Precise Determination of the Cooper-Pair Mass", *Physical Review Letters*, **62**(8), 1989, pp 845-848

[Tate et al. 1990] Tate, J., Cabrera, B., Felch, S.B., Anderson, J.T., "Determination of the Cooper-Pair Mass in Niobium", *Physical Review B*, **42**(13), 1990, pp 7885-7893

[Torquesystems] <http://www.torquesystems.com>; private communications

[VDI1997] VDI Wärmeatlas; Springer Verlag Berlin Heidelberg (1997)

- be used for any purposes other than those for which it was supplied
- be copied or reproduced in whole or in detail without the prior written consent of ARCS
- be disclosed to any third party without the prior written consent of ARCS.

POSSIBLE GRAVITATIONAL ANOMALIES IN QUANTUM MATERIALS

Phase II: Experiment Assembly, Qualification and Test Results

Award No. FA8655-03-1-3075

Date: 15. 09. 2005

Prepared by: M. Tajmar, ARC Seibersdorf research

- be used for any purposes other than those for which it was supplied
- be copied or reproduced in whole or in detail without the prior written consent of ARCS
- be disclosed to any third party without the prior written consent of ARCS.

ABSTRACT

The author recently published a paper, suggesting for the first time that a reported disagreement between experimental measurements and theoretical predictions for the magnetic field in rotating superconductors might arise from an anomalous high-order gravitomagnetic contribution (also known as frame dragging or Lense-Thirring effect). In normal matter, the ratio between electromagnetic and gravitational fields is given by the difference in the respective permeabilities. However, magnetic fields generated as a consequence of the quantization of the canonical momentum in a superconductor do not depend on the permeability. Hence, there is the possibility that the ratio between those two fields might be different in a quantum material. Latest theoretical work links the generation of those non-classical gravitomagnetic fields to the ratio between the Cooper-pair mass and the bulk density of the superconductor.

This report summarizes the work carried out in Phase II – the assembly of the experiment, qualification to make sure that the required sensitivity can be met, and finally the report on the test results using BSCCO and YBCO superconductors as well as Niobium as a dummy at liquid nitrogen temperatures. The measurements show that the resolution level is low enough to test the original conditions defined in Phase I (derived from Tate's Cooper-pair measurements), however, the resolution is about one order of magnitude above the theoretical predictions for high-temperature superconductors. No gravitational anomalies were found for BSCCO and YBCO down to the facility resolution level. Hence, gravitational fields based on Tate's measurement have not been found with high-temperature superconductors. However, the results do not rule out such gravitational anomalies at their theoretically predicted lower values or anomalies using Tate's original setup (Niobium superconductor and liquid helium temperatures).

I certify that there were no subject inventions to declare, during the performance of this grant.

- be used for any purposes other than those for which it was supplied
- be copied or reproduced in whole or in detail without the prior written consent of ARCS
- be disclosed to any third party without the prior written consent of ARCS.

TABLE OF CONTENT

1	Theoretical Predictions	4
1.1	Large Gravitomagnetic Fields based on Tate's Results	4
1.2	Gravitomagnetic Fields Depending on Superconductor Material	6
1.3	Coupling Factor Expected in Experiment	8
2	Experiment Assembly	10
2.1	Introduction	10
2.2	Sensor-Vacuum Chamber	11
2.3	Damping System	13
2.4	Motor and Coil Assembly	16
2.5	Superconductor Support and Axis	18
2.6	Cryostat Assembly	19
2.7	Electrical Setup	22
2.8	Data Acquisition and Control Program	23
2.9	Data Analysis Program	25
3	Experimental Results	27
3.1	Introduction	27
3.2	Sensor External Influence	28
3.3	Facility Calibration with Niobium Dummy	33
3.4	BSCCO Coupling Factor Evaluation	38
3.5	YBCO Coupling Factor Evaluation	43
4	Discussion	48
5	Conclusions	50
	References	51

1 THEORETICAL PREDICTIONS

1.1 Large Gravitomagnetic Fields based on Tate's Results

The experiment is designed to test the hypothesis, that large gravitomagnetic fields are responsible for the Cooper-mass anomaly measured by Tate et al (Tate et al, 1989, 1990). In a rotating superconductor (see **Figure 1.1-1**), the integral of the canonical momentum is quantized. In the case of a superconductive ring, if the ring's thickness is larger than the London penetration depth (usually in the order of 100 nm), then the integral can be set to zero,

$$\oint \vec{p}_S \cdot d\vec{l} = \oint (m\vec{v}_S + e\vec{A}) \cdot d\vec{l} = 0, \quad (1)$$

where m and e are the mass and charge of the Cooper-pair, \vec{A} the magnetic vector potential, and \vec{v}_S the speed of the Cooper-pairs.

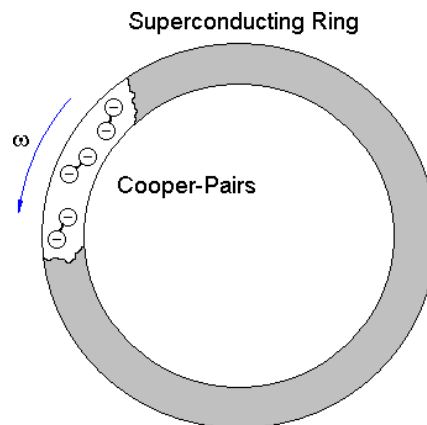


Figure 1.1-1 Rotating Superconductor

If a superconductor that was cooled down at rest ($v_S=0$) is now set into rotation (i.e. , $v_S \neq 0$), then it has to build up a magnetic field to still fulfill Equ. (1). One can easily transform Equ. (1) into

$$\vec{B} = -\frac{2m}{e} \vec{\omega}. \quad (2)$$

This is called the London moment. It is remarkable, because a magnetic field is generated without the permeability μ_0 , which appears in all classical equations involving the magnetic fields.

By accurately measuring the magnetic field of a rotating superconductor (e.g. by using a SQUID) and the angular velocity ω , one can calculate the mass of the Cooper-pair (as the charge is always two times the elementary charge). This has been done for a number of superconductors (Tajmar et al, 2005 and references therein), the most important result was that the Cooper-pair mass is very close to two times the electron mass independent on the material used. Tate et al performed the most accurate

- be used for any purposes other than those for which it was supplied
- be copied or reproduced in whole or in detail without the prior written consent of ARCS
- be disclosed to any third party without the prior written consent of ARCS.

experiment up to now (Tate et al, 1989, 1990) revealing that the Cooper-pair mass is $m^*/2m_e = 1.000084(21)$ actually a little bit larger than two times the electron mass. This is even more a surprise as quantum theory including relativistic corrections expects the Cooper-pair mass to be a little bit smaller than two times the electron mass $m^*/2m_e = 0.999992$. The difference between experiment and theory is more than 4 sigma! This anomaly was discussed in the literature without any apparent solution (Tajmar et al, 2005 and references therein). It is even more striking that such a mass increase is simply impossible from a thermodynamic point of view.

Therefore, something must be wrong – or putting in better words – not complete. Therefore Tajmar et al recently suggested (Tajmar et al, 2003) that Equ. (1) must be replaced by the full canonical momentum equation. This is not new and was first noted by DeWitt in the 1960s (DeWitt, 1966). The full canonical momentum in Equ. (1) leads to

$$\oint \vec{p}_s \cdot d\vec{l} = \oint (m\vec{v}_s + e\vec{A} + m\vec{A}_g) \cdot d\vec{l} = 0 , \quad (3)$$

where \vec{A}_g is the gravitomagnetic vector potential. Applying it to our case of a rotating superconductor, we get

$$\vec{B} = -\frac{2m}{e} \cdot \vec{\omega} - \frac{m}{e} \cdot \vec{B}_g . \quad (4)$$

Comparing with Equ. (2), this shows that a rotating superconductor is generating a gravitomagnetic field in addition to a magnetic field. Using Tate's experimental values and the theoretical predictions (Tajmar et al, 2005), we get the gravitomagnetic field that is necessary to correct Tate's result and to comply with quantum theory

$$\vec{B} = 2\vec{\omega} \left(\frac{\Delta m}{m} \right) = 1.84 \times 10^{-4} \vec{\omega} , \quad (5)$$

where Δm is the difference between experimental and theoretical Cooper-pair mass. If Tate's result is correct and quantum theory holds, then a rotating superconductor can indeed produce a gravitomagnetic field which is many orders of magnitude above the non-coherent matter result.

It is important to note that Equ. (5) was derived for Tate's setup, i.e. using a 40 nm thick Niobium ring rotating at a maximum frequency of 5 Hz at a temperature of 6 K. How will Δm change if we use a material different than Niobium? The Phase I design of this experiment was centered around a high-temperature superconductor made out of BSCCO tested together with liquid nitrogen – for simplicity and cost reasons. Can we still expect the same gravitomagnetic field in this experiment as the one derived from Tate's measurement?

- be used for any purposes other than those for which it was supplied
- be copied or reproduced in whole or in detail without the prior written consent of ARCS
- be disclosed to any third party without the prior written consent of ARCS.

1.2 Gravitomagnetic Fields Depending on Superconductor Material

Only very recent theoretical progress enables us to predict the gravitomagnetic field generated by different superconductor materials.

In modern Quantum Field Theory (QFT) superconductivity is explained in the following way: As a superconductor is passing its critical temperature, gauge symmetry is broken. This causes the photon to acquire mass via the Higgs mechanism (Ryder, 2003). The London penetration depth that we observe is then just the wavelength of the massive photon ($\lambda_L = \lambda_{\text{photon}}$). One consequence of a massive photon is that the Maxwell equations transform into the Proca equations with two additional terms,

$$\begin{aligned} \text{div } \vec{E} &= \frac{\rho}{\epsilon_0} - \left(\frac{m_{\text{photon}} c}{\hbar} \right)^2 \cdot \varphi & (6) \\ \text{div } \vec{B} &= 0 \\ \text{rot } \vec{E} &= - \frac{\partial \vec{B}}{\partial t} \\ \text{rot } \vec{B} &= \mu_0 \rho \vec{v} + \frac{1}{c^2} \frac{\partial \vec{E}}{\partial t} - \left(\frac{m_{\text{photon}} c}{\hbar} \right)^2 \cdot \vec{A} \end{aligned}$$

The author has recently shown (de Matos et al, 2005) that by taking the rotational of the 4th equation and solving the differential equation, the photon mass reveals the two basic features of superconductivity: exponential shielding of electromagnetic fields (Meissner-Ochsenfeld effect) and the generation of a magnetic field by rotation (London moment with $\lambda_L = \lambda_{\text{photon}}$),

$$\vec{B} = \vec{B}_0 \cdot e^{-\frac{x}{\lambda_{\text{photon}}}} - 2\omega \frac{m}{e} \left(\frac{\lambda_{\text{photon}}}{\lambda_L} \right)^2. \quad (7)$$

In a typical superconductor, the photon mass is then about 1/1000 of the electron mass. We see that the mass of the photon is responsible for the London moment. If the photon is so massive, why shall the graviton in a superconductor not be massive as well – leading to a gravitomagnetic London moment that we need to match Tate's Cooper-pair mass anomaly?

The Proca equations can be also expressed for gravitational fields modifying the Einstein-Maxwell equations used in the weak field approximation. Following the same arguments as above, we get,

$$\vec{B}_g = \vec{B}_{g0} \cdot e^{-\frac{x}{\lambda_g}} - 2\omega \left(\frac{\lambda_g}{\lambda_{Lg}} \right)^2, \quad (8)$$

- be used for any purposes other than those for which it was supplied
- be copied or reproduced in whole or in detail without the prior written consent of ARCS
- be disclosed to any third party without the prior written consent of ARCS.

where $\lambda_g = \frac{\hbar}{m_g c}$ is the graviton Compton wavelength, and the second term in Equ. (10) can be interpreted as a gravitomagnetic London moment, just as we need to match Tate's Cooper-pair anomaly (compare with Equ. 5!). The gravitomagnetic penetration depth λ_{Lg} is defined as (de Matos, 2004)

$$\lambda_{Lg} = i \sqrt{\frac{1}{\mu_{0g} n_s m}} \quad (9)$$

where n_s is the Cooper-pair density. Both the penetration depth as well as the graviton wavelength is a complex number, as required by the positive cosmological constant measured in our universe (Novello et al, 2003). Using Tate's result, we can compute the value of the graviton mass inside a Niobium superconductor as

$$m_g = i \cdot \sqrt{\frac{\mu_{0g} n_s m^2 \hbar^2}{c^2 \Delta m}} = i \cdot 4.61 \times 10^{-55} \text{ kg} \quad (10)$$

This is "only" 14 orders of magnitude above its accepted free-space value from the cosmological constant measurement of $i \cdot 10^{-69}$ kg (De Matos et al, 2005), but it is still a small number. In a recent assessment, Modanese (Modanese, 2003) calculated the cosmological constant inside a superconductor taking into account the contribution of the Ginzburg-Landau wave function ψ_{GL} to the Lagrangian. He found that in the case of a Pb superconductor, the cosmological constant should be on the order of 10^{-39} m^{-2} . That would lead to a complex graviton mass of $i \cdot 10^{-62}$ kg, coming closer to our estimate of $i \cdot 10^{-55}$ kg in a Nb superconductor. By comparing Eqs. (5) and (8), we find that

$$\frac{\Delta m}{m} = \left(\frac{\lambda_g}{\lambda_{Lg}} \right)^2 \quad (11)$$

Hence, the delta of mass measured by Tate is just an expression of the ratio between the graviton wavelength and its penetration depth inside a superconductor.

In our very last theoretical assessment (Tajmar et al, to be published), we were able to further express the graviton wavelength inside the superconductor and express Equ (11) by

$$\frac{\Delta m}{m} = \frac{\rho_s}{\rho_{bulk}} \quad (12)$$

where ρ_s is the Cooper-pair mass density and ρ_{bulk} the bulk density of the superconductor. The following table compares the results expected from Tate's setup to the conditions of high-temperature superconductors and liquid nitrogen as used in our experimental setup.

- be used for any purposes other than those for which it was supplied
- be copied or reproduced in whole or in detail without the prior written consent of ARCS
- be disclosed to any third party without the prior written consent of ARCS.

Material	Temperature [K]	Bulk Density [kg.m ⁻³]	Cooper-Pair	
			Mass Density [kg.m ⁻³]	$\Delta m / m$
Niobium	6	8570	5.64×10^{-2}	6.58×10^{-6}
YBCO	77	6133	2.06×10^{-3}	3.35×10^{-7}
BSCCO (2212)	77	5400	7.57×10^{-4}	1.40×10^{-7}

Table 1 Expected Theoretical $\Delta m/m$ for Different Materials

We see that the theory ($\Delta m/m=6.58 \times 10^{-6}$) already comes quite close, within a factor 11, to our derived value from Tate's experiment ($\Delta m/m=9.2 \times 10^{-5}$) in case of Niobium at 6 K. The Δm is the difference between the theoretically expected and measured Cooper-pair mass, so additional theoretical corrections factors, already proposed by a number of papers (e.g. Capelle et al, 1999), might close the gap to our theoretical prediction.

1.3 Coupling Factor Expected in Experiment

The experiment can not measure the gravitomagnetic field predicted for rotating superconductors directly, but the induced gravitational field due to acceleration of the ring.

Using the gravitational induction law,

$$\text{rot } \vec{g} = \frac{\partial \vec{B}_g}{\partial t} , \quad (13)$$

and Equ. (5), we can express the gravitational field measured at the radial distance r (if $r <$ superconductor ring radius) by expanding Equ. (13),

$$\iint \text{rot } \vec{g} \cdot d\vec{A} = \oint \vec{g} \cdot d\vec{l} = - \iint 2\dot{\omega} \frac{\Delta m}{m} \cdot d\vec{A} , \quad (14)$$

and finally get for the one-dimenaional case

$$g = -\dot{\omega} r \frac{\Delta m}{m} . \quad (15)$$

For the experiment it is useful to define a coupling factor of the induced gravitational field versus the applied acceleration. For field units in terms of the standard Earth's gravitational acceleration (9.81 m.s^{-2}), we get

$$\frac{g}{\dot{\omega}} = - \frac{r}{9.81} \frac{\Delta m}{m} . \quad (16)$$

The gravitational field, following the vectorial equations, should point in the opposite direction of the applied angular acceleration (tangential). The following table summarizes the predicted coupling factors for the In-Ring Sensors ($r=4$ cm) based on Tate's measurement and our theory.

- be used for any purposes other than those for which it was supplied
- be copied or reproduced in whole or in detail without the prior written consent of ARCS
- be disclosed to any third party without the prior written consent of ARCS.

Material	Condition	Temperature [K]	Predicted Angular Acceleration Coupling Factor [s ² .rad ⁻¹]
Niobium	From Tate's Experiment	6	-3.7x10 ⁻⁷
Niobium	From Theory	6	-2.7x10 ⁻⁸
YBCO	From Theory	77	-1.4x10 ⁻⁹
BSCCO (2212)	From Theory	77	-5.7x10 ⁻¹⁰

Table 2 Expected Coupling Ratios for Different Materials

This shows that the coupling factor to be investigated by the experiment with high-temperature superconductors can be 2-3 orders of magnitude below the one derived from Tate's measurement, which was the basis for the design. Still, even the reduced coupling factors would lead to gravitational fields 20 orders of magnitude above classical values and are therefore very interesting for technological applications.

- be used for any purposes other than those for which it was supplied
- be copied or reproduced in whole or in detail without the prior written consent of ARCS
- be disclosed to any third party without the prior written consent of ARCS.

2 EXPERIMENT ASSEMBLY

2.1 Introduction

The experimental facility was initially manufactured, assembled and tested according to the original design plan of Phase I. However, extensive testing made the following two major changes necessary:

- Replacement of the Silicon Designs 1221 accelerometers with AppliedMEMS SF1500S accelerometers. The new accelerometers have a higher resolution (see **Figure 2.1-1**) and are less sensitive to magnetic fields that are coming from the electric motor (components of accelerometers are made out of non-magnetic components).

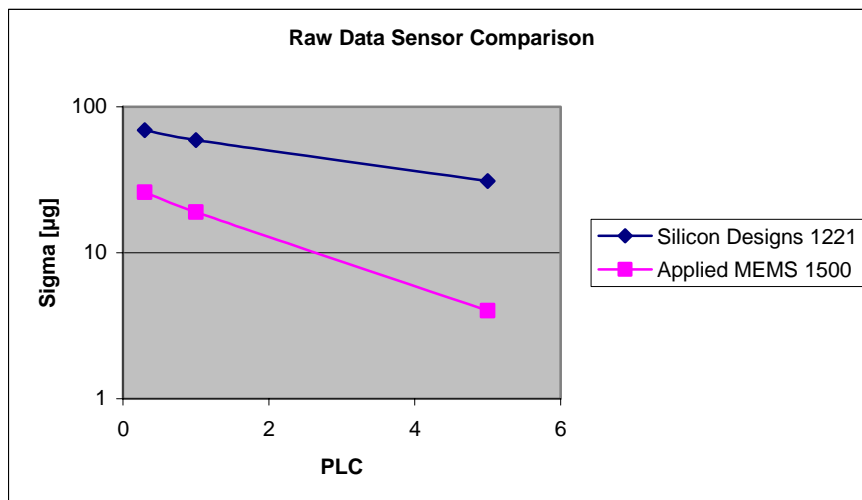


Figure 2.1-1 Sensor Noise Comparison for different Power Line Cycles (1 PLC corresponds to 20 ms)

- The damping system for the sensor-vacuum chamber had to be replaced by a fixed structure, mounted on the ground and roof, in order to efficiently stop the transmission of noise due to the rotation of the superconducting ring to the sensors. With the damping system, a noise level on the sensors of ± 2 mg was observed during full rotation, which is at least one order of magnitude larger than the predicted effect (derived from Tate's experiment at maximum angular acceleration). In the fixed configuration, no effect due to the rotation of the superconductor could be seen any more and a noise level of about 20 μg was obtained at a sampling frequency of 10 Hz.

The following sections show step-by-step how the experimental facility was assembled.

2.2 Sensor-Vacuum Chamber

Three AppliedMEMS 1500S accelerometers (X-, Y, and Z-direction) were mounted on the three measurement positions (9 in total):

- above the superconductor (2.5 cm at a radial distance of 7.5 cm),
- inside the superconductor (at a radial distance of 4 cm),
- on reference position (20.5 cm above superconductor at a radial distance of 4 cm).

Next to each accelerometer, a Kapton heater foil was mounted for maintaining a temperature of 25°C at each sensor. Moreover, each measurement position (above ring, inner ring, reference) was equipped with a PT-100 element for temperature measurement. **Figure 2.2-1** shows one accelerometer and a heater on the structure.

In addition to the accelerometers, high-resolution fluxgate magnetic field sensors (Stefan Mayer Instruments FL1-100) were mounted on the In-Ring and Reference positions. These sensors replaced the originally proposed AlphaLab Milligauss Magnetometer due to their higher resolution (20 pT/Hz^{0.5} at 1 Hz) and stability.

All elements, including the magnetic field sensor, were fixed using the STYCAST 2850FT two component vacuum compatible epoxy glue. The cables were fixed using Teflon tape. The completely assembled sensor structure is shown in **Figure 2.2-2** (left). Next, the Multi-Layer-Insulation (MLI) was carefully wrapped around the structure and again fixed with Teflon tape.

Then, LEMO connectors were mounted and sealed, the cables soldered to the connector, and all sensors were finally checked. Afterwards, the complete vacuum chamber was assembled and connected to a roughing pump-turbo pump system using the pump-out port (see **Figure 2.2-3**). The vacuum chamber was evacuated over night until a pressure of 3×10^{-6} mbar was reached. In addition, before the final pump down, no leaks were detected using a Helium leak detector.

- be used for any purposes other than those for which it was supplied
- be copied or reproduced in whole or in detail without the prior written consent of ARCS
- be disclosed to any third party without the prior written consent of ARCS.

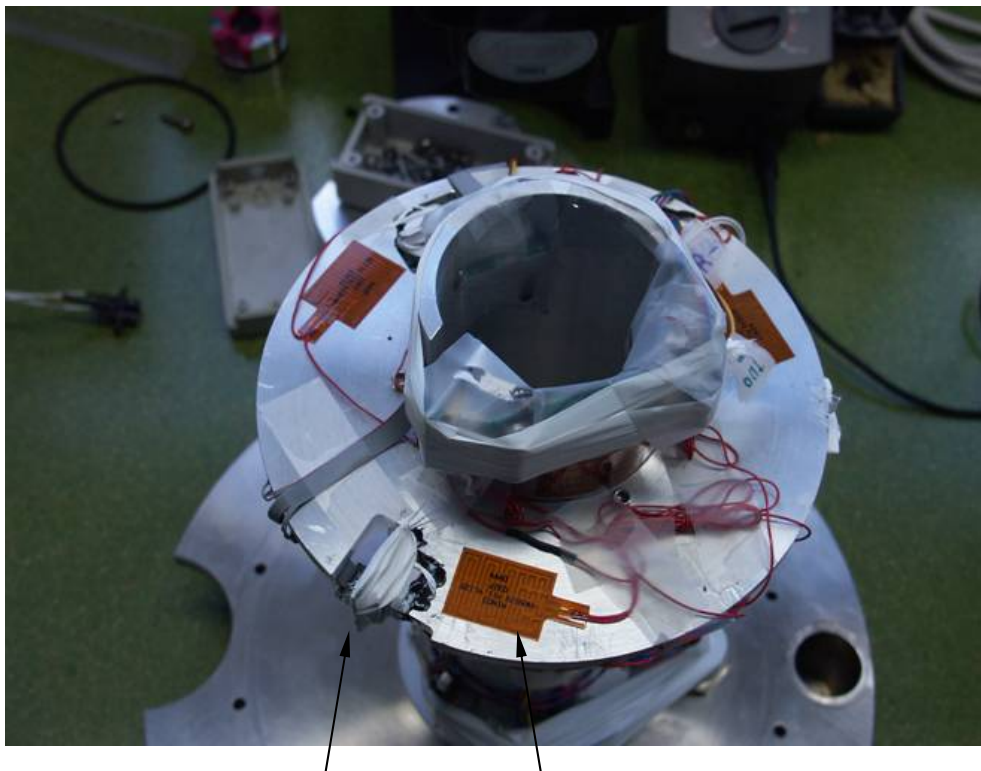


Figure 2.2-1 Accelerometers and Kapton Heater Foils Mounted on Structure

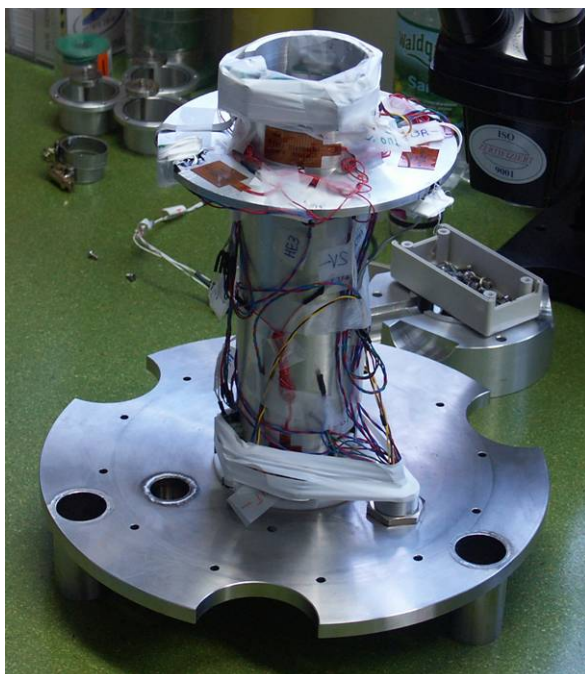


Figure 2.2-2 Complete Assembly of Accelerometers, Heaters, PT-100s and Magnetic Field Sensor on Structure (Left) and Wrapped in MLI Insulation (Right)

- be used for any purposes other than those for which it was supplied
- be copied or reproduced in whole or in detail without the prior written consent of ARCS
- be disclosed to any third party without the prior written consent of ARCS.



Figure 2.2-3 Completely Assembled Vacuum Chamber

2.3 Damping System

The following section explains the assembly of the original damping system – which was later replaced by the fixed structure.

First, the flange assembly with the radiation shields was assembled (see **Figure 2.3-1**). Then, the radial dampers that go to the copper ring were mounted (see **Figure 2.3-2**). A wire was used to pre-squeeze the spring and release it after the next sub-assembly.

Next, the copper ring with its radial dampers that go on the sensor vacuum-chamber was assembled (see **Figure 2.3-3**). Then, the copper ring was mounted on the flange, which is the first stage of the damping system (see **Figure 2.3-4**). Teflon hollow shafts were put inside the springs as a support to avoid jumps of the copper ring and to bring it to the center position. These Teflon shafts are believed to be most likely responsible for the large noise detected as they transmit part of the cryostat vibrations to the sensors.

Finally, the sensor-vacuum chamber was mounted as shown in **Figure 2.3-5**.

- be used for any purposes other than those for which it was supplied
- be copied or reproduced in whole or in detail without the prior written consent of ARCS
- be disclosed to any third party without the prior written consent of ARCS.



Figure 2.3-1 Flange Assembly

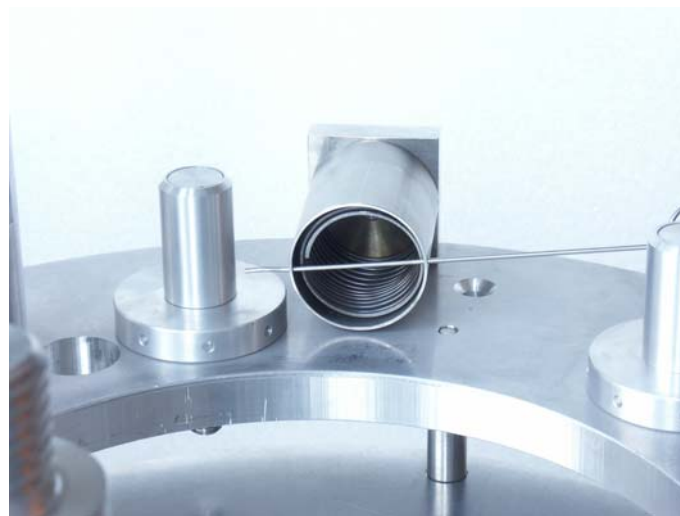


Figure 2.3-2 Flange Radial Damper

- be used for any purposes other than those for which it was supplied
- be copied or reproduced in whole or in detail without the prior written consent of ARCS
- be disclosed to any third party without the prior written consent of ARCS.



Figure 2.3-3 Copper Ring Assembly



Figure 2.3-4 Copper Ring-Flange Assembly (With Shaft and Superconductor Support Structure)

- be used for any purposes other than those for which it was supplied
- be copied or reproduced in whole or in detail without the prior written consent of ARCS
- be disclosed to any third party without the prior written consent of ARCS.



Figure 2.3-5 Complete Damping System Assembly

2.4 Motor and Coil Assembly

In order to test the assembly before mounting it on the cryostat (to avoid possible damage), the flange was mounted on a wood plate fixed to two tables. **Figure 2.4-1** shows the assembly mounted on the plate with the motor axis, bearing and coupling. **Figure 2.4-2** shows the coil mounted on the bottom. The superconductor supporting structure is inside the coil. Finally, **Figure 2.4-3** shows the motor mounted on top of the assembly.



Figure 2.4-1 Motor Axis, Bearing and Coupling Assembly

- be used for any purposes other than those for which it was supplied
- be copied or reproduced in whole or in detail without the prior written consent of ARCS
- be disclosed to any third party without the prior written consent of ARCS.

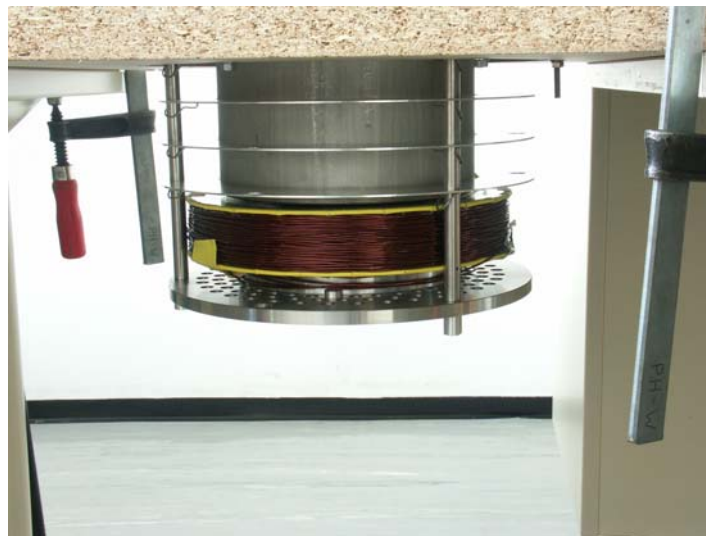


Figure 2.4-2 Coil Assembly



Figure 2.4-3 Motor Assembly

- be used for any purposes other than those for which it was supplied
- be copied or reproduced in whole or in detail without the prior written consent of ARCS
- be disclosed to any third party without the prior written consent of ARCS.

This assembly was tested with engine speeds up to 6500 rpm (minimum requirement 3000 rpm) and accelerations up to 1300 s^{-2} (minimum requirement 200 s^{-2}). No vibrations or abnormal facility behavior was noticed although the apparatus worked at more than twice its minimum requirements. Therefore, it was concluded to mount the facility on the cryostat.

In addition to the electric motor, a compressed air motor was also purchased and tested with the facility in order to exclude any electromagnetic interference of the engine with the measurement. The engine chosen was a Düsterloh PMW 400 Z24 ML/MR. This engine can reach 4000 RPM with a pressure of 10 bar. It is manually controlled and the actual speed is measured using a custom-built optical encoder.

2.5 Superconductor Support and Axis

After the first tests with the BSCCO superconductor, the ceramic broke into pieces as it could not withstand the applied accelerations. Therefore, a new superconductor was purchased and glued into the support structure using STYCAST epoxy (see **Figure 2.5-1**). On the top of the axis, a standard bearing was mounted with a heater to maintain 25°C during operation. On the bottom of the axis, a low-temperature KOYO bearing was initially mounted according to the original design. During testing it was realized that the high speeds more or less immediately damaged the KOYO bearing. It turned out that the best solution was to use a standard bearing with the highest possible gap, remove any lubricant, and put carbon powder inside as a solid lubricant. This bearing survived all later tests.



Figure 2.5-1 Superconductor Support (Left) and Upper Bearing (Right)

In order to obtain a reliable temperature measurement, a silicon diode (DT-670B-SD) from Lakeshore was installed on the superconductor support structure. A miniature collector ring (MD6038 and MD6043 from LTN Precision Products) on top of the axis enabled the correct readout even during high speed rotation (see **Figure 2.5-2**). The temperature stayed within 0.1K at speeds up to 6500 RPM.

- be used for any purposes other than those for which it was supplied
- be copied or reproduced in whole or in detail without the prior written consent of ARCS
- be disclosed to any third party without the prior written consent of ARCS.

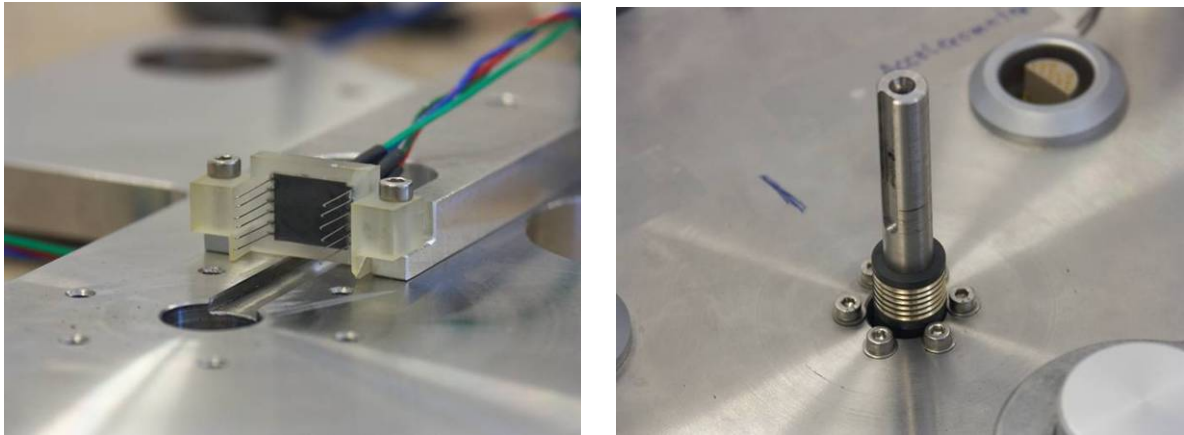


Figure 2.5-2 Miniature Collector Ring for Superconductor Temperature Read-Out

2.6 Cryostat Assembly

The experiment was then mounted on the cryostat (see **Figure 2.6-1**). In order to reduce possible vibrations from the motor, the cryostat was then put inside a box filled with sand. This increases the base weight by 1500 kg (see **Figure 2.6-2**).



Figure 2.6-1 Cryostat Assembly

- be used for any purposes other than those for which it was supplied
- be copied or reproduced in whole or in detail without the prior written consent of ARCS
- be disclosed to any third party without the prior written consent of ARCS.

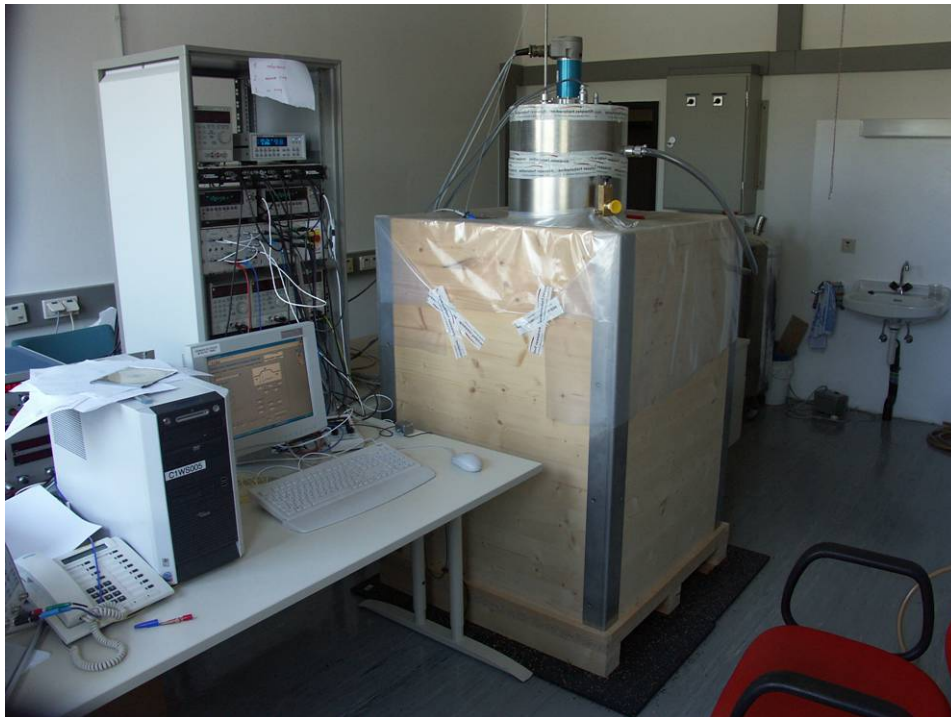


Figure 2.6-2 Cryostat Assembly in Sand Box

Because the noise level in this setup was too high (mN level), the original damping system had to be replaced. Tests with accelerometers on the floor during operation of the machine showed that the building very effectively damps the oscillations from the rotating superconducting ring. Therefore, a new design was made where the sensor chamber is directly mounted to a fixed structure made out of steel that is fixed to the floor and roof of the building (see **Figure 2.6-3**). Only flexible tubes along the three shafts (necessary to seal the cryostat) and electric wires from the sensor chamber to the flange have direct contact between the sensor chamber and the cryostat. This system proved to enable low noise operation during high rotation. The final configuration is shown with the air and electric motor in **Figure 2.6-4**.

- be used for any purposes other than those for which it was supplied
- be copied or reproduced in whole or in detail without the prior written consent of ARCS
- be disclosed to any third party without the prior written consent of ARCS.

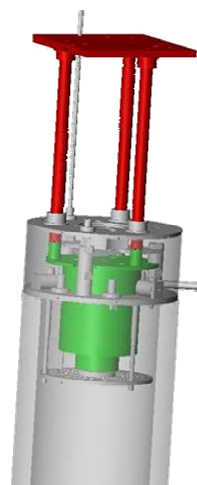
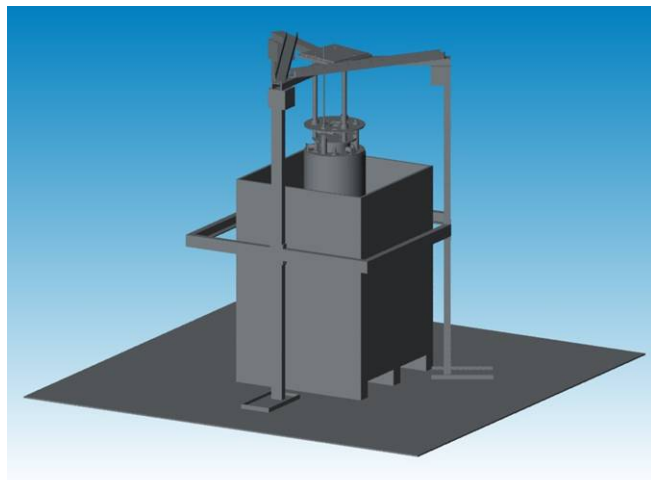


Figure 2.6-3 Fixed Structure around Cryostat holding the Sensor Chamber (Green) by three solid shafts (Red) - Shown in Detail on the Right



Figure 2.6-4 Final Configuration with Air Motor (Left) and Electric Motor (Right)

- be used for any purposes other than those for which it was supplied
- be copied or reproduced in whole or in detail without the prior written consent of ARCS
- be disclosed to any third party without the prior written consent of ARCS.

2.7 Electrical Setup

Figure 2.7-1 shows the setup of all sensors and electrical measurement devices. The accelerometers/magnetometers, the heaters as well as the low temperature monitor are controlled via the GPIB bus. The electric motor, the coil, the PT-100 temperature sensors and the optical encoder are controlled using a National Instruments DAQ board. The PC runs a LabView software to control and monitor all parameters.

Before the Keithley Nanovoltmeters, the sensors can be connected to an electronic box that subtracts two signal lines from each other (e.g. In-Ring Tangential – Reference Tangential Position). The differential signal can then be connected to the Keithley. Also a mixture of single and differential signals can be connected.

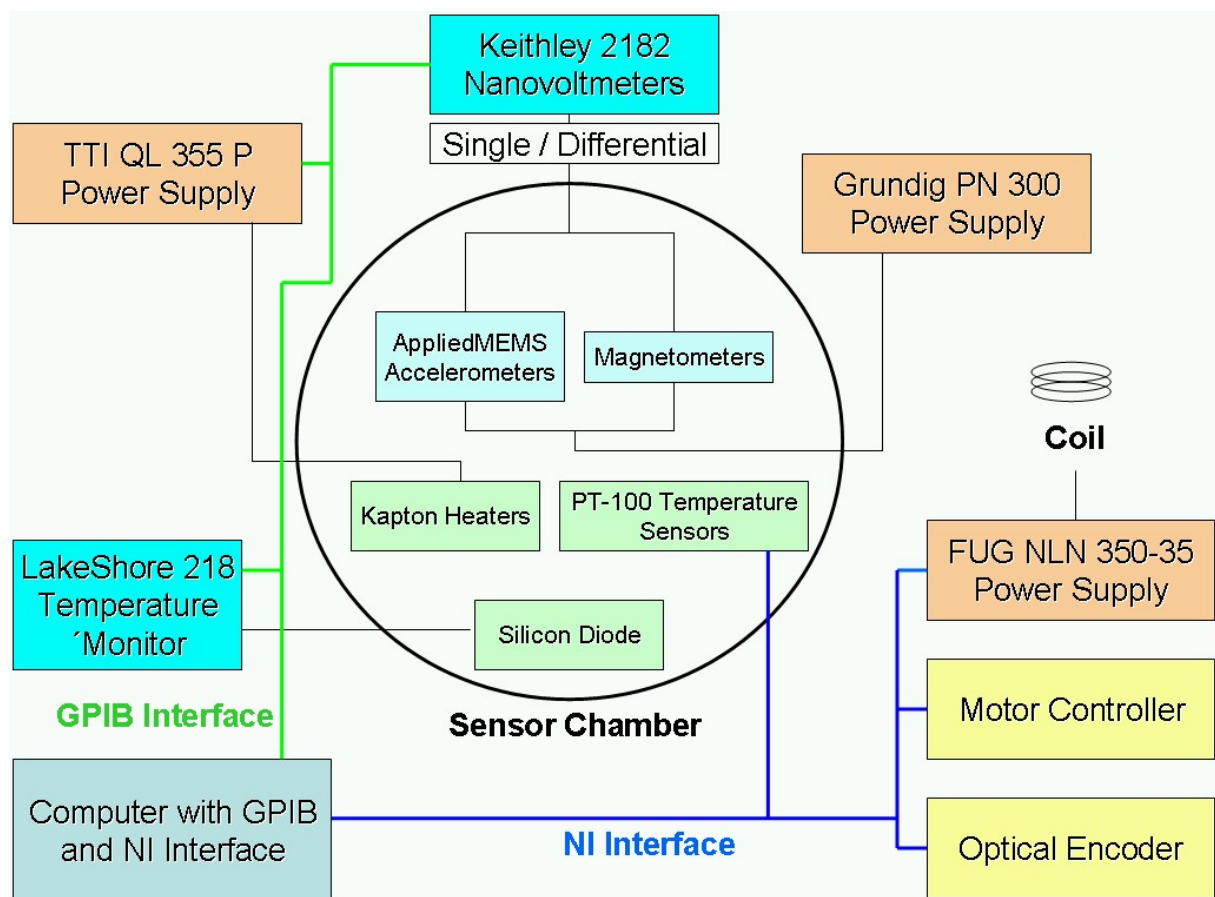


Figure 2.7-1 Electrical Setup

- be used for any purposes other than those for which it was supplied
- be copied or reproduced in whole or in detail without the prior written consent of ARCS
- be disclosed to any third party without the prior written consent of ARCS.

2.8 Data Acquisition and Control Program

In order to read out all sensors, command the motor and regulate the temperature at the bearing and accelerometers, a custom program was written in LabVIEW 7.1.

The following input parameters are processed by the program:

- 2x Keithley Nanovoltmeter, translated into gravitational acceleration ($2V = 1\text{ g}$) or magnetic field; digital integration and moving filter settings can be commanded via GPIB interface
- PT 100 thermocouple at all accelerometer positions (1x reference, 1x inner ring, 1x above ring); 2 wire method
- PT 100 thermocouple at upper bearing – 2 wire method
- Temperature superconductor (silicon diode connected via LakeShore 218 temperature monitor) [K]
- Field coil power supply
- Electric motor angular velocity and torque
- Optical encoder velocity

The following output parameters are processed by the program:

- Regulate heating power for each accelerometer and upper bearing position (according to temperature measured at each position)
- Drive field coil power supply
- Drive motor encoder

The program is subdivided into 6 main screens:

- Experiment: To set the profile shapes and speeds and to start the measurement (see **Figure 2.8-1**).
- Measurement: To define which accelerometer/magnetometer positions are connected to the Keithley Nanovoltmeters and which filter settings shall be used (see **Figure 2.8-2 Left**).
- Coil: To define the magnetic field (constant or profiles) that shall be produced from the coil.
- Environment: To set the temperature to which the accelerometers/upper bearing shall be controlled (see **Figure 2.8-2 Right**).
- Channels: Setup for GPIB and NI controller.
- Settings: Individual calibration constants for accelerometers and magnetometers.

Before each measurement, the Keithleys are calibrated and a 5 seconds test run is done to ensure that all data channels are synchronized. By using a frequency generator for one data channel it was verified that all channels are recorded with a maximum time shift of one timestep between them.

- be used for any purposes other than those for which it was supplied
- be copied or reproduced in whole or in detail without the prior written consent of ARCS
- be disclosed to any third party without the prior written consent of ARCS.

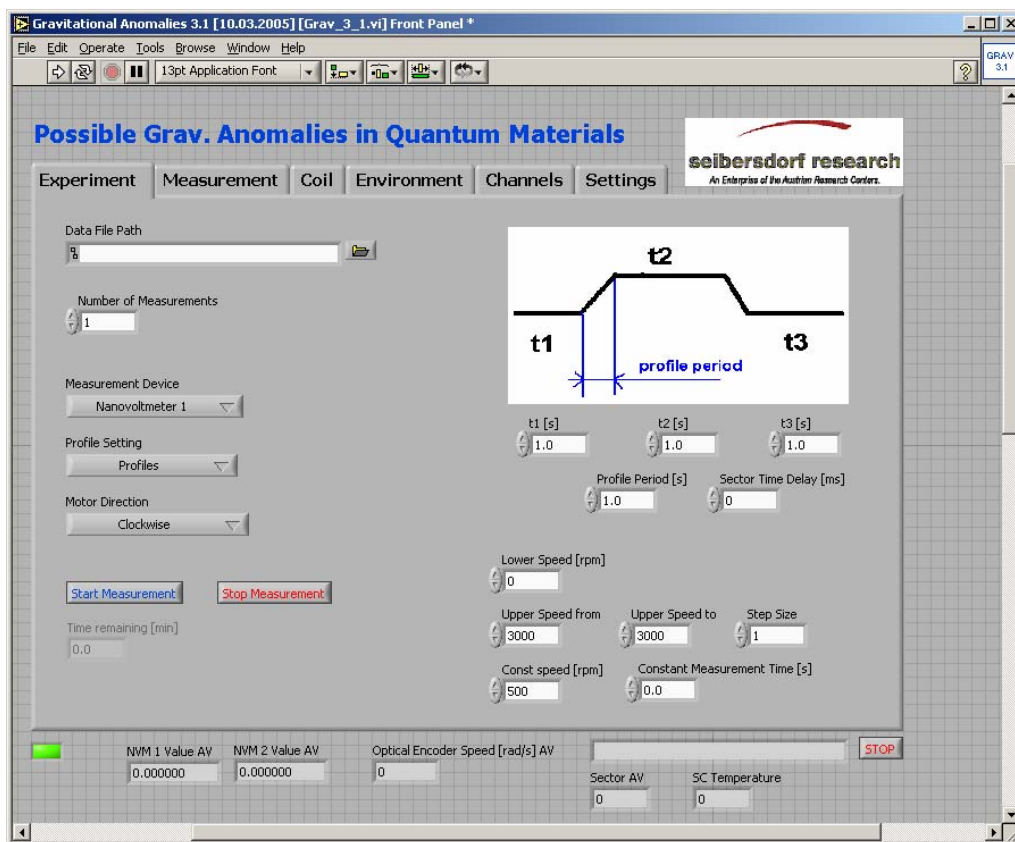


Figure 2.8-1 Experiment Screen

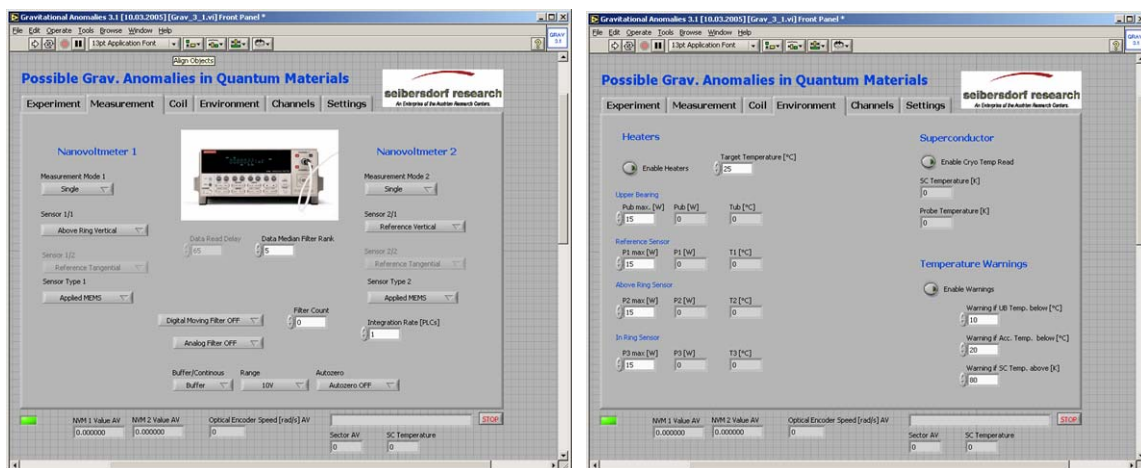


Figure 2.8-2 Measurement and Environment Screen

- be used for any purposes other than those for which it was supplied
- be copied or reproduced in whole or in detail without the prior written consent of ARCS
- be disclosed to any third party without the prior written consent of ARCS.

The speed and acceleration profile can be controlled as shown in **Figure 2.8-3** by subdividing it into 5 sectors. Each sector speed and time interval can be set individually. For comparison, the raw data from the optical encoder is compared with the filtered (Digital Moving Filter over 5 data points) and commanded speed/acceleration. The noise of the raw data in the acceleration profile is due to the numerical differentiation. By comparison between commanded and measured speeds, the maximum deviation was < 5% at speeds up to 1000 RPM and < 1% at full speed.

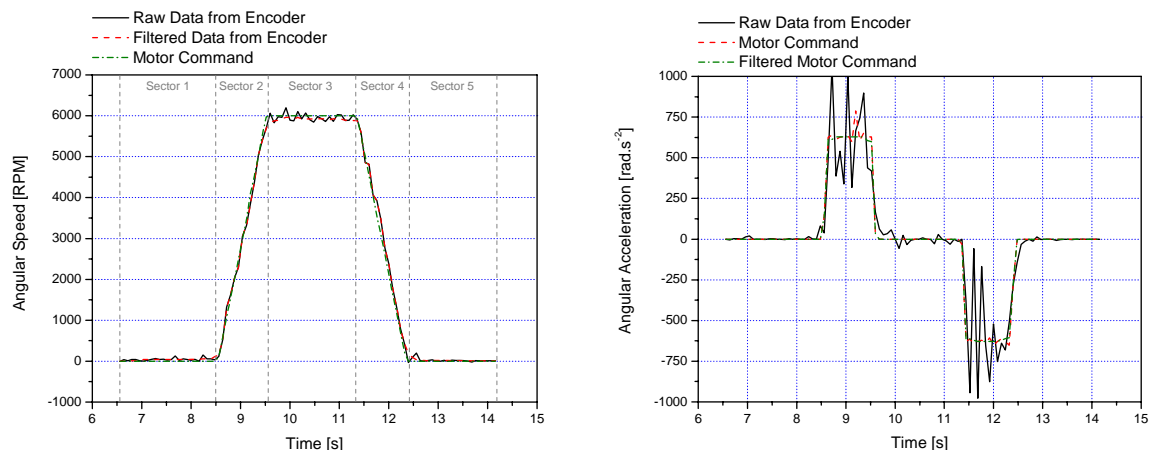


Figure 2.8-3 Speed and Acceleration Profile

2.9 Data Analysis Program

A second LabView program was also written (see **Figure 2.9-1**) in order to process the raw data and to do a statistical evaluation. The program can evaluate the coupling factors by performing a linear fit between the gravitational field measured and the applied speed, speed² and acceleration to the superconductor during each profile. As we always measure a number of profiles, the program can evaluate the coupling factors, the mean values and standard deviation, as well as the correlation factors. Other features include

- Selection of temperature, speed and acceleration range
- Selection of sectors (e.g. only sector 2 and 4)
- Subtraction of friction forces in the measurement (friction if proportional to the angular speed)
- Software subtraction of sensor positions

- be used for any purposes other than those for which it was supplied
- be copied or reproduced in whole or in detail without the prior written consent of ARCS
- be disclosed to any third party without the prior written consent of ARCS.

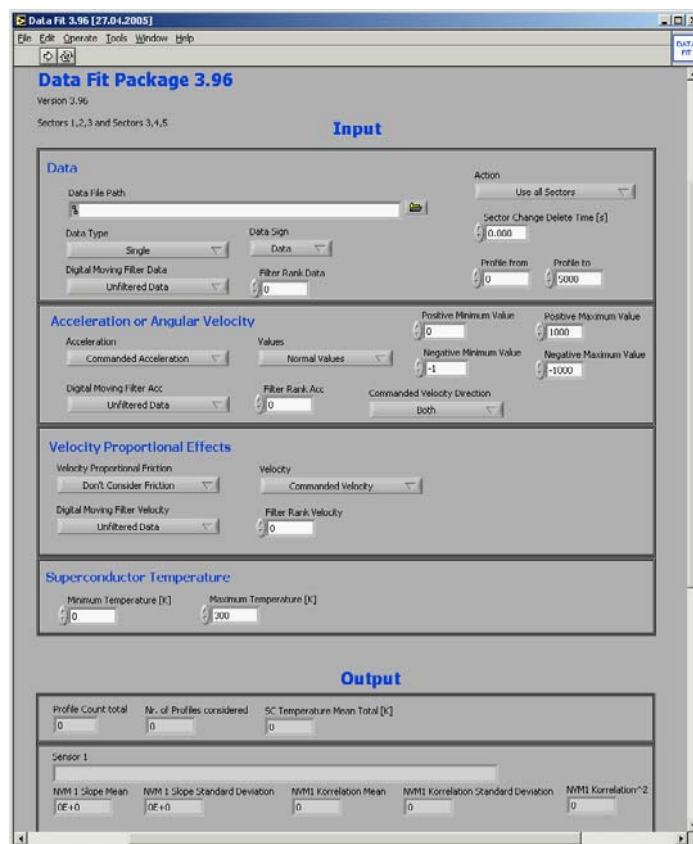


Figure 2.9-1 Data Analysis Program

- be used for any purposes other than those for which it was supplied
- be copied or reproduced in whole or in detail without the prior written consent of ARCS
- be disclosed to any third party without the prior written consent of ARCS.

3 EXPERIMENTAL RESULTS

3.1 Introduction

The following chapters summarize the experimental work carried out with the facility in its highest resolution configuration. In addition to a BSCCO superconductor, also experiments with YBCO were performed both at room temperature and at 77 K (using liquid nitrogen). For calibration purposes, also a Niobium ring was tested at 77 K (not superconductive at this temperature) in order to check for effects that could be caused by the liquid nitrogen itself.

In all tests, the following profile was commanded to the electric motor:

- 1 second at zero speed
- 1 second accelerating to 6500 RPM in clockwise direction
- 1 second remaining at full speed
- 1 second de-accelerating to zero speed
- Do the same profile but this time in counter-clockwise direction

This was repeated 5-10 times. Each profile was then processed using the DataFit Software and statistics were done to evaluate the coupling factors for all sensor positions inside and above the ring (using differential measurement technique). In addition to the angular acceleration coupling factor, also a possible coupling factor for the angular speed and angular speed² (centrifugal acceleration) was evaluated.

In order to perform the tests at 77 K, the cryostat was filled with liquid nitrogen to about 1 cm below the upper edge of the superconductor ring. After each profile, nitrogen evaporated and the liquid nitrogen level in the dewar was reduced. After about 70 profiles, the liquid was below the ring and the superconductor heated up.

- be used for any purposes other than those for which it was supplied
- be copied or reproduced in whole or in detail without the prior written consent of ARCS
- be disclosed to any third party without the prior written consent of ARCS.

3.2 Sensor External Influence

In order to reach the highest accuracy, the motor speed and acceleration was set to their limits. In all final runs, a top speed of 6500 RPM accelerated and de-accelerated in 1 s could be achieved. The first months of testing were devoted to run the machine with the BSCCO superconductor at 77K using liquid nitrogen and at near room temperature, analyze the signals, and to find if the motor or the setup are inducing false signals. The following three error sources were identified and consequently removed for the final runs:

1. The most severe problem was that after some time (ranging from minutes to hours, depending on the bearing) the bottom bearing started to get problems and created noise. This noise was proportional to ω^2 – the higher the force on the bearing, the higher the noise. This acoustic noise caused the cryostat and the fixed cage structure to vibrate. Due to the vertical mounting of the sensor chamber, the sensors could then also vibrate in the radial direction. This in turn was interpreted by the sensor electronics as a shift in the signal of the radial sensor (see **Figure 3.2-1**). This shift was several hundred μg (up to milli-g when the bearing was nearly dead), which then also transmitted to other sensor positions as they are not perfectly aligned to the central axis. The problem was circumvented by using a new bearing for every new test. As soon as the false signal appeared, the test had to be stopped and the bearing had to be exchanged. A similar problem occurred with the air motor as already the motor's noise was very large.

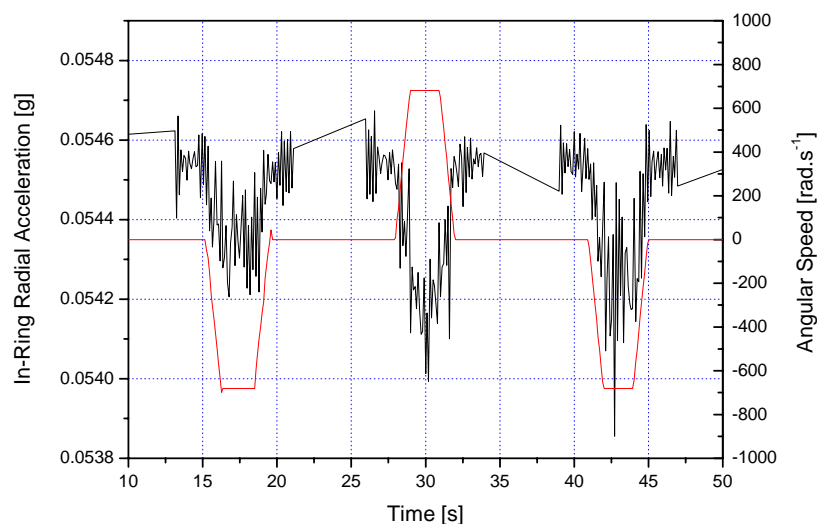


Figure 3.2-1 False Radial Measurement due to Bearing Noise

2. The second important point was that ice formation could occur after some hours of liquid nitrogen cooling which then in turn could cause vibrations on the sensor chamber (the gap between axis and sensor chamber is only 1 mm!). This caused wrong signals in the radial direction because there was now a direct transfer of force from the rotation of the axis (a force again in the radial direction proportional to ω^2 appeared due to the centrifugal force on the axis, see **Figure 3.2-2**).

The best results were always obtained shortly after assembly and cooling down. It was found out that up to 5 hours after initial LN₂ filling, no false signals appeared.

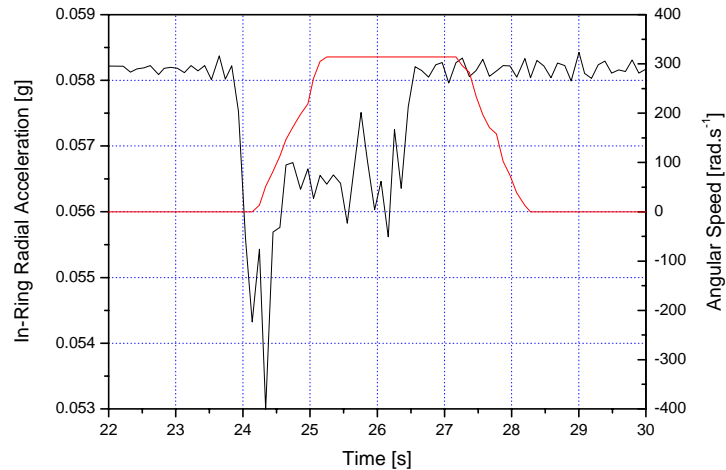


Figure 3.2-2 False Radial Measurement due to Ice Formation on Motor Axis

3. The third important point was to ground all cables that are not used and are coming from the sensor chamber. Because we had only two Keithley Nanovoltmeters, two sensors could be measured and the others signal outputs were initially floating. This caused a measurable influence of the motor magnetic field which was different if the BSCCO was superconductive or not (it acts like a magnetic mirror when it is superconductive). The motor on/off as well and the difference when the BSCCO was superconductive or not can be seen in **Figure 3.2-3**. After all cables were properly grounded, no influence could be seen any more.

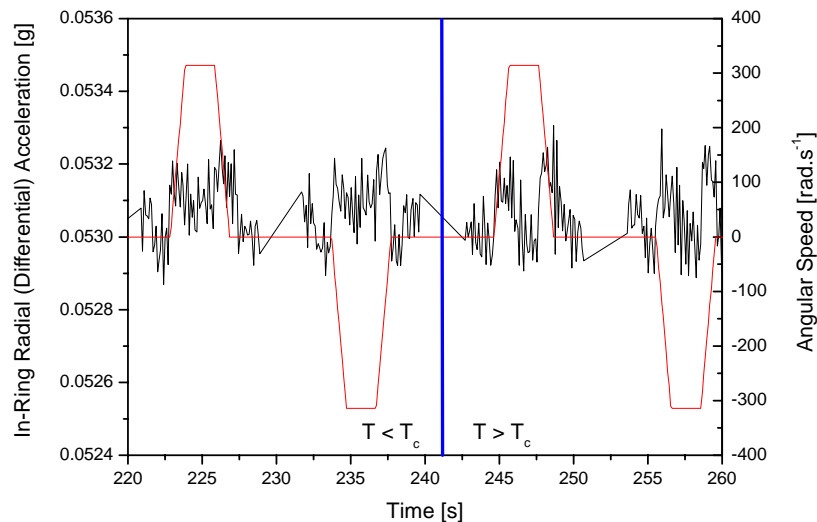


Figure 3.2-3 False Radial Measurement due to Cable Induction

Using the coil, the influence of a strong magnetic field on the accelerometers was evaluated. The test was done with the BSCCO ring at 117 K (normal conductive) and 77 K (superconductive). An oscillating magnetic field with an amplitude of 20 mT was applied and the sensor responses were evaluated (see **Figure 3.2-4** to **Figure 3.2-9**). **Table 3** summarizes the measured offsets, which were linear with the applied magnetic field, when the BSCCO is superconductive, it acts as a magnetic shield and reduces the influence on the sensors.

As the maximum magnetic field from the electric motor was measured to be about 50 μT , the maximum offset for the real runs should be therefore less than 0.025 μg , which is far below the measurement threshold of the sensors (about 1 μg). Therefore, influence of magnetic fields on the results can be neglected.

Offset [μg]		
Sensor Position	Normal Conductive	Superconductive
In-Ring Radial	5	< 1
In-Ring Tangential	10	5
In-Ring Vertical	10	2.5
Above-Ring Radial	<1	< 1
Above-Ring Tangential	5	5
Above-Ring Vertical	5	10

Table 3 Magnetic Field Influence (20 mT) on Sensors

- be used for any purposes other than those for which it was supplied
- be copied or reproduced in whole or in detail without the prior written consent of ARCS
- be disclosed to any third party without the prior written consent of ARCS.

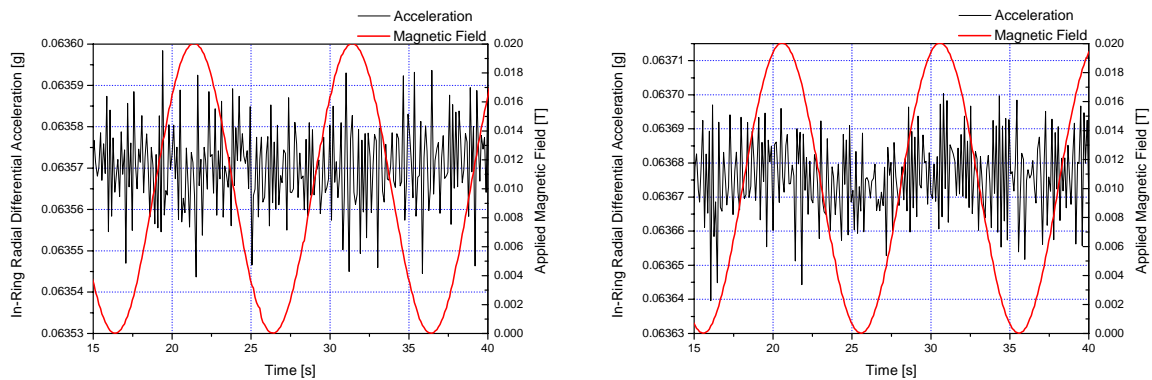


Figure 3.2-4 Influence of Magnetic Field on In-Ring Radial Sensor with BSCCO at 77K and 270K

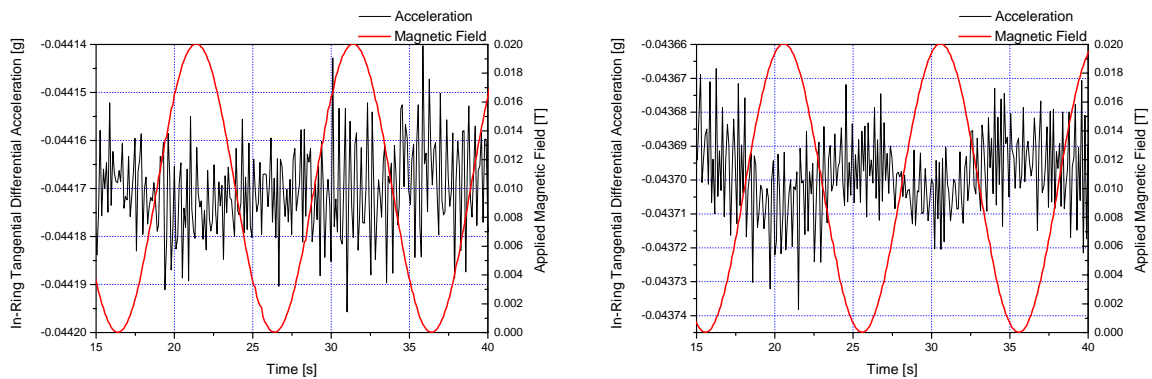


Figure 3.2-5 Influence of Magnetic Field on In-Ring Tangential Sensor with BSCCO at 77K and 270K

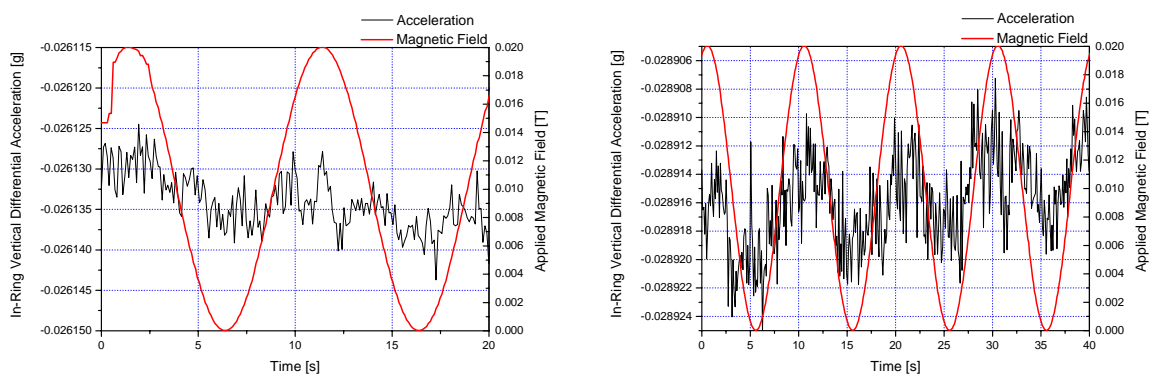


Figure 3.2-6 Influence of Magnetic Field on In-Ring Vertical Sensor with BSCCO at 77K and 270K

- be used for any purposes other than those for which it was supplied
- be copied or reproduced in whole or in detail without the prior written consent of ARCS
- be disclosed to any third party without the prior written consent of ARCS.

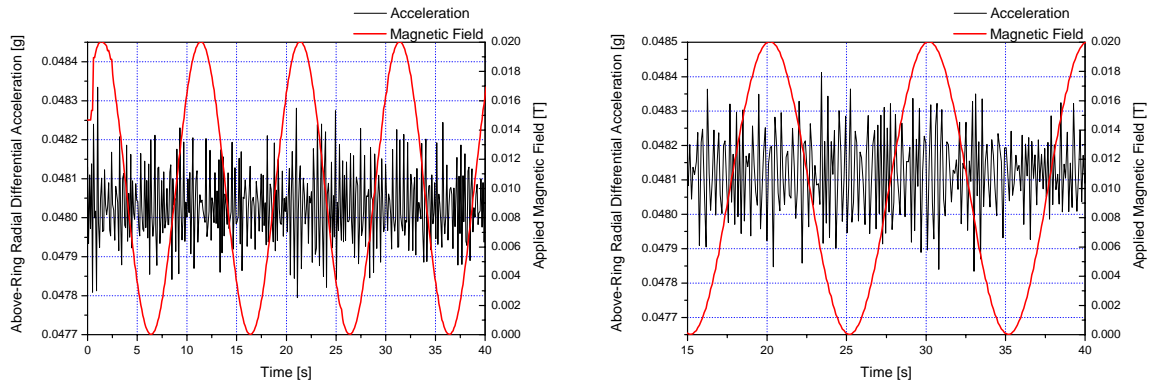


Figure 3.2-7 Influence of Magnetic Field on Above-Ring Radial Sensor with BSCCO at 77K and 270K

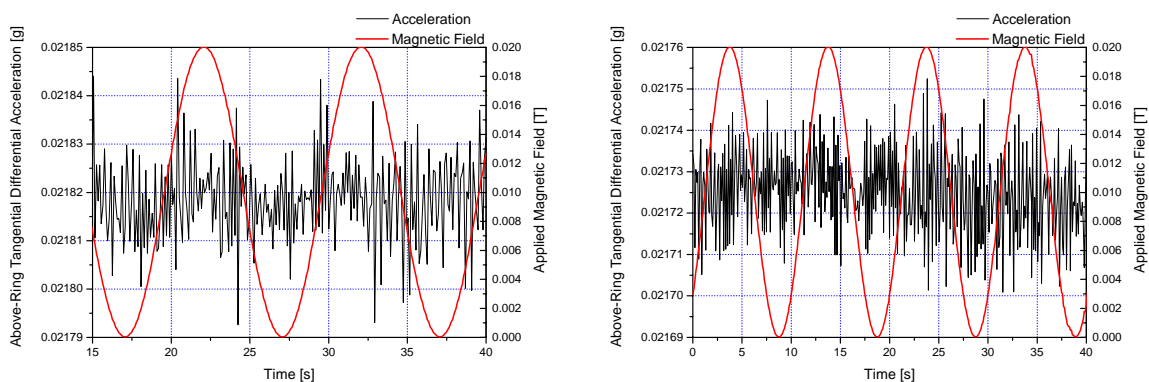


Figure 3.2-8 Influence of Magnetic Field on Above-Ring Tangential Sensor with BSCCO at 77K and 270K

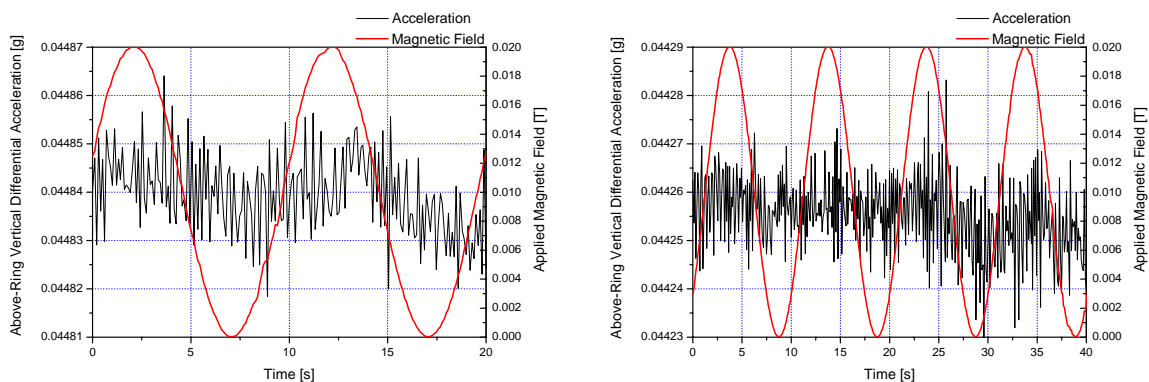


Figure 3.2-9 Influence of Magnetic Field on Above-Ring Vertical Sensor with BSCCO at 77K and 270K

- be used for any purposes other than those for which it was supplied
- be copied or reproduced in whole or in detail without the prior written consent of ARCS
- be disclosed to any third party without the prior written consent of ARCS.

3.3 Facility Calibration with Niobium Dummy

Figure 3.4-2 to Figure 3.4-7 show a comparison between all sensor positions at 77K and 270K during acceleration to maximum speed in both directions. The sensor sigma at our measurement rate of 10 Hz was about 15 μg as it can be seen in the raw data plots.

The coupling factors (linear fit of raw data per profile) between gravitational field and applied acceleration, velocity and velocity² for Niobium at 77K and 270K is shown in **Tables 4-6**.

No significant difference between 77K and 270K can be seen, therefore, the results of the facility are not influenced by the liquid nitrogen (evaporation during rotating, different acoustic noise of bearing when in or out of liquid nitrogen, etc.).

The angular acceleration coupling factor sigmas for all sensors are in the low 10^{-8} range, except for the vertical direction, which is in the low 10^{-9} range (due to the construction of the fixed cage, the vertical direction has the highest damping factor).

Comparing with the predicted coupling factors in **Table 2**, that is the right range to detect the anomaly based on Tate's measurement (for which the facility was designed in Phase I), but the sigmas are too high by at least 1-2 orders of magnitude to detect induced gravitational fields for high-temperature superconductors (due to the much lower Cooper-pair density).

- be used for any purposes other than those for which it was supplied
- be copied or reproduced in whole or in detail without the prior written consent of ARCS
- be disclosed to any third party without the prior written consent of ARCS.

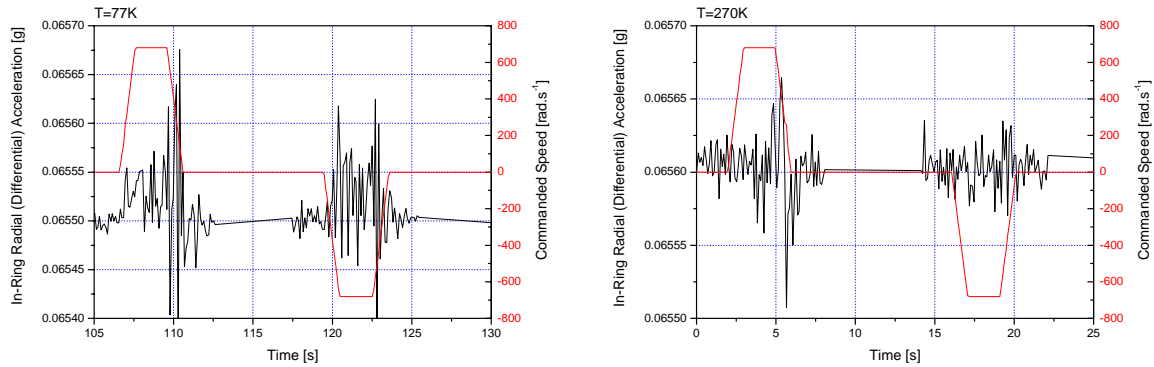


Figure 3.3-1 Niobium In-Ring Radial Differential Sensor Comparison at 77K and 270K

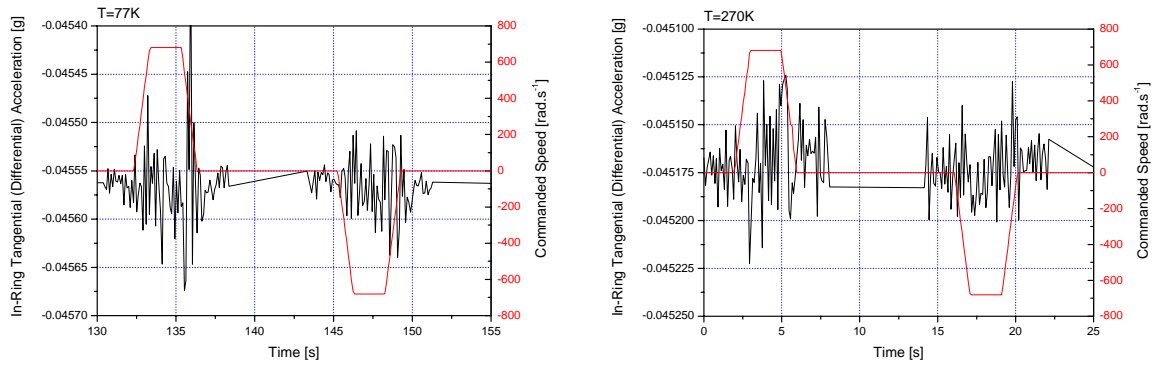


Figure 3.3-2 Niobium In-Ring Tangential Differential Sensor Comparison at 77K and 270K

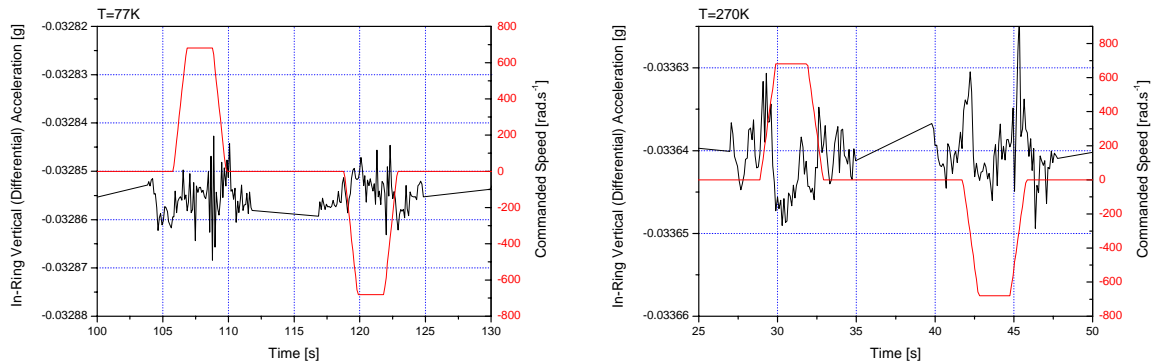


Figure 3.3-3 Niobium In-Ring Vertical Differential Sensor Comparison at 77K and 270K

- be used for any purposes other than those for which it was supplied
- be copied or reproduced in whole or in detail without the prior written consent of ARCS
- be disclosed to any third party without the prior written consent of ARCS.

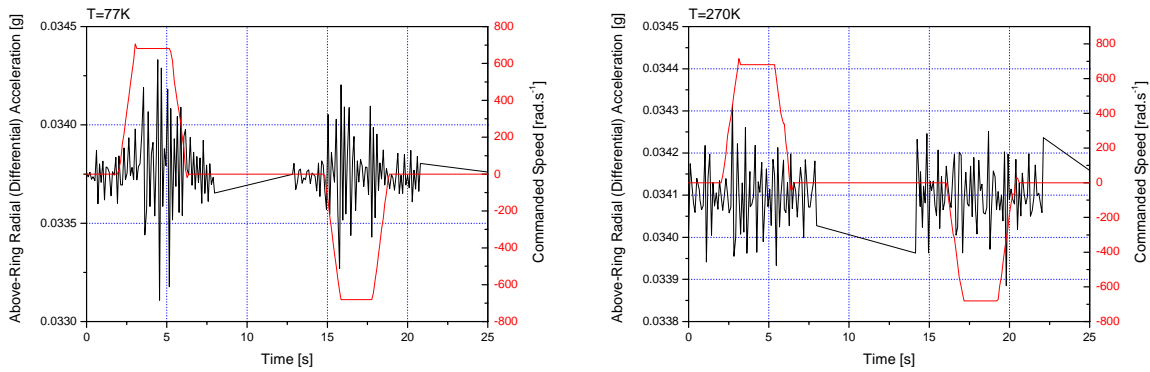


Figure 3.3-4 Niobium Above-Ring Radial Differential Sensor Comparison at 77K and 270K

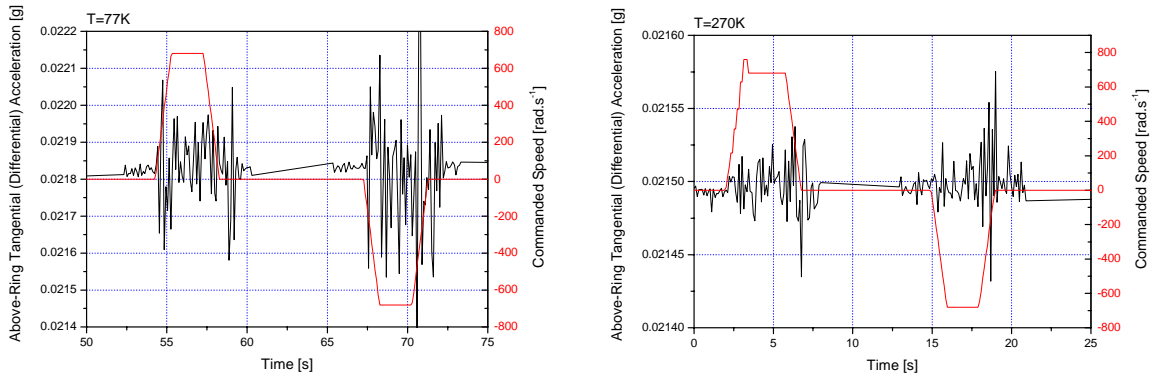


Figure 3.3-5 Niobium Above-Ring Tangential Differential Sensor Comparison at 77K and 270K

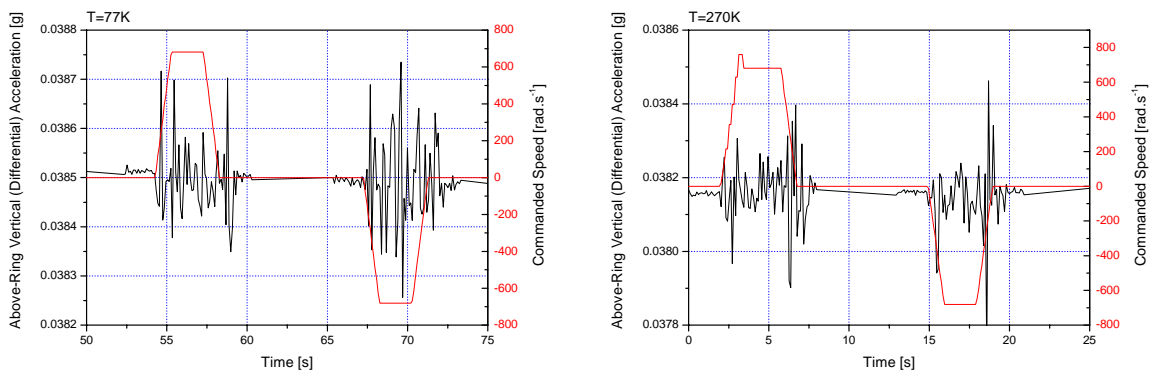


Figure 3.3-6 Niobium Above-Ring Vertical Differential Sensor Comparison at 77K and 270K

- be used for any purposes other than those for which it was supplied
- be copied or reproduced in whole or in detail without the prior written consent of ARCS
- be disclosed to any third party without the prior written consent of ARCS.

	77K				270K			
	Acceleration Coupling Factor		Correlation Factor		Acceleration Coupling Factor		Correlation Factor	
Position	Mean	Sigma	Mean	Sigma	Mean	Sigma	Mean	Sigma
In-Ring Radial	-6.21E-09	1.76E-08	-0.04	0.13	-1.80E-09	1.18E-08	-0.02	0.15
In-Ring Tangential	-1.29E-09	2.05E-08	-0.01	0.17	-2.53E-10	1.11E-08	0.00	0.15
In-Ring Vertical	-2.48E-10	1.42E-09	-0.02	0.13	9.85E-10	1.62E-09	0.08	0.14
Above-Ring Radial	-2.87E-08	3.36E-08	-0.04	0.05	1.15E-09	1.30E-08	0.00	0.04
Above-Ring Tangential	-1.01E-08	4.97E-08	0.00	0.10	-3.06E-10	8.88E-09	0.00	0.14
Above-Ring Vertical	5.42E-09	1.80E-08	0.03	0.08	-3.37E-09	4.62E-08	0.00	0.16

Table 4 Niobium Acceleration Coupling at 77K and 270K (Over 20 Profiles)

	77K				270K			
	Velocity Coupling Factor		Correlation Factor		Velocity Coupling Factor		Correlation Factor	
Position	Mean	Sigma	Mean	Sigma	Mean	Sigma	Mean	Sigma
In-Ring Radial	-9.55E-10	4.30E-09	-0.09	0.27	-1.65E-11	6.67E-09	0.00	0.07
In-Ring Tangential	-1.66E-08	7.02E-08	0.00	0.08	-9.85E-10	7.87E-09	0.00	0.11
In-Ring Vertical	-1.72E-09	3.13E-09	-0.15	0.26	-1.13E-09	5.44E-09	-0.05	0.42
Above-Ring Radial	-1.41E-08	6.61E-08	0.00	0.095	4.79E-11	7.58E-09	0.00	0.02
Above-Ring Tangential	8.96E-09	4.13E-08	0.02	0.11	-2.02E-09	7.69E-09	-0.04	0.11
Above-Ring Vertical	-4.92E-09	2.37E-08	0.00	0.07	-2.59E-09	1.84E-08	-0.01	0.08

Table 5 Niobium Velocity Coupling at 77K and 270K (Over 20 Profiles)

- be used for any purposes other than those for which it was supplied
- be copied or reproduced in whole or in detail without the prior written consent of ARCS
- be disclosed to any third party without the prior written consent of ARCS.

	77K				270K			
	Velocity ² Coupling Factor		Correlation Factor		Velocity ² Coupling Factor		Correlation Factor	
Position	Mean	Sigma	Mean	Sigma	Mean	Sigma	Mean	Sigma
In-Ring Radial	3.79E-12	4.93E-12	0.18	0.20	-2.73E-12	8.83E-12	-0.02	0.06
In-Ring Tangential	8.39E-11	4.00E-11	0.06	0.03	-8.63E-12	8.12E-12	-0.08	0.07
In-Ring Vertical	2.65E-12	4.09E-12	0.15	0.23	-8.55E-12	2.85E-12	-0.44	0.15
Above-Ring Radial	7.30E-11	4.70E-11	0.06	0.03	-3.37E-12	1.05E-11	0.00	0.01
Above-Ring Tangential	2.82E-11	5.22E-11	0.06	0.09	4.18E-12	9.11E-12	0.05	0.08
Above-Ring Vertical	1.16E-11	3.37E-11	0.02	0.07	-7.40E-12	2.70E-11	-0.01	0.08

Table 6 Niobium Velocity² Coupling at 77K and 270K (Over 20 Profiles)

- be used for any purposes other than those for which it was supplied
- be copied or reproduced in whole or in detail without the prior written consent of ARCS
- be disclosed to any third party without the prior written consent of ARCS.

3.4 BSCCO Coupling Factor Evaluation

In order to evaluate the critical temperature of our BSCCO ring (manufactured by NEXANS Superconductors, dimension 150x138x15 mm), a magnetic field was trapped during cooling down using the coil. Then the coil was switched off – and the magnetic field remained because BSCCO is a Type-II superconductor. During warming up, the magnetic field suddenly dropped to zero – exactly when the superconductor turned normal conductive. During several tests the critical temperature in our setup was therefore evaluated to be around 88.3 K (see **Figure 3.4-1**). This value is about 2 K higher than BSCCO critical temperatures in the literature (for phase 2122) which is probably due to our temperature measurement location of the silicon diode and the collector ring setup as well as the STYCAST fixing of the ring into the superconductor holder.

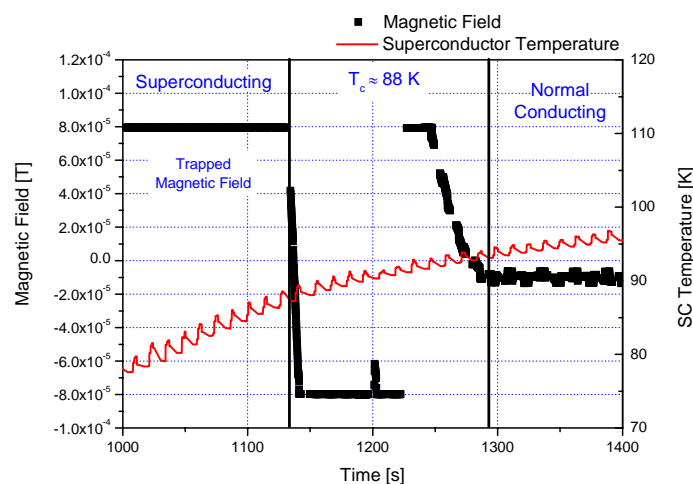


Figure 3.4-1 BSCCO Critical Temperature Measurement with Trapped Magnetic Field

Figure 3.4-2 to **Figure 3.4-7** show a comparison between all sensor positions at 77K and 270K during acceleration to maximum speed in both directions. The sensor sigma at our measurement rate of 10 Hz was about 15 μ g as it can be seen in the raw data plots.

The coupling factors (linear fit of raw data per profile) between gravitational field and applied acceleration, velocity and velocity² for BSCCO at 77K and 270K are shown in **Tables 7-9**. The sigmas are a little bit smaller compared to the Niobium dummy tests, probably due to the smaller weight of the ring and therefore reduced forces on the bearing.

For the acceleration coupling factors, all mean values are below its sigma. Also, no significant difference can be seen between the superconductive and normal conductive case – within the resolution threshold. The sigmas must be interpreted as upper boundaries for possible gravitational interactions for BSCCO.

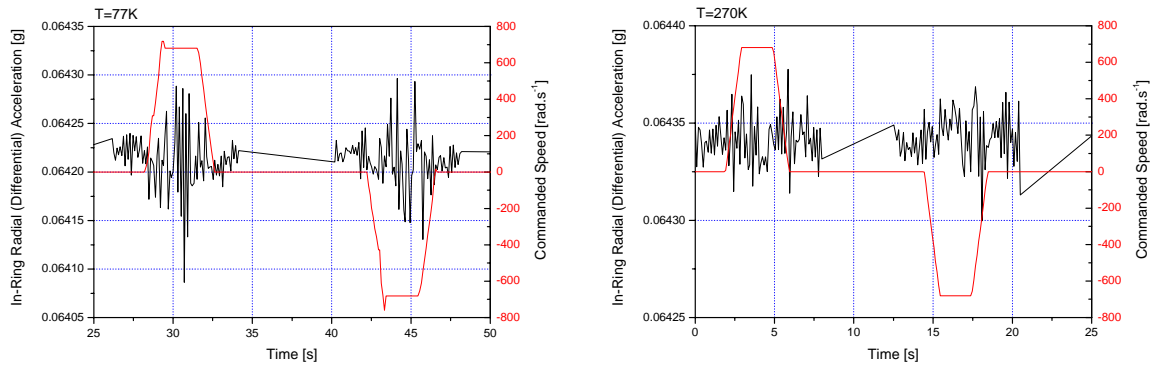


Figure 3.4-2 BSCCO In-Ring Radial Differential Sensor Comparison at 77K and 270K

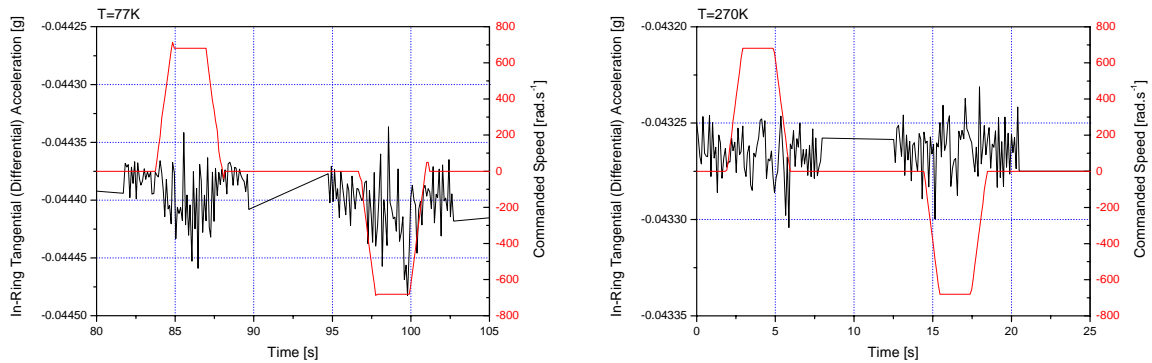


Figure 3.4-3 BSCCO In-Ring Tangential Differential Sensor Comparison at 77K and 270K

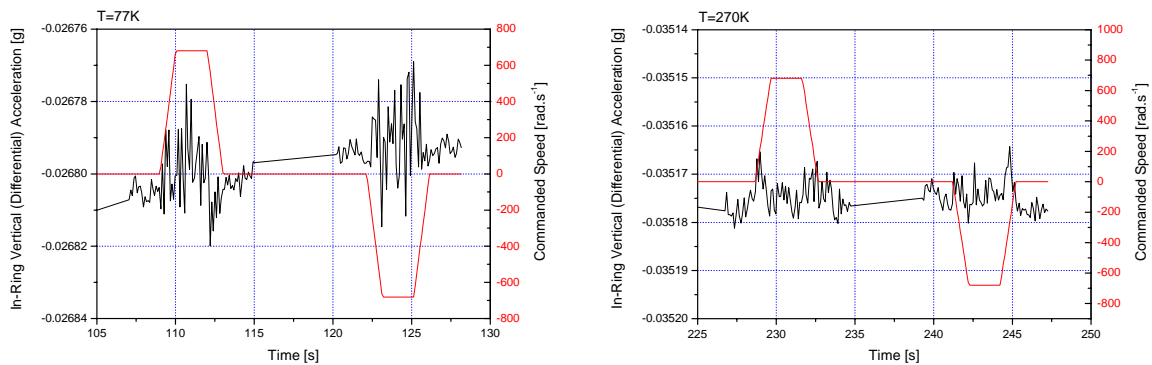


Figure 3.4-4 BSCCO In-Ring Vertical Differential Sensor Comparison at 77K and 270K

- be used for any purposes other than those for which it was supplied
- be copied or reproduced in whole or in detail without the prior written consent of ARCS
- be disclosed to any third party without the prior written consent of ARCS.

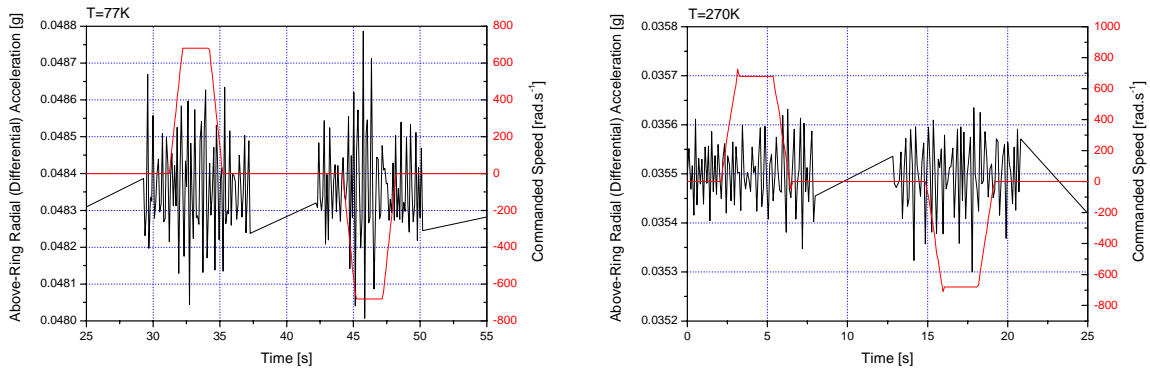


Figure 3.4-5 BSCCO Above-Ring Radial Differential Sensor Comparison at 77K and 270K

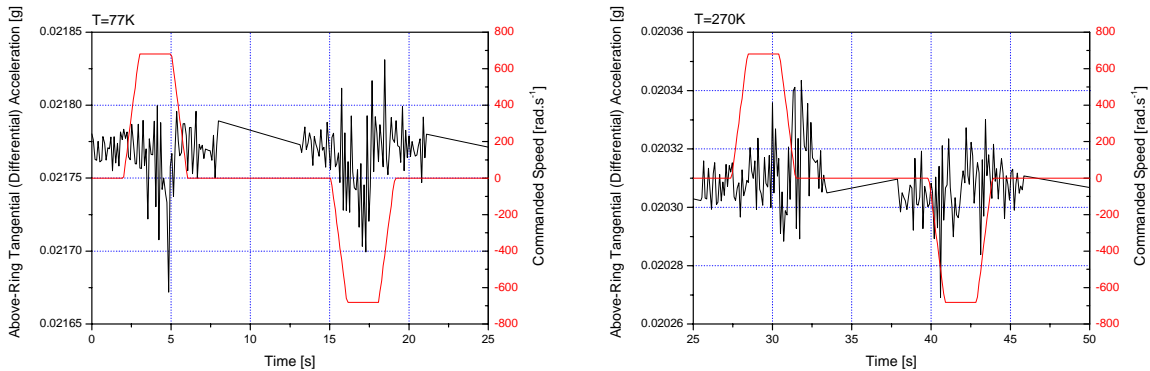


Figure 3.4-6 BSCCO Above-Ring Tangential Differential Sensor Comparison at 77K and 270K

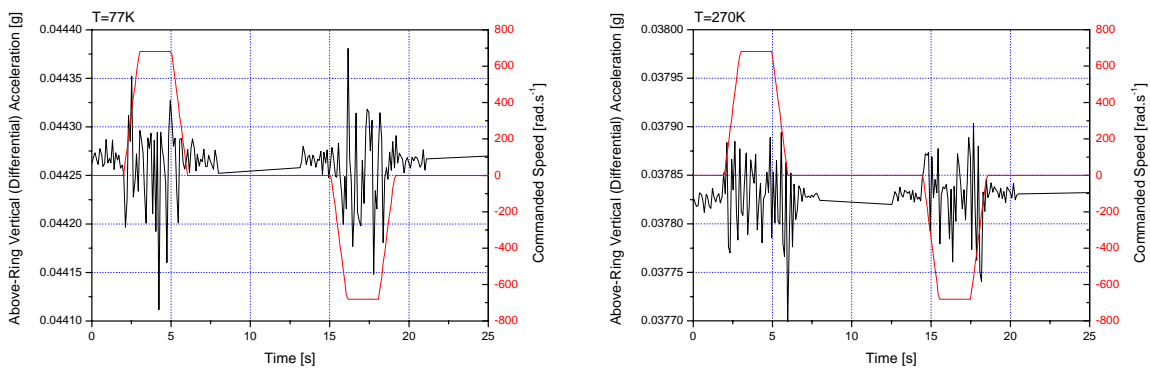


Figure 3.4-7 BSCCO Above-Ring Vertical Differential Sensor Comparison at 77K and 270K

- be used for any purposes other than those for which it was supplied
- be copied or reproduced in whole or in detail without the prior written consent of ARCS
- be disclosed to any third party without the prior written consent of ARCS.

	77K				270K			
	Acceleration Coupling Factor		Correlation Factor		Acceleration Coupling Factor		Correlation Factor	
Position	Mean	Sigma	Mean	Sigma	Mean	Sigma	Mean	Sigma
In-Ring Radial	-9.73E-10	8.45E-09	-0.01	0.11	-4.00E-09	5.34E-09	-0.09	0.12
In-Ring Tangential	-2.96E-09	4.84E-09	-0.04	0.06	-8.61E-10	5.51E-09	-0.02	0.14
In-Ring Vertical	4.52E-10	2.90E-09	0.02	0.13	7.59E-10	1.43E-09	0.07	0.14
Above-Ring Radial	2.06E-09	1.80E-08	0.00	0.04	1.14E-10	1.23E-08	0.01	0.04
Above-Ring Tangential	8.13E-10	7.01E-09	0.02	0.10	9.12E-09	8.09E-09	0.20	0.18
Above-Ring Vertical	9.23E-10	1.07E-08	0.00	0.12	2.87E-09	2.81E-08	0.02	0.24

Table 7 BSCCO Acceleration Coupling at 77K and 270K (Over 20 Profiles)

	77K				270K			
	Velocity Coupling Factor		Correlation Factor		Velocity Coupling Factor		Correlation Factor	
Position	Mean	Sigma	Mean	Sigma	Mean	Sigma	Mean	Sigma
In-Ring Radial	1.75E-09	1.20E-08	0.01	0.13	-3.27E-10	4.93E-09	-0.01	0.11
In-Ring Tangential	-7.07E-09	3.60E-08	-0.03	0.39	2.07E-09	4.88E-09	0.04	0.11
In-Ring Vertical	-3.40E-09	1.12E-08	-0.10	0.43	1.30E-10	2.49E-09	0.01	0.21
Above-Ring Radial	-2.13E-09	1.14E-08	-0.01	0.03	-1.28E-09	6.99E-09	0.00	0.03
Above-Ring Tangential	7.23E-10	3.55E-08	-0.03	0.44	1.56E-11	1.09E-08	-0.02	0.20
Above-Ring Vertical	-6.90E-09	2.08E-08	-0.07	0.19	-8.39E-10	1.31E-08	-0.01	0.11

Table 8 BSCCO Velocity Coupling at 77K and 270K (Over 20 Profiles)

- be used for any purposes other than those for which it was supplied
- be copied or reproduced in whole or in detail without the prior written consent of ARCS
- be disclosed to any third party without the prior written consent of ARCS.

	77K				270K			
	Velocity^2 Coupling Factor		Correlation Factor		Velocity^2 Coupling Factor		Correlation Factor	
Position	Mean	Sigma	Mean	Sigma	Mean	Sigma	Mean	Sigma
In-Ring Radial	-1.04E-11	1.22E-11	-0.08	0.08	4.98E-12	5.98E-12	0.07	0.09
In-Ring Tangential	-5.00E-11	1.35E-11	-0.37	0.10	2.06E-12	7.29E-12	0.03	0.11
In-Ring Vertical	1.34E-11	1.04E-11	0.35	0.25	6.47E-13	3.11E-12	0.04	0.18
Above-Ring Radial	3.62E-12	1.68E-11	0.01	0.03	5.69E-12	8.45E-12	0.02	0.02
Above-Ring Tangential	-5.00E-11	1.15E-11	-0.42	0.12	1.53E-12	1.55E-11	0.02	0.19
Above-Ring Vertical	-2.03E-11	2.54E-11	-0.12	0.17	6.46E-12	1.25E-11	0.04	0.07

Table 9 BSCCO Velocity^2 Coupling at 77K and 270K (Over 20 Profiles)

- be used for any purposes other than those for which it was supplied
- be copied or reproduced in whole or in detail without the prior written consent of ARCS
- be disclosed to any third party without the prior written consent of ARCS.

3.5 YBCO Coupling Factor Evaluation

The YBCO ring was purchased from ATZ and has a thicker wall thickness in order to properly seed and grow the crystals. The final size measured was 160x130x15 mm and the superconductor holder was adapted accordingly. Also in this case, trapped fields were used to evaluate the critical temperature of the YBCO ring. The tests showed that the critical temperature was about 92 K, consistent with results in the literature (see **Figure 3.5-1**).

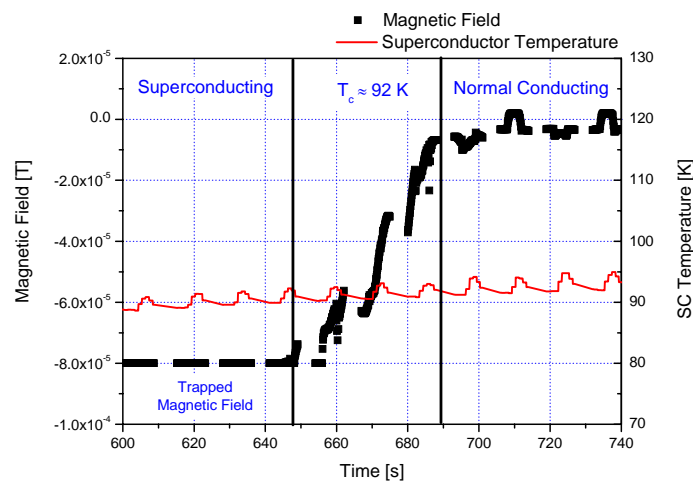


Figure 3.5-1 YBCO Critical Temperature Measurement with Trapped Magnetic Field

Figure 3.5-2 to **Figure 3.5-7** show a comparison between all sensor positions at 77K and 200K during acceleration to maximum speed in both directions. The sensor sigma at our measurement rate of 10 Hz was about 15 μg as it can be seen in the raw data plots.

The coupling factors (linear fit of raw data per profile) between gravitational field and applied acceleration, velocity and velocity² for YBCO at 77K and 200K are shown in **Tables 10-12**. The sigmas are a little bit smaller compared to the Niobium dummy tests, probably due to the smaller weight of the ring and therefore reduced forces on the bearing.

The data is very similar to the BSCCO results. For the acceleration coupling factors, again all mean values are below its sigma. Also, no significant difference can be seen between the superconductive and normal conductive case – within the resolution threshold. The sigmas must be interpreted as upper boundaries for possible gravitational interactions for YBCO.

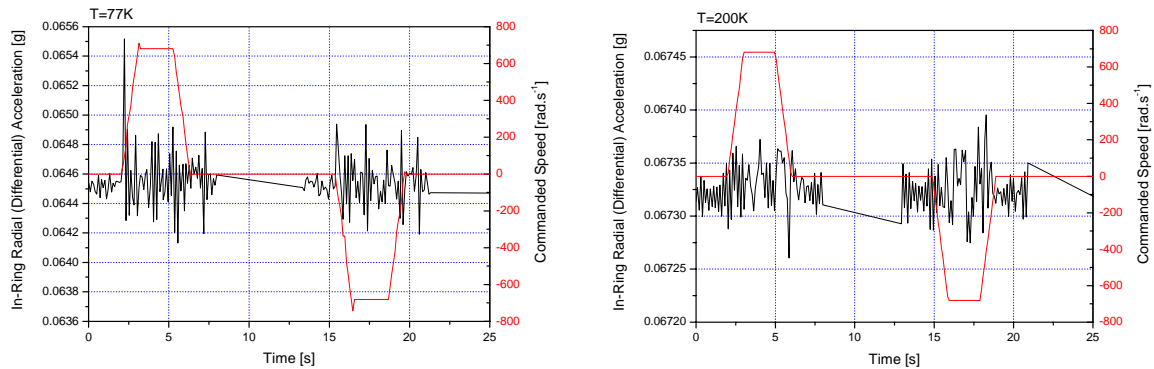


Figure 3.5-2 YBCO In-Ring Radial Differential Sensor Comparison at 77K and 200K

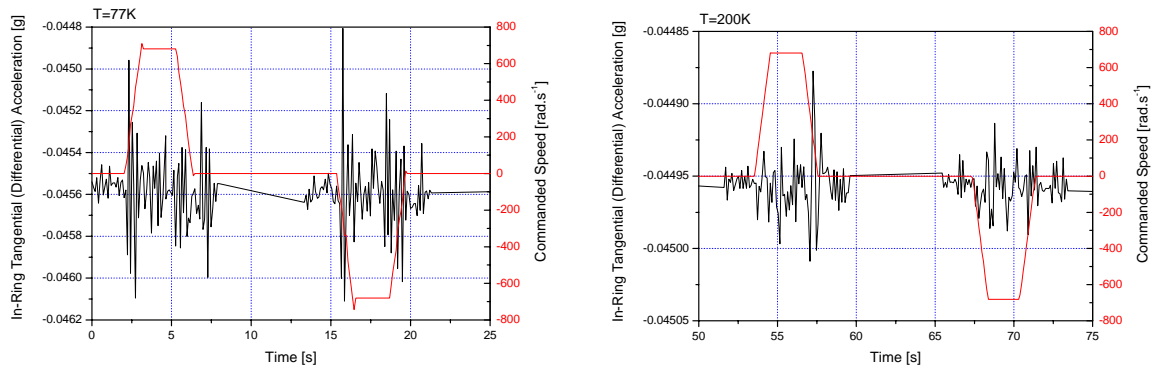


Figure 3.5-3 YBCO In-Ring Tangential Differential Sensor Comparison at 77K and 200K

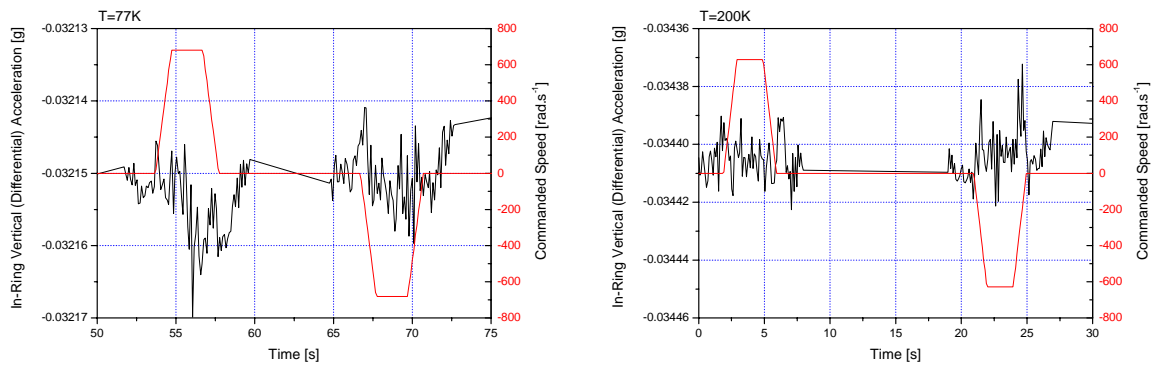


Figure 3.5-4 YBCO In-Ring Vertical Differential Sensor Comparison at 77K and 200K

- be used for any purposes other than those for which it was supplied
- be copied or reproduced in whole or in detail without the prior written consent of ARCS
- be disclosed to any third party without the prior written consent of ARCS.

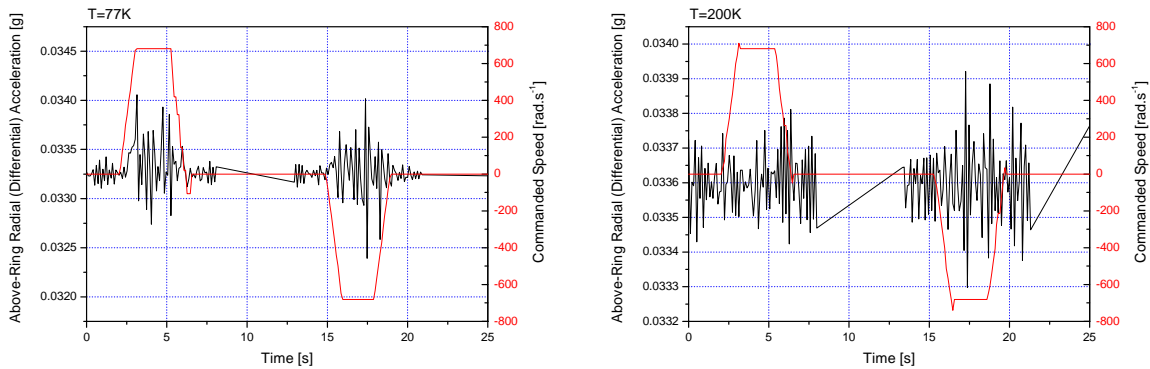


Figure 3.5-5 YBCO Above-Ring Radial Differential Sensor Comparison at 77K and 200K

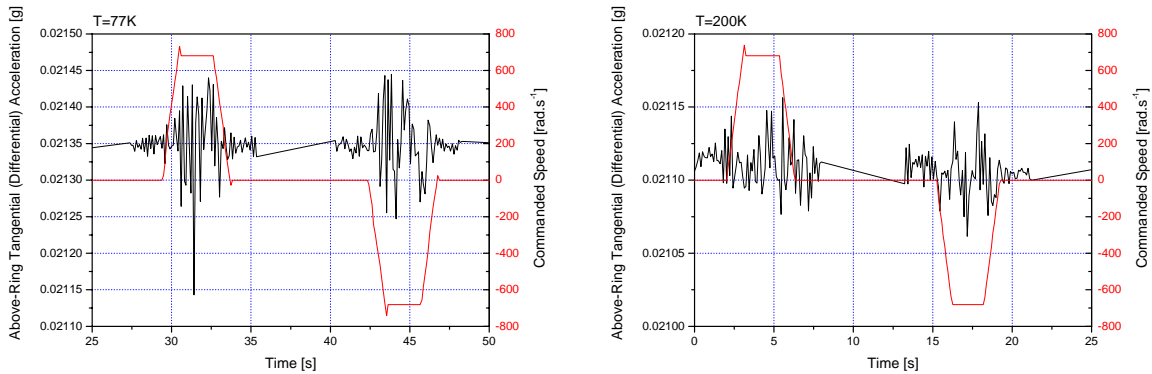


Figure 3.5-6 YBCO Above-Ring Tangential Differential Sensor Comparison at 77K and 200K

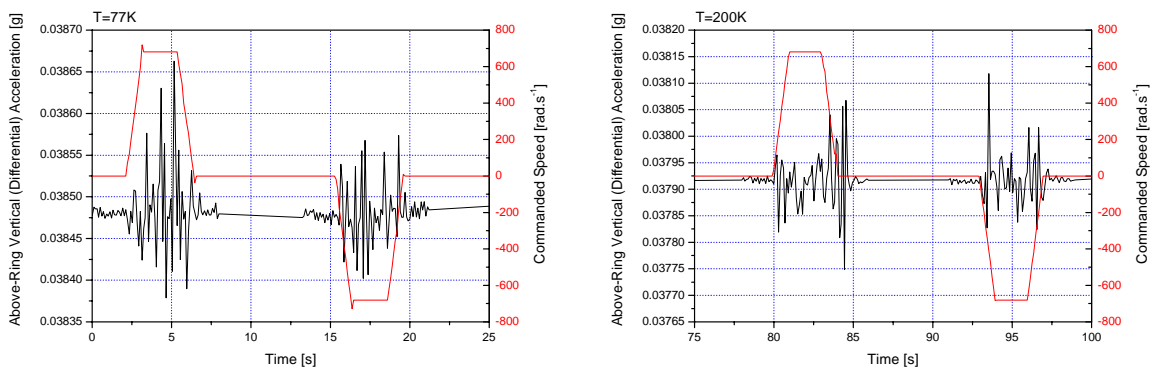


Figure 3.5-7 YBCO Above-Ring Vertical Differential Sensor Comparison at 77K and 200K

- be used for any purposes other than those for which it was supplied
- be copied or reproduced in whole or in detail without the prior written consent of ARCS
- be disclosed to any third party without the prior written consent of ARCS.

	77K				200K			
	Acceleration Coupling Factor		Correlation Factor		Acceleration Coupling Factor		Correlation Factor	
Position	Mean	Sigma	Mean	Sigma	Mean	Sigma	Mean	Sigma
In-Ring Radial	-7.96E-09	4.16E-08	-0.02	0.20	6.63E-09	8.37E-09	0.07	0.09
In-Ring Tangential	5.66E-09	1.31E-08	0.04	0.07	-5.66E-09	7.53E-09	-0.08	0.11
In-Ring Vertical	-6.17E-10	2.54E-09	-0.07	0.22	2.11E-09	3.42E-09	0.08	0.13
Above-Ring Radial	-8.58E-09	3.21E-08	-0.01	0.04	2.06E-08	1.25E-08	0.05	0.03
Above-Ring Tangential	-2.27E-09	1.12E-08	-0.02	0.09	3.24E-09	3.87E-09	0.06	0.07
Above-Ring Vertical	-4.82E-09	1.44E-08	-0.04	0.11	-1.58E-09	3.58E-08	-0.01	0.22

Table 10 YBCO Acceleration Coupling at 77K and 200K (Over 20 Profiles)

	77K				200K			
	Velocity Coupling Factor		Correlation Factor		Velocity Coupling Factor		Correlation Factor	
Position	Mean	Sigma	Mean	Sigma	Mean	Sigma	Mean	Sigma
In-Ring Radial	-1.74E-08	6.01E-08	-0.08	0.30	-4.14E-09	2.63E-08	-0.05	0.24
In-Ring Tangential	-2.45E-09	5.45E-08	-0.01	0.25	-8.80E-10	2.14E-08	0.00	0.26
In-Ring Vertical	-4.92E-10	1.33E-08	-0.01	0.44	-2.16E-11	9.64E-09	-0.03	0.30
Above-Ring Radial	8.66E-09	6.92E-08	0.01	0.08	-1.74E-09	3.23E-08	0.00	0.08
Above-Ring Tangential	2.87E-09	1.94E-08	0.03	0.15	1.29E-09	1.33E-08	0.00	0.23
Above-Ring Vertical	-1.44E-09	2.48E-08	-0.01	0.15	2.22E-09	3.47E-08	0.02	0.17

Table 11 YBCO Velocity Coupling at 77K and 200K (Over 20 Profiles)

- be used for any purposes other than those for which it was supplied
- be copied or reproduced in whole or in detail without the prior written consent of ARCS
- be disclosed to any third party without the prior written consent of ARCS.

	77K				200K			
	Velocity^2 Coupling Factor		Correlation Factor		Velocity^2 Coupling Factor		Correlation Factor	
Position	Mean	Sigma	Mean	Sigma	Mean	Sigma	Mean	Sigma
In-Ring Radial	5.60E-11	7.86E-11	0.17	0.23	3.21E-11	1.46E-11	0.20	0.09
In-Ring Tangential	-5.56E-11	5.64E-11	-0.17	0.15	-2.55E-11	1.51E-11	-0.21	0.12
In-Ring Vertical	-1.71E-11	1.33E-11	-0.36	0.25	-1.36E-11	5.54E-12	-0.28	0.11
Above-Ring Radial	8.84E-11	4.26E-11	0.07	0.03	3.86E-11	1.41E-11	0.06	0.02
Above-Ring Tangential	-3.40E-12	3.22E-11	-0.01	0.16	1.65E-11	7.10E-12	0.19	0.08
Above-Ring Vertical	-2.28E-11	3.20E-11	-0.09	0.12	-4.11E-11	2.95E-11	-0.14	0.09

Table 12 YBCO Velocity^2 Coupling at 77K and 200K (Over 20 Profiles)

- be used for any purposes other than those for which it was supplied
- be copied or reproduced in whole or in detail without the prior written consent of ARCS
- be disclosed to any third party without the prior written consent of ARCS.

4 DISCUSSION

The facility reached the design specification of Phase I and can reliably detect gravitational anomalies in rotating superconductors that are low enough to test our theory that non-classical gravitational fields are responsible for the Tate Cooper-pair mass anomaly – the design goal of Phase I. Coupling factors for all sensor directions (radial, tangential and vertical - inside and above the superconductor) were evaluated for applied angular acceleration, angular speed and angular speed² (applied centrifugal acceleration).

It could be shown that the liquid nitrogen level and external magnetic fields (e.g. from the electric motor) have no influence on the measurement and that the sensors are sufficient mechanically de-coupled to reach very low signal levels even during maximum accelerations. Both speed and accelerations obtained exceed the specifications of Phase I.

Both BSCCO and YBCO measurements showed coupling factor values similar to the dummy test with Niobium at liquid nitrogen temperatures (77 K). In addition, no significant difference between measurements at 77 K and room temperatures were seen. Nearly all mean values (except some very low numbers at ω^2 coupling factor measurements) are below the sigma values. Therefore, the sigma values can be interpreted as upper limits for a possible coupling factor between applied acceleration/speed to a superconductor and induced gravitational fields.

Table 13 compares the upper limits for the angular acceleration coupling factor (our primary theoretical prediction) in the tangential direction with the values originally derived from Tate's experiment and our latest theoretical values.

Material	Condition	Predicted Angular Acceleration Coupling Factor [s ² .rad ⁻¹]	Measured Upper Limit Angular Acceleration Coupling Factor [s ² .rad ⁻¹]
Niobium @ 6 K	From Tate's Experiment	-3.7x10 ⁻⁷	NA
Niobium @ 6 K	From Theory	-2.7x10 ⁻⁸	NA
YBCO @ 77 K	From Theory	-1.4x10 ⁻⁹	± 1.3x10 ⁻⁸
BSCCO (2212) @ 77 K	From Theory	-5.7x10 ⁻¹⁰	± 4.8x10 ⁻⁹

Table 13 Comparison of Measured Upper Limits on Angular Acceleration Couplings with Theoretical Precisions Inside Superconductor Ring in Tangential Direction

This shows that the resolution of the facility is one order of magnitude above the theoretical predictions for YBCO and BSCCO, but it is accurate enough to test induced gravitational fields for Tate's condition of using Niobium. The tests also rule out gravitational fields as large as predicted from Tate's measurements to exist for YBCO and BSCCO high-temperature superconductors.

- be used for any purposes other than those for which it was supplied
- be copied or reproduced in whole or in detail without the prior written consent of ARCS
- be disclosed to any third party without the prior written consent of ARCS.

The resolution of the AppliedMEMS sensors ($\cong 1 \mu\text{g}$) have not been reached yet, an improvement of about one order of magnitude should be still possible. It was found out that the largest noise contribution is due to the acoustic noise developed by the bottom bearing. Alternative bearing solutions such a frictionless magnetic bearing or a distribution of the bearing loads to several bearings could improve the noise level.

From the latest theoretical work it seems also more worthwhile to continue the experiments with low-temperature superconductors and liquid helium, as the facility resolution to detect gravitational anomalies e.g. for Niobium is already reached, and much larger gravitational fields can be expected.

- be used for any purposes other than those for which it was supplied
- be copied or reproduced in whole or in detail without the prior written consent of ARCS
- be disclosed to any third party without the prior written consent of ARCS.

5 CONCLUSIONS

The following conclusions have been obtained during Phase II of this project:

- A facility was designed and built to investigate μg level gravitational fields around rotating superconductors exceeding the specifications of Phase I. Angular acceleration coupling factor resolutions around $1 \times 10^{-8} \text{ s}^{-2} \cdot \text{rad}^{-1}$ were obtained.
- The coupling factors are small enough to test the originally predicted gravitational fields based on Tate's Cooper-pair measurement (about $10^{-7} \text{ s}^{-2} \cdot \text{rad}^{-1}$).
- No gravitational anomalies have been detected using BSCCO and YBCO high-temperature superconductors, as expected from latest theoretical work (at least one order of magnitude below the facilities resolution, around $1 \times 10^{-9} \text{ s}^{-2} \cdot \text{rad}^{-1}$).
- The resolution can be further increased by reducing the acoustic noise coming from the bottom bearing (exposed to cryogenic temperatures) by using either frictionless magnetic bearings or optimizing the current bearing solution (e.g. by dividing the bearing load to several bearings).
- The most promising venue seems to explore low-temperature superconductors such as Niobium at liquid helium temperatures to definitely test under the same condition as Tate did for her Cooper-pair measurement. Due to the much higher Cooper-pair density, larger gravitational fields should be produced as theoretically predicted.

- be used for any purposes other than those for which it was supplied
- be copied or reproduced in whole or in detail without the prior written consent of ARCS
- be disclosed to any third party without the prior written consent of ARCS.

REFERENCES

de Matos, C.J., and Tajmar, M., "Gravitomagnetic London Moment and the Graviton Mass Inside a Superconductor", *Physica C*, in Print (2005)

Capelle, K., and Gross, E.K.U., "Relativistic framework for microscopic theories of superconductivity. I. The Dirac equation for superconductors", *Physical Review B*, Vol. 59, 1999, pp. 7140-7154

Modanese, G., "Local Contribution of a Quantum Condensate to the Vacuum Energy Density", *Mod. Phys. Lett. A*, **18**(10), 2003, pp. 683-690

Novello, M., and Neves, R.P., "The Mass of the Graviton and the Cosmological Constant", *Classical and Quantum Gravity*, **20**, 2003, L67-L73

Ryder, L.H., "Quantum Field Theory", Cambridge University Press, 2nd Edition, 1996, pp. 296-298

Tajmar, M., and de Matos, C.J., "Gravitomagnetic Field of a Rotating Superconductor and of a Rotating Superfluid", *Physica C*, Vol. 385, No. 4, 2003, pp. 551-554

Tajmar, M., and de Matos, C.J., "Extended Analysis of Gravitomagnetic Fields in Rotating Superconductors and Superfluids", *Physica C*, Vol. 420, No. 1-2, 2005, pp. 56-60

Tate, J., Cabrera, B., Felch, S.B., Anderson, J.T., "Precise Determination of the Cooper-Pair Mass", *Physical Review Letters*, **62**(8), 1989, pp 845-848

Tate, J., Cabrera, B., Felch, S.B., Anderson, J.T., "Determination of the Cooper-Pair Mass in Niobium", *Physical Review B*, **42**(13), 1990, pp 7885-7893

- be used for any purposes other than those for which it was supplied
- be copied or reproduced in whole or in detail without the prior written consent of ARCS
- be disclosed to any third party without the prior written consent of ARCS.